主論文

Galaxy Evolution through Far-Infrared Radiation

BY

HIROYUKI HIRASHITA

Department of Astronomy, Kyoto University, Sakyo-ku, Kyoto 606-8502, Japan

Research Fellow of the Japan Society for the Promotion of Science

E-mail: hirasita@kusastro.kyoto-u.ac.jp

Ph.D. Dissertation
Submitted to Department of Astronomy, Kyoto University

Contents

Acknowledgments

I wish to express my gratitude to my advisor, Shin Mineshige for helpful discussions on many interesting topics, which motivated my research of galactic astronomy. I appreciate his reading through this thesis carefully and giving me many useful comments. I am grateful to Hideyuki Kamaya for frequent discussions and useful comments, which substantially improved the quality of my researches. I also thank Tsutomu T. Takeuchi for helpful advice especially from observational and statistical viewpoints. I acknowledge Kohji Yoshikawa for very excellent computational environment and Akio K. Inoue for helpful comments on infrared radiation from galaxies.

I am indebted to Hiroshi Shibai for my knowledge in infrared astrophysics. Much of the optical properties of galaxies is learned from Kouji Ohta and Akihiko Tomita. For the theoretical side, Andrea Ferrara often gave me useful comments: Lo ringrazio di tutto cuore. Non vedo l'ora di studiare con lui. Ryoichi Nishi is also acknowledged for his stimulating discussions.

Much of my work is supported by the members of Kwasan Observatory. I am grateful to Takako T. Ishii for the advice about how to use IDL, with which I made almost all the figures in this thesis. Hiroki Kurokawa is also acknowledged for allowing me to use the excellent facilities in the observatory.

The financial support has been provided by the Research Fellowship of the Japan Society for the Promotion of Science for Young Scientists. We fully utilized the NASA's Astrophysics Data System Abstract Service (ADS).

Finally, I thank all the members at Department of Astronomy for providing me with wonderful and stimulating environment for study.

Hiroyuki Hirashita
11 January 2001

Abstract

About half of the radiative energy from galaxies is emitted in the far-infrared (FIR) wavelength. The FIR radiation originates from the reprocessing of stellar light by dust grains. In order to reveal the time evolution of dust content in galaxies, we construct an evolution model of dust-to-gas mass ratio by extending the chemical evolution model and by considering the formation and destruction processes of dust. Based on this model, we succeed in explaining the relation between dust-to-gas ratio and metallicity for galaxies with a wide metallicity range, which confirms that our model describes the evolution of dust content of galaxies in various evolutionary stages.

The evolution of interstellar medium (ISM) may be important in the time evolution of dust-to-gas ratio. This is because the dust growth occurs only in the cold and dense phase of the ISM. We discuss the time variation of dust-to-gas mass ratio using the three-phase model of the ISM. The typical timescale of the phase change of an interstellar gas is $\sim 10^{7-8}$ yr in spiral galaxies. Since the phase transition changes the filling factor of the cold gas where the dust growth occurs, the dust growth rate varies on that timescale. We examine the response of the dust-to-gas ratio to the phase transition by adopting the Ikeuchi–Tomita model for the mass exchange among the phases. According to the model, a limit-cycle evolution of the mass exchange is obtained. In this limit-cycle case, the amplitude of the variation of the dust-to-gas ratio is large (nearly an order of magnitude) if the dust growth timescale is shorter than the phase transition timescale. Since this condition is easily satisfied in spiral galaxies, the dynamical multi-phase evolution of ISM is important for the time evolution of dust amount.

The dust amount is important for the intensity of its thermal radiation at FIR. Although FIR emission from dust is frequently used as an indicator of star formation rate (SFR), the effect of the dust-to-gas ratio (i.e., amount of the dust) on the conversion law from IR luminosity to SFR has not so far been considered. Then, we present a convenient analytical formula including this effect. Especially, we present the metallicity dependence of our conversion law between SFR and FIR luminosity with the aid of our model. We find that the effect of the chemical evolution on the conversion formula is significant: The conversion factor from FIR luminosity to SFR changes by a factor of 4 in the course of chemical enrichment. This is important in determining the cosmic SFR from the future FIR observations (e.g., ASTRO-F).

Finally, we consider the observational strategy with ASTRO-F, which will be launched in 2004. This satellite enables us to test our galaxy evolution model in the FIR wavelength. One of the main purposes of the ASTRO-F mission is an all-sky survey in the FIR with a flux limit more than ten times deeper than that of *IRAS*. We investigated the expected optical and near-infrared (NIR) number counts of galaxies detected by the FIR scanner (FIS) of ASTRO-F and the possibility of their optical and NIR follow-up. The spectral energy

distribution and the luminosity function of galaxies are modeled based on the properties of galaxies observed by *IRAS*. The galaxies are divided into two populations according to their infrared luminosities ($L_{\rm IR}$): normal spirals ($L_{\rm IR} < 10^{10} L_{\odot}$) and starbursts ($L_{\rm IR} > 10^{10} L_{\odot}$). The expected number counts of galaxies expected to be detected by ASTRO-F for both of the populations are calculated in B and H bands. As for the starburst population, we also calculated the number of galaxies with a simple model of evolution. In the evolution model, the numbers of low-z ($z < 1$), intermediate-z ($1 < z < 3$), and high-z ($z > 3$) galaxies are 100, 20, and 0.2 per square degree, respectively. The future observational facilities, e.g., F-MOS equipped with Subaru telescope can be a useful tool for the follow-up of galaxies up to $z = 3$.

keyword: galaxies: evolution — Infrared: continuum — Interstellar: dust, extinction — stars: formation

Part I

Introduction to Radiation from Dust

Chapter 1

Introduction

About 200 years ago, Sir William Herschel discovered infrared (IR) radiation in examining the warming powers of the Sun's rays dispersed by a prism. However, it is after the recent improvement of observational capabilities that the IR observation of galaxies was advanced. Here, we are interested in the electromagnetic radiation of galaxies in the wavelength range from about 5 μm to 1 mm. The IR radiation originates from *interstellar dust* heated mainly by stellar radiation field. The space observation and the parallel development of ground-based facilities for IR and sub-millimeter (sub-mm) astronomy represent major landmarks in our ability to study the emission from dust. Such a study is important in tracing the stellar radiation field. Some observational study indeed indicated that the IR luminosity of a galaxy is a good indicator of its star formation activity.

The *Infrared Astronomical Satellite* (*IRAS*), launched in 1983, permitted the first far-IR (FIR) survey unlimited to the Earth's atmosphere. It discovered hundreds of galaxies emitting well over 95% of their total luminosity in the IR. This indicates that the IR observation is important in galactic astronomy. The *Infrared Telescope in Space* (*IRTS*) (Murakami et al. 1996) was the first Japanese satellite-borne IR telescope. The objective of this mission was to measure absolute intensities of diffuse IR emissions in wavelengths from 1.4 μm to 700 μm. The *Infrared Space Observatory* (*ISO*) is a recent observatory-type satellite launched by the European Space Agency (ESA). It was launched in November 1995 and ceased operation in April 1998 following exhaustion of its liquid helium supply.

Further progress in IR galactic astronomy is expected in the beginning of the twenty-first century. ASTRO-F, a Japanese satellite which will be launched in 2004, will perform an all-sky survey with a detection limit 10–100 times deeper than that of *IRAS*. The expected number count by ASTRO-F is estimated in chapter 6. Other missions, such as *SIRTF* by NASA, *FIRST* by ESA, and so on, will also contribute to revealing the IR universe.

In this chapter, we describe the introductory overview of the IR radiation from galaxies.

1.1 Overview of Dust Emission

The light radiated from stars in absorbed and scattered by interstellar dust grains. This loss of light is observed as an interstellar extinction. The absorbed energy is returned to the radiation field in the IR regime. The peak of the intensity of the IR radiation lies around $\lambda_{\rm peak} \sim 100$ μm. With the aid of the Wien displacement law,

$$T\lambda_{\rm peak} = 2898 \text{ K } \mu\text{m}\,, \tag{1.1}$$

where T is the temperature, we find that the dust is typically 30 K in the galactic environment. The temperature is estimated later in §2.3.1 assuming the radiative equilibrium with the stellar radiation field.

A typical spiral galaxy emits 30% of its energy in FIR region (Saunders et al. 1990). The "ultra-luminous IR galaxies," whose IR luminosity is larger than $\sim 10^{12}\ M_\odot$, emits most of its energy in FIR (Sanders & Mirabel 1996). Such large fractions of FIR light result from the absorption and reprocess by dust within these galaxies. Active star formation what is generally called "starburst" contributes to such a large energy release. Extensive IR observations of galaxies are therefore necessary in order to obtain a full picture for their energy output. The observed spectral energy distribution (SED) averaged for the sample of spiral galaxies and starburst galaxies in Schmitt et al. (1997) is shown in Figure 1.1. Their SEDs are normalized to the λ7000 Å flux.

In this section, we review the IR emission from dust in galaxies. We review the mid-IR (MIR; 5 μm $\lesssim \lambda \lesssim$ 40 μm), FIR (40 μm $\lesssim \lambda \lesssim$ 200 μm), and sub-mm (200 μm $\lesssim \lambda <$ 1 mm) wavelengths. In the near-infrared wavelength (1 μm $\lesssim \lambda$5 μm), the stellar light dominates over the dust emission. The sublimation temperature of dust ($\sim$ 1000 K) corresponds to $\lambda \sim 3$ μm.

1.1.1 Far-Infrared and Sub-Millimeter

The first all-sky survey at FIR wavelengths carried out in 1983 by the *IRAS* resulted in the detection of tens of thousands of galaxies. It is now clear that part of the reason for the large number of detections is the fact that the majority of the most luminous galaxies in the universe emit the bulk of their energy in the FIR (Sanders & Mirabel 1996).

For the convenience of modeling and understanding, two different environments are often considered for the FIR–sub-mm emission from galaxies:

1. dust associated with star-forming regions,

2. dust heated by the general interstellar radiation field that is not associated with star-forming regions (generally called the cirrus component).

The radiation from the former is modeled in chapter 5 and Inoue, Hirashita, & Kamaya (2000). These environments have different importance in different types of galaxies at various evolutionary stages. For galaxies forming stars actively, such as M82, NGC 6090, and Arp 220, the former is dominated over the latter. On the contrary, quiescent spiral galaxies have the cirrus emission comparable to, or larger than, the star-forming component.

It is widely accepted that the FIR luminosity of galaxies is a useful indicator of star formation rate (SFR). The SFR of a galaxy is defined as the mass turned into stars per unit time. In fact, actively star-forming galaxies emit almost all of their radiative energy in FIR (Soifer, Houck, & Neugebauer 1987). For such galaxies, we can assume that their observed FIR luminosity is nearly equal to their bolometric luminosity. Even for spiral galaxies, the amount of stellar light absorbed by dust and re-emitted in the FIR range is about the same as the emerging stellar light (Xu & Buat 1995; Wang & Heckman 1996).

Sub-mm observations of galaxies are also important to trace an component of dust whose temperature is less than about 20 K. An array of bolometers, the Submillimeter Common User Bolometer Array (SCUBA) has been installed on the James Clerk Maxwell Telescope. The advantage of this instrument is that arrays make it possible to map the sky much more

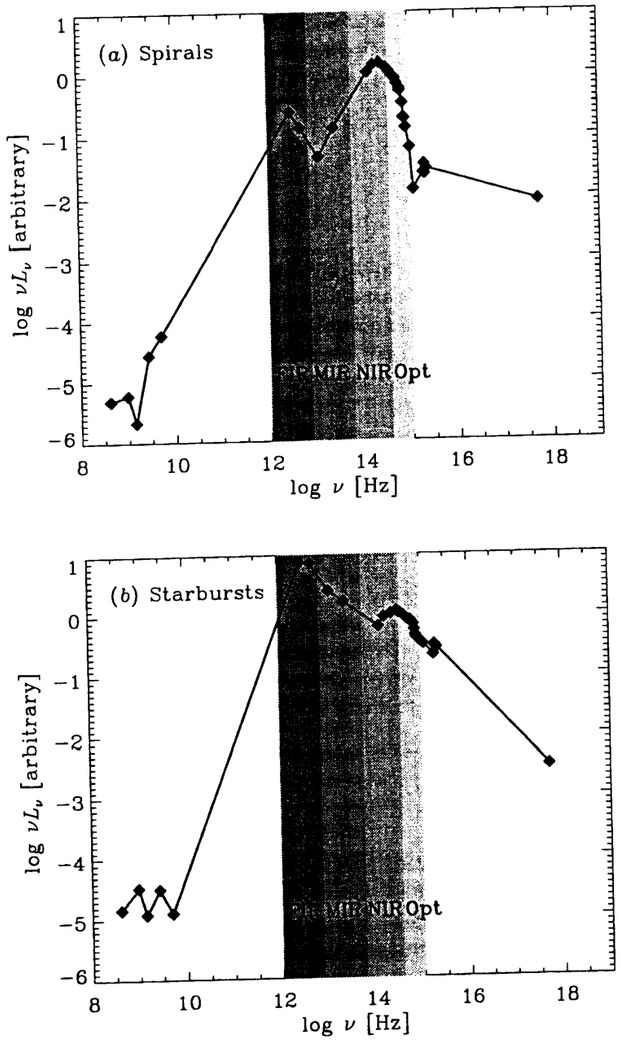

Figure 1.1: Average spectral energy distributions (SEDs; ν is the frequency and L_ν is the monochromatic luminosity) of (*a*) spiral galaxies and of (*b*) starburst galaxies of Schmitt et al. (1997). The SEDs are normalized to the λ7000 Å flux. We adopt the SBH sample in Schmitt et al. for the starburst SED. The regions denoted as "sub-mm", "FIR", "MIR", "NIR", "Opt" indicate the typical wavelength range of sub-millimeter, far-infrared, mid-infrared, near-infrared, and optical, respectively.

quickly (before the install of SCUBA, continuum observation in sub-mm had relied on single bolometers, which means that only a single point in the sky is observed at one time), and that the individual bolometers in SCUBA are ten times more sensitive than previous bolometers. Sub-mm observations are also important when we observe the high-redshift (distant) objects. This is because the rest-frame FIR wavelength for the objects is redshifted to the sub-mm (§1.2.2).

1.1.2 Mid-Infrared

Unlike FIR continuum, MIR continuum originates from the dust out of thermal equilibrium (i.e., transiently heated). Most of the recent dust models (e.g., Désert, Boulanger, & Puget 1990) accept stochastically heated very small grains with radii less than 100 Å. Such small grains are transiently heated and are not become thermal equilibrium because of their small heat capacity. The *ISO* satellite made it possible to resolve spiral galaxies with a resolution of about 10″. The MIR radiation is known to be associated with molecular gas and Hα emission (Malhotra et al. 1996; Sauvage et al. 1996). This may be because the grains emitting MIR radiation convert heating photons from star-forming regions.

The MIR spectra show several broad bands at 3.3, 6.2, 7.7, 8.6, and 11.3 μm, whose origin is interpreted as the C–C and C–H stretching and bending vibrations in polycyclic aromatic hydrocarbons (PAHs; Léger & Puget 1984; Allamandola et al. 1989). Other possible carriers are hydrogenated amorphous carbons (Borghesi, Bussoletti, & Colangeli 1987), quenched carbonaceous compounds (Sakata et al. 1987), and coal grains (Papoular et al. 1989). Observations of known starbursts in the MIR revealed that the MIR bands are rarely suppressed (Mouri et al. 1998). Thus, the bands are "common" nature for MIR SEDs of galaxies. The bands are also observed from the Galactic interstellar medium (ISM; e.g., Onaka et al. 1996).

1.1.3 Active Galactic Nuclei

The main mechanisms responsible for FIR emission from active galactic nuclei (AGNs) are nonthermal emission from a nucleus and thermal emission from dust. The relative importance of these processes appears to vary from AGN to AGN. Moreover, the ultraviolet (UV) radiation from nuclear starburst could be a heating source of the dust. On the other hand, it is argued that the nonthermal radiation is not sufficient to explain the FIR via dust reradiation (Carleton et al. 1987).

The *IRAS* survey detected many quasars (Neugebauer et al. 1986). The IR bump is characteristic of the SED of quasars (Sanders et al. 1989). This bump is ubiquitous in both radio-quiet and radio-loud quasars, but the origin may be different between the two. The radiation may originate from nonthermal process in the central engine or may result from thermal radiation from dust. The SEDs of high-redshift quasars are recently compiled by Oyabu et al. (2001).

In this thesis, we do not treat AGN to concentrate on the star formation history of galaxies. The number of AGNs in the local universe is known to be much smaller than that of star-forming galaxies. However, the number of AGNs at a high-redshift universe is poorly constrained and may be an important issue to interpret the infrared light from the universe.

1.2 Dust and Galaxy Evolution

1.2.1 Various Types of Galaxies

Luminous Infrared Galaxies

Luminous infrared galaxies (LIRGs) are often defined as the galaxies whose infrared luminosity defined in the wavelength range of 8–1000 μm is greater than $10^{11}\ L_\odot$. Galaxies more luminous in the IR range than $10^{12}\ L_\odot$ are referred to as ultraluminous infrared galaxies (ULIRGs). LIRGs contain large quantities of molecular gas, as traced by CO (Sanders et al. 1988). This as well as the observed abundant dense molecular gas traced by HCN emission, usually found only in star-forming cores (Solomon, Downes, & Radford 1992), may indicate active on-going star formation from the gas. Dust reprocessing of the radiation from such an activity is widely considered to be the energy source of the LIRGs. The term "starburst galaxies" is used for galaxies with intense star formation activities.

The optical follow-up study of LIRGs showed that a large fraction of them has interacting features (Sanders & Mirabel 1996 and references therein). The fraction increases as the IR luminosity increases. This is interpreted as an interaction induces the star formation activities. We note that the AGN fraction also increases with IR luminosity (Veilleux et al. 1995).

Spiral Galaxies

A typical spiral galaxy emits 30% of its radiative energy in the FIR. However, as shown in Tomita, Tomita, & Saitō (1996), the FIR luminosity presents a large variety among spiral galaxies. This variety can be interpreted as a scatter of star formation activities, though we should keep in mind the significant cirrus fraction in the FIR emission from spiral galaxies (§1.1.1). A possible model for this variety is presented in chapter 4 (see also Kamaya & Takeuchi 1997).

Inoue, Hirashita, & Kamaya (2000b) treated some early-type spiral (Sa–Sab) galaxies with evident star-forming regions that concentrate in their own central 1 kpc by adopting the sample of Usui, Saitō, & Tomita (1998). There are some early-type spiral galaxies showing evident star-forming activity (e.g., Keel 1983; Hameed & Devereux 1999). According to Inoue et al. (2000a), the SFR of this central region is about 2 $M_\odot\ \mathrm{yr}^{-1}$. Inoue et al. (2000b) moreover estimated the star formation efficiency (SFE) in this central 1 kpc star-forming region, taking into account the condition required for this region to be self-gravitating. Here we define the SFE as being the ratio of the stellar mass in a star-forming region to the gas mass of a parent cloud. This SFE relates more directly than the SFR to the mechanism of turning the interstellar medium (ISM) into stars. Using two indicators of the present SFR, Hα and infrared luminosities, they estimated the SFE to a few percent. This is equivalent to the observational SFE in late-type disks. This coincidence may support the universality of the mean SFE of spiral galaxies as suggested by Young et al. (1996) and Rownd & Young (1999).

Recent *ISO* observation have resolved spiral galaxies in the MIR region (e.g., Sauvage et al. 1996). Well-defined spiral arms are seen in the wavelength. A tight correlation in brightness between MIR and Hα is seen in M51. This indicates that a strong MIR radiation originates from the region with an intense star formation activity. The *IRAS* FIR pictures of the disks of normal galaxies also correlate very well with their images in Hα (e.g., Devereux

1996).

Dwarf Galaxies

In the last two decades, increasing attention has been paid to the study of dwarf galaxies in order to understand their crucial role in galaxy formation and evolution. In hierarchical clustering theories (e.g., White & Frenk 1991) these systems can constitute the building blocks from which larger systems have been created by merging. A population of newly star-forming dwarfs at $z \lesssim 1$ has been also invoked in some evolutionary models to reproduce the excess of faint blue galaxies observed in deep photometric surveys.

The detection of the FIR flux from dwarf galaxies is limited in the nearby sample, since the dust content is much smaller than spiral galaxies. However, large FIR sample of dwarf galaxies will be available at the beginning of the 21st century owing to some FIR observations as summarized in Takeuchi et al. (1999). Kamaya & Hirashita (2001) estimated the flux from I Zw 18 (a dwarf irregular galaxy at the distance of 10 Mpc) as ~ 10 mJy (This means that the galaxy has IR luminosity of 10^6–$10^7\ L_\odot$). This flux level is detectable with ASTRO-F.

The dust-to-gas ratio determined from the IR luminosity and H I observation for the *IRAS* sample of dwarf galaxies are explained through a chemical evolution model by Lisenfeld & Ferrara (1998). They noted that the mass loss from the dwarf galaxies is important to reproduce the scatter of the dust-to-gas ratio. Recently, however, Tajiri & Kamaya (2001) noted that the H I envelope around a star-forming region effectively works as a reservoir of momentum. This mechanism may keep gas from escaping out of a dwarf system. After their suggestion, Hirashita, Tajiri, & Kamaya (2001, in preparation) showed that significant mass loss is not necessary to explain the scatter of the dust-to-gas ratio of the dwarf sample if the rate of dust destruction changes significantly as a function of time. Since the destruction is caused by supernova (SN) shocks, a temporal variation of SN rate is necessary for the time variation of dust destruction rate. This temporal change is naturally introduced if dIrrs experience intermittent star formation histories.

Elliptical Galaxies

Elliptical galaxies are not gas-rich and show little evidence of present star formation activities. This is considered to result from the gas loss due to successive energy input from SNe. However, roughly 40% of a sample of bright elliptical galaxies were detected by *IRAS* (Knapp et al. 1989) but mostly at low value of the IR-to-optical luminosity ratio. The cold gas content inferred from the *IRAS* flux level is 10^7–$10^8\ M_\odot$ (Jura et al. 1987). This is much smaller than the mass of cold gas in spiral galaxies. It is also known that about 40% of bright ellipticals have dust lanes. The origin of dust in elliptical galaxies has not yet been made clear. For example, external origin of dust is discussed. (e.g., Binney & Merrifield 1998, §8.2.2).

1.2.2 Observational View of Galaxy Evolution

Galaxy Number Counts

Galaxy number count provides a useful tool to investigate the galaxy evolution to high redshift, since it can be made from observational quantities (i.e., *galaxy number* as a function of *observed flux*). The galaxy evolution is constrained by predicting the count from models.

Recent modeling by *semi-analytic* method (e.g., Guiderdoni et al. 1998) as well as by empirical method (e.g., Takeuchi et al. 2001b) can be compared with the number count by the *ISO* satellite now. Takeuchi et al. (2001b) modeled the number count in the mid–far-IR wavelengths and compared their prediction with the *ISO* number count and the FIR background spectrum. They determined a probable history of the comoving IR luminosity density, suggesting that the IR luminosity density increases rapidly from $z = 0$ to $z = 1$ by an order of magnitude. They also showed that the IR density should be < 10 times between $1 \lesssim z \lesssim 5$ as large as that at $z = 0$ to be consistent with the sub-mm background intensity.

ASTRO-F will be a powerful tool to reveal the galaxy evolution in the IR wavelength. Hirashita et al. (1999) calculated the optical number count of galaxies detected by ASTRO-F and considered the strategy for the optical follow-up observation (see chapter 6 for the detailed description for the model and the result).

At a high redshift, the rest-frame FIR light of galaxies is observed at longer wavelength, especially the sub-mm band. Indeed, SCUBA has recently been used to detect distant dusty galaxies (§1.1.1; Smail, Ivison, & Blain 1997). By using the magnification owing to the gravitational lens, the deeper survey is made possible (Blain 1998; Smail et al. 1998). Further progress is expected by the Atacama Submillimeter Telescope Experiment (ASTE) and the Atacama Large Millimeter Array/Large Millimeter and Submillimeter Array (ALMA/LMSA). The observational strategy is described in Takeuchi et al. (2001a).

Cosmic FIR Background

The contribution of young galaxies to the visible and IR background radiation was investigated by Partridge & Peebles (1967; see also Stecker, Puget, & Fazio 1977). Puget et al. (1996) searched for an extragalactic FIR background in the whole sky data of the Cosmic Background Explorer (*COBE*) satellite by removing the interplanetary and interstellar dust components (see also Fixsen et al. 1998; Hauser et al. 1998). The data put a strong constraint on IR luminosity of galaxies at various redshifts. A strong evolution of IR light between $z = 0$ and $z = 1$ is indicated, and the strong constraint is put on the luminosity (or number) of high-redshift galaxies from the sub-mm part of the background (Gispert, Lagache, & Puget 2000; Takeuchi et al. 2001b). In Figure 1.2, we show the cosmic background radiation in the UV–sub-mm range.

Cosmic Star Formation History

The emission history of the universe at UV, optical and near-IR wavelengths provides us a clue to the star formation history of galaxies as a whole (Madau et al. 1996). Usually the star formation history of the universe is indicated with the star formation rate (SFR) per comoving volume as a function of the redshift z. The determination of the cosmic star formation history is made possible after recent deep observations, especially the Hubble Deep Field. Estimate of SFR at high redshift became possible owing to the Lyman break technique, which is developed to select galaxies at $z \sim 3$ (Steidel et al. 1996), and the photometric redshift technique, which provided us with a way of determining the redshifts of a large sample of galaxies (e.g., Connolly et al. 1997).

According to Madau et al. (1996), the comoving SFR density has a peak around $z \sim 1.5$ (see also Madau, Pozzetti, & Dickinson 1998), and it decreases monotonically beyond $z \sim 1.5$. However, Steidel et al. (1999) suggested that the comoving SFR density is almost constant at $z \gtrsim 2$.

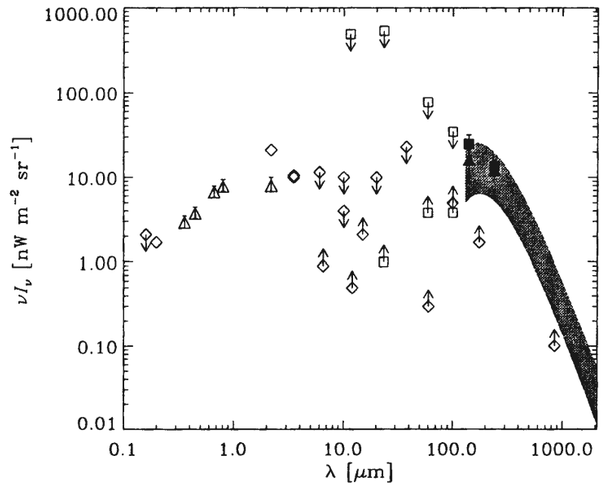

Figure 1.2: Cosmic background from the UV–sub-millimeter wavelength. I_ν is the intensity for the background light per unit solid angle. For the reference of each point, see Gispert et al. (2000). The data are compiled by T. T. Takeuchi.

The biggest uncertainty is, however, represented by the amount of starlight that was absorbed by dust and reradiated in the MIR–FIR wavelengths. The role of extinction in high redshift galaxies has yet to be comprehensively analyzed. A model of the history of the emission of galaxies in a wide wavelength range (UV–FIR) is constructed by Pei, Fall, & Hauser (1999). Tan, Silk, & Balland (1999) discussed the history of the IR universe. Both of them concluded the peak of the comoving IR density at $z \sim 1$–3. Takeuchi et al. (2001b) empirically derived the comoving IR density based on the number count by *ISO* and the cosmic IR background. They concluded that the peak exists at $z \lesssim 1$. We should wait for further observational results with future facilities to solve the history of the emissivity in the universe.

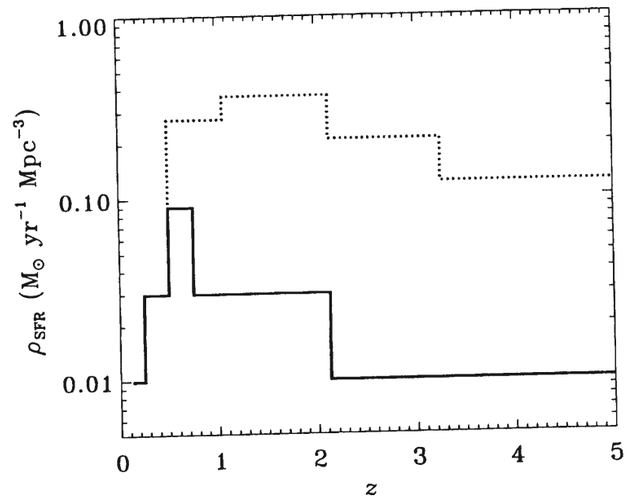

Figure 1.3: Cosmic star formation history determined by from observed IR number counts by Takeuchi et al. (2001b). The comoving density of star formation rate ($\rho_{\rm SFR}$) is presented as a function of the redshift z. The solid line represents the minimum of all the three models investigated by them, while the dotted line indicates the maximum.

Chapter 2

Basic Formulation of Radiation from Dust

2.1 Radiative Transfer

Radiation reaching us provides most of our direct knowledge about the dust, whose IR emission is the main topics of this thesis. The radiative transfer equation is a useful tool to analyze the radiation. Hence, first of all, the basic concepts of radiative transfer are reviewed.

The photons traveling by a point $\boldsymbol{r}$ at a time t is considered. Each of them will have a different direction, denoted by the unit vector $\hat{\boldsymbol{k}}$, and a different frequency ν. To characterize the radiation field we must specify the energy passing by as a function of all four of these physical variables. We define the specific intensity $I_\nu(\hat{\boldsymbol{k}}, \boldsymbol{r}, t)$ so that $I_\nu \, \mathrm{d}\nu \, \mathrm{d}\omega \, \mathrm{d}A \, \mathrm{d}t$ is the energy of those photons which during a time interval $\mathrm{d}t$ pass through the area $\mathrm{d}A$, whose frequency lies within the element $\mathrm{d}\nu$ about ν, and whose direction is within the solid angle $\mathrm{d}\omega$ about $\hat{\boldsymbol{k}}$; $\mathrm{d}A$ is located at the position $\boldsymbol{r}$ and is perpendicular to the photon direction $\hat{\boldsymbol{k}}$. The geometry considered is illustrated in Figure 2.1.

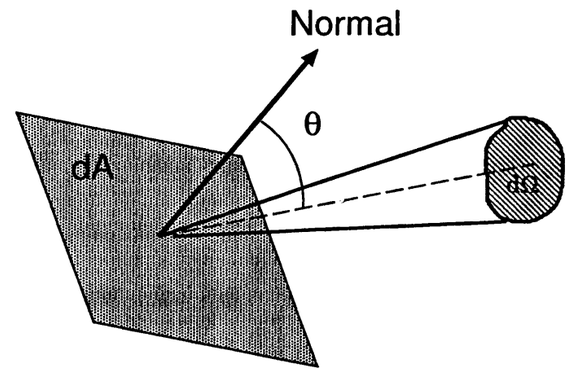

Figure 2.1: Geometry for a ray considered in the text.

The specific energy density u_ν is defined as the energy per unit volume per unit frequency

range. To determine this it is convenient to consider first the energy density per unit solid angle $u_\nu(\Omega) \equiv I_\nu/c$. Integrating over all solid angles we have

$$u_\nu \equiv \int u_\nu(\Omega)\,\mathrm{d}\Omega = \frac{1}{c}\int I_\nu\,\mathrm{d}\Omega\,, \tag{2.1}$$

or

$$u_\nu = \frac{4\pi}{c}J_\nu\,, \tag{2.2}$$

where we have defined the mean intensity J_ν:

$$J_\nu \equiv \frac{1}{4\pi}\int I_\nu\,\mathrm{d}\Omega\,. \tag{2.3}$$

The flux F_ν is defined as

$$F_\nu = \int I_\nu \cos\theta\,\mathrm{d}\Omega\,, \tag{2.4}$$

where θ is the angle between the line normal to the surface element $\mathrm{d}A$ and the ray.

The change of I_ν resulting from interaction with matter is governed by the equation of transfer. This equation is derived by considering the flow of energy in and out the ends of cylinder of length $\mathrm{d}s$, with the use of the absorption and emission coefficients κ_ν and j_ν. The absorbed intensity in the cylinder is assumed to be $\kappa_\nu I_\nu\,\mathrm{d}s$, while the emitted intensity is denoted as $j_\nu\,\mathrm{d}s$. As a result, we obtain the following equation for the change of I_ν along a distance $\mathrm{d}s$:

$$\frac{\mathrm{d}I_\nu}{\mathrm{d}s} = -\kappa_\nu I_\nu + j_\nu\,. \tag{2.5}$$

We define the optical depth τ_ν backward along the ray path by the expression

$$\mathrm{d}\tau_\nu = -\kappa_\nu\,\mathrm{d}s\,. \tag{2.6}$$

At the observer $\tau_\nu = 0$. If we consider the radiation received from a region or cloud of total optical thickness τ_ν^0, equation (2.5) may be integrated to yield

$$I_\nu = I_\nu(0)e^{-\tau_\nu^0} + \int_0^{\tau_\nu^0}\frac{j_\nu}{\kappa_\nu}e^{-\tau_\nu}\,\mathrm{d}\tau_\nu\,, \tag{2.7}$$

where $I_\nu(0)$ denotes the value of I_ν on the far side of the emitting region from the observer, where $\tau_\nu = \tau_\nu^0$.

Under the thermodynamic equilibrium, it is required that $I_\nu = B_\nu(T)$, where $B_\nu(T)$ is the Planck function at the temperature of T:

$$B_\nu(T) = \frac{2h\nu^3}{c^2}\frac{1}{e^{h\nu/k_\mathrm{B}T}-1}\,. \tag{2.8}$$

The Planck function is also expressed if we adopt the wavelength λ as the measure of intensity:

$$B_\lambda(T) = \frac{2hc^2}{\lambda^5}\frac{1}{e^{hc/\lambda k_\mathrm{B}T}-1}\,. \tag{2.9}$$

Since $\mathrm{d}I_\nu/\mathrm{d}s$ must vanish if I_ν is constant, we see from equation (2.5) that

$$j_\nu = \kappa_\nu B_\nu(T) \tag{2.10}$$

in the thermal equilibrium. This relation is known as Kirchhoff's law.

2.2 Interstellar Extinction

In the wavelengths around the optical band, the transmitted beam of electromagnetic radiation is reduced in intensity by two physical processes, absorption and scattering of grains. This reduction of energy is called interstellar extinction. In this section, we begin by outlining the theoretical basis for models of extinction.

2.2.1 Extinction by Spherical Grains

Here, spherical grains is assumed in considering the extinction properties of the dust. Suppose that spherical dust grains of radius a are distributed uniformly with number density n_d per unit volume along the line of sight to a star. We define $C_{\mathrm{ext},\nu}$ as the extinction cross section (i.e., the absorption coefficient per grain):

$$\kappa_\nu = n_\mathrm{d}C_{\mathrm{ext},\nu}\,. \tag{2.11}$$

We omit the subscript ν (or λ) hereafter in this section, but we should note the ν dependence of κ and C_ext. Considering an element of column with length $\mathrm{d}s$, the fractional reduction in intensity of starlight at a given wavelength is

$$\frac{\mathrm{d}I}{I} = -n_\mathrm{d}C_\mathrm{ext}\,\mathrm{d}s\,, \tag{2.12}$$

where emission can be neglected around the visible wavelengths. The emission around FIR is considered in §2.3. The optical depth τ is expressed as $\mathrm{d}\tau = -n_\mathrm{d}C_\mathrm{ext}\,\mathrm{d}s$ (with $\kappa = n_\mathrm{d}C_\mathrm{ext}$ and eq. [2.6] combined). From equation (2.12), we obtain

$$I = I_0\exp(-\tau)\,, \tag{2.13}$$

where I_0 is the value of I at $s = 0$. Expressing the intensity reduction in magnitudes, the total extinction at some wavelength λ is given by

$$A_\lambda \equiv -2.5\log\left(\frac{I}{I_0}\right) = 1.086N_\mathrm{d}C_\mathrm{ext}\,, \tag{2.14}$$

where the column density N_d is defined as the density integrated over the whole line of sight.

$$N_\mathrm{d} \equiv \int n_\mathrm{d}\,\mathrm{d}s\,. \tag{2.15}$$

If we define Q_ext as the ratio of extinction cross section to geometric cross section, i.e.,

$$Q_\mathrm{ext} \equiv \frac{C_\mathrm{ext}}{\pi a^2}\,, \tag{2.16}$$

we obtain

$$A_\lambda = 1.086N_\mathrm{d}\pi a^2 Q_\mathrm{ext}\,. \tag{2.17}$$

If we have a size distribution, then equation (2.17) is replaced by

$$A_\lambda = 1.086\pi\int a^2 Q_\mathrm{ext}(a)\,N(a)\,\mathrm{d}a\,, \tag{2.18}$$

where $N(a)\,\mathrm{d}a$ is the number of grains per column in the line of sight with radii in the range from a to $a + \mathrm{d}a$.

The extinction efficiency is the sum of corresponding factors for absorption and scattering,

$$Q_{\rm ext} = Q_{\rm abs} + Q_{\rm sca}\,. \tag{2.19}$$

These efficiencies are functions of two quantities, a dimensionless size parameter,

$$x \equiv \frac{2\pi a}{\lambda}\,, \tag{2.20}$$

and the complex refractive index of the grain material,

$$m = n - ik\,. \tag{2.21}$$

The problem is that of solving Maxwell's equations with appropriate boundary conditions at the grain surface. A solution was first formulated by Mie (1908) and independently by Debye (1909), resulting in what is now known as the Mie theory.

The asymptotic behavior of the extinction efficiency is as follows. At very large x ($a \gg \lambda$), $Q_{\rm ext}$ is constant. When $x \ll 1$ ($a \ll \lambda$) is satisfied (in FIR, this condition is satisfied), useful approximations may be used to give simple expressions for the efficiency factors (Bohren & Huffman 1983, Chap. 5):

$$Q_{\rm sca} \simeq \frac{8}{3}x^4\left|\frac{m^2-1}{m^2+2}\right|^2\,, \tag{2.22}$$

$$Q_{\rm abs} \simeq 4x\,{\rm Im}\left\{\frac{m^2-1}{m^2+2}\right\}\,. \tag{2.23}$$

The quantity $(m^2-1)/(m^2+2)$ is often only weakly dependent on wavelength. In this case, extinction dominated by absorption in the small particle limit gives a λ^{-1} dependence, whilst extinction dominated by scattering gives a λ^{-4} dependence (Rayleigh scattering).

2.2.2 The Mean Extinction Curve of the Galaxy

Trumpler (1930a, b) considered the colors of stars in the presence of interstellar extinction produced by submicron-sized particles, concluding the reddening effect to be expected, exactly analogous to the reddening of the sun at sunset by particles in the terrestrial atmospheres. In order to study in detail the observed properties of reddening, it is essential to use background stars with known spectral characteristics as probes. The degree of reddening or "selective extinction" of a star in the Johnson BV system is quantified as the color excess

$$E_{B-V} = (B-V) - (B-V)_0\,, \tag{2.24}$$

where $(B-V)$ and $(B-V)_0$ are observed and "intrinsic" values of the color index. The relation between total extinction at a given wavelength and a corresponding color excess depends on the wavelength dependence of extinction, or extinction curve. The extinction in the visual passband may be related to E_{B-V} by

$$A_V = R_V E_{B-V}\,, \tag{2.25}$$

where R_V is the ratio of total to selective extinction. Theoretically, R_V is expected to depend on the composition and size distribution of the grains.

Reliable data on the wavelength dependence of extinction are available in the spectral region from 0.1 to 5 μm. Studies of large samples of stars have shown that the extinction curve takes the same general form in many lines of sight. The best available data plotted in Figure 2.2 are taken from Table 3.1 of Whittet (1992), who compiled the data by Whittet (1988) and Savage & Mathis (1979). One of the most prominent feature in the extinction curve is the bump at 2175 Å.

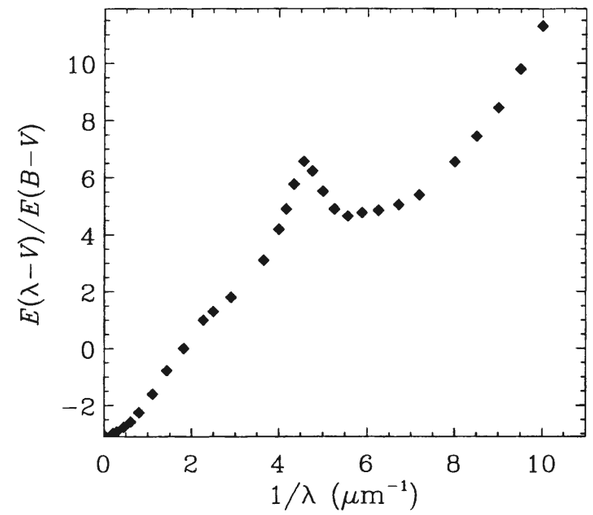

Figure 2.2: The average interstellar extinction curve ($E_{\lambda-V}/E_{B-V}$ versus λ^{-1}). The data are taken from Table 3.1 of Whittet (1992).

The values of extinction presented in Figure 2.2 make use of standard normalizations with $E(B-V)$ and the expression for the normalized extinction is modified as

$$\frac{E_{\lambda-V}}{E_{B-V}} = R_V\left\{\frac{A_\lambda}{A_V} - 1\right\}\,. \tag{2.26}$$

Since the extinction asymptotically reach zero as the wavelength becomes large, R_V is related formally to the normalized relative extinction by the limit

$$R_V = -\left[\frac{E_{\lambda-V}}{E_{B-V}}\right]_{\lambda\to\infty}\,, \tag{2.27}$$

and may thus be deduced by extrapolation of the observed extinction curve to $\lambda^{-1} \to 0$. A non-linear least-square fit from 0.7 to 5 μm yields

$$\frac{E_{\lambda-V}}{E_{B-V}} = 1.19\lambda^{-1.84} - 3.05 \tag{2.28}$$

(Martin & Whittet 1990). This relation indicates that $R_V = 3.05$.

2.2.3 Models for Interstellar Extinction

The nature of the grains responsible for the observed extinction curve must be investigated from a model calculation carried out for candidate materials with laboratory-measured optical properties and an assumed size distribution. Observations in the ultraviolet (UV) led to the development of multicomponent grain models: (i) "large" grains ($a \gtrsim 0.02$ μm) that contribute to the visible–infrared extinction; (ii) "small" grains that absorb at 2175 Å; and (iii) an additional population of small grains which account for the far-UV extinction. The two kinds of small grains responsible for (ii) and (iii) may respond differently to environmental influences.

A two-component model, based on uncoated refractory particles following a power-law size distribution

$$N(a) \propto a^{-3.5}\,, \tag{2.29}$$

was formulated by Mathis, Rumpl, & Nordsieck (1977, hereafter MRN). MRN estimated the upper and lower cutoffs to the size distribution to be $a_{\rm min} \simeq 0.005$ μm, and $a_{\rm max} \simeq 0.25$ μm. In the MRN model, graphite contributes significantly to the extinction at all wavelengths and requires $\sim$ 70% depletion of carbon into this form of dust. Especially, the extinction feature seen at $\lambda = 2175$ Å may be due to the graphite with $a \lesssim 300$ Å. Draine & Lee (1984) reinvestigated the extinction due to the MRN mixture using their results for the silicate and graphite dielectric functions. For the result of theoretical fittings for the observed extinction curve, see Figure 3.11 of Whittet (1992).

2.2.4 Dust Density and Dust-to-Gas Ratio

The integral of $Q_{\rm ext}$ over all λ can be obtained from the Kramers-Krönig relationship (Purcell 1969; Spitzer 1978). We start with a complex electric susceptibility as a function of angular frequency of the electromagnetic wave, ω:

$$\chi(\omega) = \chi'(\omega) - i\chi''(\omega), \tag{2.30}$$

where χ' and χ'' are real. From the Kramers-Krönig relation, we obtain for the static electric susceptibility

$$\chi'(0) = \frac{2}{\pi}\int_0^\infty \frac{\chi''(\omega)}{\omega}\,{\rm d}\omega. \tag{2.31}$$

We apply this relation to the ISM. If a spherical grain whose radius is a is assumed, the real and complex parts of the susceptibility is expressed as

$$\chi'(0) = Na^3\frac{\epsilon_{\rm g}-1}{\epsilon_{\rm g}+2} \tag{2.32}$$

$$\chi''(\omega) = N\frac{\lambda}{2\pi}C_{\rm ext}, \tag{2.33}$$

respectively (Purcell 1969), where $\epsilon_{\rm g}$ is the static dielectric constant of grain and N is the number of grain per unit volume. Combining equations (2.16), (2.31), (2.32), and (2.33), we

obtain

$$\int_0^\infty Q_{\rm ext}{\rm d}\lambda = 4\pi^2 a\left\{\frac{\epsilon_{\rm g}-1}{\epsilon_{\rm g}+2}\right\}. \tag{2.34}$$

If equation (2.17) is used to eliminate $Q_{\rm ext}$, and if we let $\rho_{\rm s}4\pi a^3 N_{\rm d}/3 = \rho_{\rm d}L$, where $\rho_{\rm s}$ is the density of solid material within the grain, and $\rho_{\rm d}$ is the mean density of dust along the line of sight, of length L, equation (2.34) becomes

$$\rho_{\rm d} = 1.01\times10^{-23}\rho_{\rm s}\left\{\frac{\epsilon_{\rm g}+2}{\epsilon_{\rm g}-1}\right\}\int_0^\infty \frac{A_\lambda\,{\rm d}\lambda({\rm cm})}{L({\rm kpc})}\,. \tag{2.35}$$

From a knowledge of the observed mean extinction curve, $\rho_{\rm d}$ may be expressed approximately as

$$\langle\rho_{\rm d}\rangle = 1.2\times10^{-27}\rho_{\rm s}\left\langle\frac{A_V}{L}\right\rangle\frac{\epsilon_{\rm g}+2}{\epsilon_{\rm g}-1}\,, \tag{2.36}$$

where L is again in kpc and $\langle\ \rangle$ denotes an average over stars at all the same distance. From observations of reddened stars, $\langle A_V/L\rangle \simeq 1.8$ mag kpc^{-1} in the diffuse interstellar medium (ISM) (Whittet 1992, §1.1.2), and if we assume that $m = 1.50 - 0i$ and $\rho_{\rm s} = 2.5$ g cm^{-3}, appropriate to low-density silicates, then

$$\rho_{\rm d} \simeq 1.8\times10^{-26}\ {\rm g\ cm^{-3}}\,. \tag{2.37}$$

The dust-to-gas ratio, $\mathcal{D}$, is defined as

$$\mathcal{D} \equiv \frac{\rho_{\rm d}}{\rho_{\rm gas}}\,, \tag{2.38}$$

where $\rho_{\rm gas}$ is the gas mass density. According to equation (7.19) in Spitzer (1978), $\rho_{\rm gas} = 2.8\times10^{-24}$ g cm^{-3}, where we have assumed a H–He ratio of 10 by number. Thus, we finally obtain the dust-to-gas ratio in the solar neighborhood as

$$\mathcal{D} \simeq 6\times10^{-3}. \tag{2.39}$$

2.3 Far-Infrared Emission of Dust

Infrared diffuse emission from interstellar dust was predicted by van de Hulst (1946) as a consequence of the balance of energy absorbed by the dust grains over the entire electromagnetic spectrum. In a typical interstellar environment, a dust particle gains energy mainly by absorption of UV photons from the ambient interstellar radiation field. A steady state is established: the grain emits a power equal to that absorbed, at some temperature $T_{\rm d}$; van de Hulst showed that for classical dielectric spheres of radii $a \sim 0.1$ μm, $T_{\rm d} \sim$ 10–20 K is expected, and emission should thus occur in the far infrared (FIR), a prediction confirmed some 25 years later (Pipher 1973).

Since an interstellar cloud is, in general, optically thin at FIR wavelengths, observed flux densities sample emission at all depths in the cloud with equal efficiency. Observations of the diffuse emission thus provide valuable information on the spatial distribution of dust in the ISM as well as on grain properties (Hildebrand 1983).

2.3.1 Equilibrium Dust Temperatures

Interstellar grains exchange energy with their environment as a result of absorption and emission of radiation, collisions, and surface reactions of surface reactions. The equilibrium temperature is determined primarily by radiative processes except in clouds of the highest opacity (Spitzer 1978, pp. 191–193).

Now we consider a spherical dust grain of radius $a \sim 0.1$ μm. The power absorbed from the interstellar radiation field (ISRF) is

$$W_{\rm abs} = c(\pi a^2) \int_0^\infty Q_{\rm abs}(\nu)\, u_\nu \, {\rm d}\nu \,, \tag{2.40}$$

where u_ν is the energy density of the ISRF with respect to frequency. The power radiated by the grain is

$$W_{\rm rad} = 4\pi(\pi a^2) \int_0^\infty Q_{\rm em}(\nu)\, B_\nu(T_{\rm d})\, {\rm d}\nu \,, \tag{2.41}$$

where $Q_{\rm em}$ is the efficiency factor for emission from the grain. It follows from Kirchhoff's law that

$$Q_{\rm abs}(\nu) = Q_{\rm em}(\nu) \equiv Q_\nu \,. \tag{2.42}$$

Now we consider a spherical large dust grain ($a \sim 0.1$ μm). Because $a \sim \lambda$ for the UV range, where the absorption is the most efficient, Q_ν is not strongly dependent on ν. Thus,

$$W_{\rm abs} \simeq \pi a^2 \langle Q_\nu \rangle_{\rm UV} 4\pi J \,, \tag{2.43}$$

where $\langle Q_\nu \rangle_{\rm UV}$ is the average dust absorption efficiency at UV–optical wavelength and

$$4\pi J \equiv \int_0^\infty 4\pi J_\nu {\rm d}\nu = \int_0^\infty c u_\nu {\rm d}\nu \,. \tag{2.44}$$

At FIR, $a \ll \lambda$. Thus, we use the small-particle approximation to specify Q_ν. In general, Q_ν follows a power law in the FIR as $Q_\nu \propto \nu^\beta$. Thus we obtain

$$W_{\rm rad} = 4\pi(\pi a^2) \langle Q_\nu \rangle_{\rm FIR} \int_0^\infty \left(\frac{\nu}{\nu_0}\right)^\beta B_\nu(T_{\rm d}) {\rm d}\nu \,, \tag{2.45}$$

where $\langle Q_\lambda \rangle_{\rm FIR}$ is the average absorption efficiency in FIR wavelengths at frequency ν_0. Theoretically, we expect $\beta = 2$ for metals and crystalline dielectric substances, and $\beta = 1$ for amorphous, layer-lattice materials (Tielens & Allamandola 1987).

For the equilibrium state, $W_{\rm abs} = W_{\rm rad}$, we obtain

$$4\pi J = 4\pi \frac{\langle Q_\lambda \rangle_{\rm UV}}{\langle Q_\lambda \rangle_{\rm FIR}} \int_0^\infty \left(\frac{\nu}{\nu_0}\right)^\beta B_\nu(T_{\rm d})\, {\rm d}\nu \,. \tag{2.46}$$

If we set $\langle Q_\lambda \rangle_{\rm UV} / \langle Q_\lambda \rangle_{\rm FIR} = 700$ at $\nu_0 = 3 \times 10^{12}$ Hz ($\lambda = 100$ μm) (Shibai, Okumura, & Onaka 1999) and $\beta = 2$, the integrated flux density of the ambient radiation field is obtained in units of Habing value (1.6×10^{-3} erg s^{-1} cm^{-2}; Habing 1968) as

$$G \equiv \frac{4\pi J}{1.6 \times 10^{-3} \text{ erg s}^{-1} \text{ cm}^{-2}} = 1.84 \times 10^{-7} T_{\rm d}^6 \,. \tag{2.47}$$

Since radiation field in typical Galactic plane indicates $G \sim 1$, we find $T_{\rm d} \sim 18$ K. Higher temperature is observationally indicated for dust in or near H II regions (Glass 1999, p. 126).

2.3.2 FIR Continuum Emission

Consider a cloud containing $\mathcal{N}$ spherical dust grains of uniform size, composition and temperature. We assume that the grains are spheres of radius $a \sim 0.1$ μm, and that each grain is in thermal equilibrium with the ambient radiation field. If the cloud is optically thin in the FIR, which is often the case, the flux density received by an observer is

$$F_\nu = \mathcal{N} \left\{ \frac{\pi a^2}{d^2} \right\} Q_\nu B_\nu(T_{\rm d}) \,, \tag{2.48}$$

where d is the distance to the cloud. The volume of dust in a cloud is given by

$$V = \frac{4}{3} \pi a^3 \mathcal{N} \,. \tag{2.49}$$

Using equation (2.48) to eliminate $\mathcal{N}$, equation (2.49) becomes

$$V = \frac{4 a F_\nu d^2}{3 Q_\nu B_\nu(T_{\rm d})} \,. \tag{2.50}$$

If the grains are composed of material of density $\rho_{\rm s}$, the total dust mass $M_{\rm d}$ is expressed as

$$M_{\rm d} = V \rho_{\rm s} = \frac{4 \rho_{\rm s} F_\nu d^2}{3 B_\nu(T_{\rm d})} \left\{ \frac{a}{Q_\nu} \right\} \,. \tag{2.51}$$

In the small-particle approximation, the quantity a/Q_ν is independent of a and depends only on the refractive index at wavelength λ. Adopting a suitably weighted average of a/Q_ν, equation (2.51) may thus be used to estimate the total mass of dust in a cloud from the observed flux density *without detailed knowledge of the grain size distribution.*

Part II

Evolution of Dust Content in Galaxies

Chapter 3

Dust-to-Gas Ratio and Metallicity

3.1 Overview of the Dust Formation and Destruction

Interstellar dust is composed of heavy elements made in and ejected from stars. An important source for the dust is stellar mass loss. For example, dust was clearly detected in the SN 1987A event (Moseley et al. 1989; Lucy et al. 1991). Dwek & Scalo (1980) presented that supernovae (SNe) are dominant sources for the formation of dust grains based on their chemical evolution model (but see Gehrz 1989). The formation of dust in SN 1987A was treated in e.g., Kozasa, Hasegawa, & Nomoto (1989) by using a nucleation theory. Todini & Ferrara (2001) calculated the mass of dust formed in SNe for various progenitor mass. The wind from stars also plays an important role in dust supply in the interstellar spaces (e.g., Whittet 1992, §7.1.3). Observations of infrared (IR) emission in stellar winds support the existence of dust grains (Whittet 1992 and references therein). The wind from cool stars can indeed be as cool as grain condensation temperature (1000–2000 K). Gilman (1969) proposed a grain composition in such a wind.

The dust growth in molecular clouds also contributes to the increase of dust mass. It is known that only the stellar source cannot account for the Galactic dust content (e.g., Gehrz 1989), since the supply timescale of the dust by stellar sources is ~ 1 Gyr while the destruction timescale is a few$\times 10^8$ yr. It is naturally explained by considering the dust growth in molecular clouds. Such a growth is supported by elemental depletions (Savage & Sembach 1996) and large grain sizes (Cohen 1977) in dense clouds. The chemical evolution model by Dwek (1998) was successful in explaining the dust content in the Galaxy by considering the dust growth in molecular clouds. This growth seems to be efficient in other spiral galaxies (Hirashita 1999a, hereafter H99).

Destruction processes of dust grains are also efficient in the formation timescale above (a few $\times 10^8$ yr). Interstellar shocks are known to destroy grains efficiently from observations (Routly & Spitzer 1952) and from theory (Cowie 1978). It is generally accepted that destruction is mainly due to the SN-generated shocks that propagate in the low-density interstellar medium (Barlow 1978; Draine & Salpeter 1979; Dwek & Scalo 1980; McKee et al. 1987; Jones et al. 1994; Borkowski & Dwek 1995; Jones, Tielens, & Hollenbach 1996). Crinklaw, Federman, & Joseph (1994) showed increasing gas phase abundance of heavy elements with decreasing density along the line of sight. This is naturally explained by considering that low density gas has high probability of having been exposed to SN shocks. The inclusion into newly formed stars in star-forming regions also contributes to the destruction process, but this contribution is less than that by SN shocks (Gehrz 1989).

Recently, galaxy-evolution models including the evolution of dust content have been developed (Wang 1991; Lisenfeld & Ferrara 1998, hereafter LF98; Dwek 1998, hereafter D98; Takagi, Arimoto, & Vansevičius 1999) by extending the chemical evolution model (e.g., Tinsley 1980). The formation and destruction processes described above can be included in the modeling. An extensive study was conducted by Dwek (1998), whose framework can be applied to the dust abundance of any galactic system. Lisenfeld & Ferrara (1998) focused on the relation between the dust-to-gas ratio and the metallicity of dwarf irregular galaxies and blue compact dwarf galaxies.

H99 also modeled the evolution of dust-to-gas ratio as a function of metallicity. Though his model is based on one-zone[1] treatment of galaxies, it includes and parameterizes all the formation and destruction processes above. &The importance of outflow from dwarf galaxies is stressed in In this chapter, we discuss the framework by H99. The following merits of H99 is stressed here:

1. The relation between the dust-to-gas ratio and the metallicity is derived. The relation will be very useful in estimating the dust content in galaxies whose metallicity is known. It is also helpful in examining the relation between the far-IR luminosity and the metallicity (Takagi et al. 1999; Hirashita, Inoue, & Kamaya 2000).

2. The model is as simple as possible. The galaxies are treated as one zone and some approximations (e.g., instantaneous recycling approximation; see §3.3 for details) are applied. This simplicity helps us to examine the response of the relation between the dust-to-gas ratio and metallicity to various physical parameters (§3.4).

3.2 Model Description

In this section, we derive the model equations which describe the dust content in a galaxy. The model is based on the chemical evolution model as described in Tinsley (1980). First, we estimate the quantities related to the dust formation and destruction. Then, we construct a set of model equations. We treat a galaxy as one zone to concentrate on global properties of galaxies. The simplicity of one-zone treatment has an advantage that the responses to change of parameters concerning the chemical evolution are easily tested.

3.3 Basic Equations

As mentioned in the previous section, we treat a galaxy as one-zone for simplicity. The time evolution of the gas mass in a galaxy is determined by the infall rate from the halo, F, the outflow rate, W, the consumption by star formation, ψ, and the recycling from stellar mass loss, E. Then, the time evolution of the gas mass is described by

$$\frac{dM_{\rm g}}{dt} = -\psi + E + F - W\,. \tag{3.1}$$

The time evolution of the mass of the heavy element i (i = O, C, Si, Mg, Fe, etc.) in the whole galaxy (including that in dust) is expressed as

$$\frac{{\rm d}M_i}{{\rm d}t} = -X_i\psi + E_i + X_i^{\rm f}F - X_i^{\rm w}W\,, \tag{3.2}$$

[1]The approximation that neglects or averages the spatial distribution of quantities and only concentrate on their time evolution.

where $X_i^{\rm f}$ and $X_i^{\rm w}$ are the abundance of i in the infalling and outflowing materials, respectively. The time evolution of $M_{{\rm d},i}$ (the mass of metal i locked up in dust grains) is estimated as

$$\frac{{\rm d}M_{{\rm d},i}}{{\rm d}t} = \left[\frac{{\rm d}M_{{\rm d},i}}{{\rm d}t}\right]_* + \left[\frac{{\rm d}M_{{\rm d},i}}{{\rm d}t}\right]_{\rm acc} + \left[\frac{{\rm d}M_{{\rm d},i}}{{\rm d}t}\right]_{\rm SF} + \left[\frac{{\rm d}M_{{\rm d},i}}{{\rm d}t}\right]_{\rm SN} + \left[\frac{{\rm d}M_{{\rm d},i}}{{\rm d}t}\right]_{\rm in} + \left[\frac{{\rm d}M_{{\rm d},i}}{{\rm d}t}\right]_{\rm w}\,. \tag{3.3}$$

Each term on the left-hand side is explained in the following subsection.

3.3.1 Dust Formation Processes

Formation in Stellar Mass Loss

Grains are supplied by the stellar mass loss from evolved stars and SNe. According to Gehrz (1989) evolved stars are dominant over SNe, while SNe are considered to be dominant in Dwek & Scalo (1980). Here, we parameterize the "effective condensation efficiency ($f_{{\rm in},i}$)" of the metal element labeled as i injected from stellar sources as

$$\left[\frac{{\rm d}M_{{\rm d},i}}{{\rm d}t}\right]_* = f_{{\rm in},i}\,E_i\,, \tag{3.4}$$

where $[{\rm d}M_{{\rm d},i}/{\rm d}t]_*$ means the rate of dust injection from stellar sources (evolved stars or SNe) into interstellar medium, $f_{{\rm in},i}$ is the condensation efficiency of heavy element labeled as i, and E_i is the injection rate of metal i from stars.

Growth in Dense Clouds

The mass increase of dust in interstellar spaces occurs through the accretion of heavy elements onto preexisting dust grains (e.g., Dwek 1998). This process is the most efficient in dense environment (i.e., molecular clouds), where the collision between grains and heavy element occurs most frequently. The timescale of the dust growth $\tau_{\rm grow}$ in clouds is estimated as

$$\tau_{\rm grow} \simeq \frac{m_{\rm d}}{{\rm d}m_{\rm d}/{\rm d}t}\,, \tag{3.5}$$

where $m_{\rm d}$ is the typical mass of a grain. If a spherical grain is assumed, we obtain the following expression for the growth of the mass:

$$\frac{{\rm d}m_{\rm d}}{{\rm d}t} = \pi a^2 v_{\rm m} n_{\rm m} A m_{\rm H} \xi_{\rm m}\,, \tag{3.6}$$

where a is the size of the grain; $v_{\rm m}$, $n_{\rm m}$, and $Am_{\rm H}$ ($m_{\rm H}$ is the mass of a hydrogen atom) are the typical thermal velocity, the number density, and the mass of a metal atom, respectively; $\xi_{\rm m}$ is the sticking efficiency of the metal atoms onto grains (Spitzer 1978). This gives an estimation of $\tau_{\rm grow}$ as

$$\tau_{\rm grow} \simeq \frac{4as}{3v_{\rm m} n_{\rm m} A m_{\rm H} \xi_{\rm m}}, \tag{3.7}$$

where s is the material density of a grain. Apparently, $\tau_{\rm grow}$ depends on metallicity through $n_{\rm m}$.

The growth of dust content in the whole galaxy by the accretion of heavy elements, $[\mathrm{d}M_{\mathrm{d},i}/\mathrm{d}t]_{\mathrm{acc}}$, is estimated as

$$\sum_i \left[\frac{\mathrm{d}M_{\mathrm{d},i}}{\mathrm{d}t}\right]_{\mathrm{acc}} \simeq N_{\mathrm{d}} X_{\mathrm{cold}} \frac{\mathrm{d}m_{\mathrm{d}}}{\mathrm{d}t}\,, \tag{3.8}$$

where N_{d} is the number of grains in the galaxy and X_{cold} is the mass ratio of the cold gas to all the gas. In the above estimate, the factor X_{cold} indicates that only dust incorporated into cold clouds can grow through the accretion (e.g., Hirashita 1999b). Using equation (3.6), equation (3.8) reduces to

$$\sum_i \left[\frac{\mathrm{d}M_{\mathrm{d},i}}{\mathrm{d}t}\right]_{\mathrm{acc}} \simeq \sum_i \frac{M_{\mathrm{d},i} X_{\mathrm{cold}}}{\tau_{\mathrm{grow}}}\,, \tag{3.9}$$

where we assumed a spherical grain; i.e., $\sum_i M_{\mathrm{d},i} = 4\pi a^3 s N_{\mathrm{d}}/3$. For species of metal element i, we obtain

$$\left[\frac{\mathrm{d}M_{\mathrm{d},i}}{\mathrm{d}t}\right]_{\mathrm{acc}} \simeq \frac{M_{\mathrm{d},i} X_{\mathrm{cold}}}{\tau_{\mathrm{grow}}}\,. \tag{3.10}$$

The abundance of metal i is defined as

$$X_i \equiv \frac{M_i}{M_{\mathrm{g}}}, \tag{3.11}$$

where M_i and M_{g} are the total mass of metal i and gas in the galaxy, respectively. If we consider that a part of heavy-element atoms are tied up in grains, the effective abundance of metal possible to be accreted onto grains is lower than X_i. Defining f_i as the fraction of metal i that is absorbed by grains (i.e., $f_i \equiv M_{\mathrm{d},i}/M_i$), the effective abundance of metal is expressed as $(1-f_i)X_i$. Thus, we assume that

$$\left[\frac{\mathrm{d}M_{\mathrm{d},i}}{\mathrm{d}t}\right]_{\mathrm{acc}} \simeq \frac{M_{\mathrm{d},i} X_{\mathrm{cold}}(1-f_i)}{\tau_{\mathrm{grow}}}\,. \tag{3.12}$$

Here, we estimate τ_{grow}, the typical timescale of the dust growth in molecular clouds. We adopt the Galactic value for the simple parameterization. Estimating τ_{grow} (eq. [3.7]) at the solar metallicity (fractional abundance of metals by mass of 2×10^{-2} is assumed), we obtain

$$\tau_{\mathrm{grow}} = 3\times10^7 \xi_{\mathrm{m}}^{-1}\,, \tag{3.13}$$

where we put $a = 0.1$ μm, $s = 3$ g cm^{-3}, $A = 20$, and $T = 50$ K (equivalent to $v_{\mathrm{m}} = 0.14$ km s^{-1}).

3.3.2 Dust Destruction Processes

Incorporation into Stars

The dust mass incorporated into stars is estimated as

$$\left[\frac{\mathrm{d}M_{\mathrm{d},i}}{\mathrm{d}t}\right]_{\mathrm{SF}} = -\psi \mathcal{D}_i\,, \tag{3.14}$$

where ψ and $\mathcal{D}_i$ are the star formation rate and the mass ratio of metal i in the dust phase to that in the gas (i.e., $\mathcal{D}_i \equiv M_{\mathrm{d},i}/M_{\mathrm{g}}$), respectively. We should note that we adopt a one-zone model, so that $\mathcal{D}_i$ is an averaged dust-to-gas ratio in the whole galaxy.

Destruction by SN shocks

The destruction rate of dust by SN remnants (SNRs), $[\mathrm{d}M_{\mathrm{d},i}/\mathrm{d}t]_{\mathrm{SN}}$, is written as

$$\left[\frac{\mathrm{d}M_{\mathrm{d},i}}{\mathrm{d}t}\right]_{\mathrm{SN}} = -\mathcal{D}_i \epsilon M_{\mathrm{SNR}} R_{\mathrm{SN}}\,, \tag{3.15}$$

where ϵ is the grain destruction efficiency, M_{SNR} is the total mass of interstellar gas swept up by an SNR during its lifetime, and R_{SN} is the number of SNe (Type I and Type II) per unit time. We define τ_{SN} as

$$\tau_{\mathrm{SN}} \equiv \frac{M_{\mathrm{g}}}{\epsilon M_{\mathrm{SNR}} R_{\mathrm{SN}}}\,. \tag{3.16}$$

Using τ_{SN}, equation (3.15) is reduced to

$$\left[\frac{\mathrm{d}M_{\mathrm{d},i}}{\mathrm{d}t}\right]_{\mathrm{SN}} = -\frac{M_{\mathrm{d},i}}{\tau_{\mathrm{SN}}}\,. \tag{3.17}$$

According to McKee (1989), $\tau_{\mathrm{SN}} = 4\times10^8$ yr, consistent with Jones, Tielens, & Hollenbach (1996).

3.3.3 Infall and Outflow

The dust mass in a galaxy changes due to the infall and outflow. The dust mass increase via the infall, $[\mathrm{d}M_{\mathrm{d},i}/\mathrm{d}t]_{\mathrm{in}}$, is expressed as

$$\left[\frac{\mathrm{d}M_{\mathrm{d},i}}{\mathrm{d}t}\right]_{\mathrm{in}} = \mathcal{D}_i^{\mathrm{f}} F\,, \tag{3.18}$$

where $\mathcal{D}_i^{\mathrm{f}}$ and F are the dust-to-gas ratio of infalling gas and the infall rate of gas, respectively.

The changing rate of dust mass in the galaxy through the outflow (galactic wind) is described as

$$\left[\frac{\mathrm{d}M_{\mathrm{d},i}}{\mathrm{d}t}\right]_{\mathrm{w}} = -\mathcal{D}_i^{\mathrm{w}} W\,, \tag{3.19}$$

where $\mathcal{D}_i^{\mathrm{w}}$ and W are the dust-to-gas ratio of the wind and the outflow rate of gas, respectively.

3.3.4 Instantaneous Recycling Approximation

For an analytical convenience, we adopt the instantaneous recycling approximation. We posit that stars less massive than m_{l} live forever and the others die instantaneously (Tinsley 1980). With this assumption, we express E and E_i as

$$E = \mathcal{R}\psi, \tag{3.20}$$

$$E_i = (\mathcal{R}X_i + \mathcal{Y}_i)\psi, \tag{3.21}$$

where $\mathcal{R}$ is the returned fraction of the mass that has formed stars, which is subsequently ejected into interstellar space, and $\mathcal{Y}_i$ is the mass fraction of the element i newly produced

and ejected by stars.[2] The two quantities, $\mathcal{R}$ and $\mathcal{Y}_i$, can be obtained using the following formulae:

$$\mathcal{R} = \int_{m_l}^{m_u} [m - w(m)]\phi(m)\,\mathrm{d}m\,, \tag{3.22}$$

$$\mathcal{Y}_i = \int_{m_l}^{m_u} m p_i(m)\phi(m)\,\mathrm{d}m\,, \tag{3.23}$$

where $\phi(m)$ is the initial mass function (IMF), which is normalized so that the integral of $m\phi(m)$ in the full range of the stellar mass becomes unity, m_u is the upper mass cutoff of stellar mass, $w(m)$ is the remnant mass of a star whose mass is m, and $p_i(m)$ is the fraction of mass converted into the element i in a star of mass m.

Using the above parameters, $\mathcal{R}$ and $\mathcal{Y}_i$, equations (3.1) and (3.2) become

$$\frac{\mathrm{d}M_g}{\mathrm{d}t} = -(1-\mathcal{R})\psi + F - W\,, \tag{3.24}$$

$$\frac{\mathrm{d}M_i}{\mathrm{d}t} = -(1-\mathcal{R})X_i\psi + \mathcal{Y}_i\psi + X_i^f F - X_i^w W\,. \tag{3.25}$$

Finally equation (3.3) is reduced to

$$\frac{\mathrm{d}M_{d,i}}{\mathrm{d}t} = f_{in,i}(\mathcal{R}X_i + \mathcal{Y}_i)\psi + \frac{M_{d,i}\,X_{cold}(1-f_i)}{\tau_{grow}} - \psi\mathcal{D}_i - \frac{M_{d,i}}{\tau_{SN}} + \mathcal{D}_i^f F - \mathcal{D}_i^w W\,. \tag{3.26}$$

3.4 Closed-Box Model

Here, we examine the case where the inflow and outflow of gas are neglected (i.e., $F = W = 0$). This case is often called "closed-box" model. This model has been a first step to understand the parameter dependence of the chemical enrichment in galaxies. Putting $F = W = 0$, equations (3.24)–(3.26) become

$$\frac{dM_g}{dt} = -(1-\mathcal{R})\psi\,, \tag{3.27}$$

$$\frac{dM_i}{dt} = -(1-\mathcal{R})X_i\psi + \mathcal{Y}_i\psi\,, \tag{3.28}$$

$$\frac{dM_{d,i}}{dt} = f_{in,i}(\mathcal{R}X_i + \mathcal{Y}_i)\psi + \frac{M_{d,i}\,X_{cold}(1-f_i)}{\tau_{grow}} - \psi\mathcal{D}_i - \frac{M_{d,i}}{\tau_{SN}}\,. \tag{3.29}$$

For analytical convenience, we modify these equations as

$$\frac{1}{\psi}\frac{dM_g}{dt} = -(1-\mathcal{R})\,, \tag{3.30}$$

$$\frac{M_g}{\psi}\frac{dX_i}{dt} = \mathcal{Y}_i\,, \tag{3.31}$$

$$\frac{M_g}{\psi}\frac{d\mathcal{D}_i}{dt} = f_{in,i}(\mathcal{R}X_i + \mathcal{Y}_i) - [\mathcal{R} + \beta_{SN} - \beta_{grow}(1-f_i)]\mathcal{D}_i\,, \tag{3.32}$$

[2] $\mathcal{R} = R$ and $\mathcal{Y}_i = y_i(1-R)$ in the notation of Lisenfeld & Ferrara (1998).

where we have defined the following two parameters:

$$\beta_{SN} \equiv \frac{M_g}{\tau_{SN}\psi}\,, \tag{3.33}$$

$$\beta_{grow} \equiv \frac{M_g X_{cold}}{\tau_{grow}\psi}\,. \tag{3.34}$$

Generally both β_{SN} and β_{grow} are functions of time, but we assume that these are constants for the reason as follows. Recall the definition of τ_{SN} in §3.3.2; $\tau_{SN} \equiv M_g/(\epsilon M_{SNR} R_{SN})$. Because the dependence of M_{SNR} on the gas density is weak (McKee 1989), $\tau_{SN} \propto M_g/R_{SN}$ if we assume the efficiency of the dust destruction, ϵ to be constant. If we assume that the rate of supernova R_{SN} is proportional to SFR ψ, $M_g/\tau_{SN}\psi = \beta_{SN} =$ constant. On the other hand, $\beta_{grow} \propto M_g X_{cold}/\psi$. If we assume the Schmidt law with index $n = 1$ (Schmidt 1959),[3] $\psi \propto M_g X_{cold}$. Thus, β_{grow} can be regarded as constant.

Now we estimate β_{SN} and β_{grow} by using the typical quantity of the Galaxy. First, τ_{SN} is estimated as 4.3×10^8 yr (McKee 1989). Moreover, the typical timescale of gas consumption, M_g/ψ, for a spiral galaxy is 10^9–10^{10} yr (Kennicutt, Tamblyn, & Congdon 1994). If we put $\tau_{SN} = 4.3 \times 10^8$ yr and $M_g/\psi = 5 \times 10^9$ yr, we find $\beta_{SN} \simeq 10$. On the other hand, we obtain $\beta_{grow} \simeq 8$, where we have used equation (3.13) and have assumed $\xi_m = 0.1$.

Combining equations (3.31) and (3.32), we obtain the following differential equation for $\mathcal{D}_i$ as a function of X_i:

$$\mathcal{Y}_i\frac{d\mathcal{D}_i}{dX_i} = f_{ini}(\mathcal{R}X_i + \mathcal{Y}_i) - (\mathcal{R} - \beta_{grow} + \beta_{SN})\mathcal{D}_i - \frac{\beta_{grow}\mathcal{D}_i^2}{X_i}, \tag{3.35}$$

where we used the relation of $f_i = \mathcal{D}_i/X_i$. We should note that $\mathcal{R}$ and $\mathcal{Y}_i$ are constant owing to the instantaneous recycling approximation.

3.4.1 Comparison with Observations

The result of the numerical integration of equation (3.35) is compared with observational data of nearby spiral galaxies. We take again $i = \mathrm{O}$. Moreover, we make an assumption that total mass of dust including both oxygen dust and carbon dust[4] is proportional to that of oxygen in the dust phase. In other words,

$$\mathcal{D} \equiv \sum_i \mathcal{D}_i = C\mathcal{D}_\mathrm{O}\,, \tag{3.36}$$

where C is assumed to be constant for all spiral galaxies. We adopt the Galactic value, $C \simeq 2.2$ according to Table 2.2 of Whittet (1992).

For further quantification, we need to fix the values of $\mathcal{R}$ and $\mathcal{Y}_i$ for the traced element ($i = \mathrm{O}$). We choose oxygen as the tracer, because (i) most of it is produced in type II SNe which are also responsible for the shock destruction of dust grains; (ii) oxygen is the main constituent of dust grains (see also LF98). The point (i) means that the instantaneous recycling approximation may be a reasonable approximation for the investigation of oxygen

[3] The star formation rate ψ and the gas mass M_g are often related as $\psi \propto M_g^n$. This relation is called as the Schmidt law after Schmidt (1959). Originally Schmidt assumed the relation between the star formation rate and gas density. After various observational examination, Schmidt proposed that $n = 1$–2.

[4] We should note that the carbon dust is not traced by oxygen. Here we make this assumption for simplicity.

abundances, since the generation of oxygen is a massive-star-weighed phenomenon. In other words, results are insensitive to the value of $m_{\rm l}$ defined in equations (3.22) and (3.23). According to LF98, we put $m_{\rm l} = 1\ M_\odot$ and $m_{\rm u} = 120\ M_\odot$. We use a power-law form of the IMF: $\phi(m) \propto m^{-x}$. Two kinds of the IMFs are investigated: $x = 2.35$ (Salpeter 1955) and more steep case: $x = 2.7$. If we assume that the lower cutoff[5] of the stellar mass is equal to $m_{\rm l}(= 1\ M_\odot)$, $(\mathcal{R},\ y_{\rm O}) = (0.79,\ 1.8 \times 10^{-2})$ and $(0.68,\ 9.6 \times 10^{-3})$ for the IMFs of Salpeter and Scalo, respectively (LF98). Evidently, stars with mass lower than $1\ M_\odot$ exist with a significant fraction in mass. So we adopt the lower cutoff of $0.1\ M_\odot$ instead. The values become $(\mathcal{R},\ y_{\rm O}) = (0.32,\ 7.2 \times 10^{-3})$ and $(0.13,\ 1.8 \times 10^{-3})$ for $x = 2.35$ and 2.7, respectively. We use the former values for $\mathcal{R}$ and $y_{\rm O}$ unless otherwise stated.

Dependence on $\beta_{\rm grow}$

First, we examine the dependence of $X_{\rm O}$–$\mathcal{D}$ relation on the parameter $\beta_{\rm grow}$, the efficiency of accretion of heavy element onto the preexisting dust grains. The result is shown in Figure 3.1*a*. The solid, dotted, dashed, dash-dotted lines represent the case where $\beta_{\rm grow} = 10$, 15, 5, and 0 respectively. The other parameters are set as $f_{\rm in,O} = 0.1$, $(\mathcal{R},\ y_{\rm O}) = (0.32,\ 7.2 \times 10^{-3})$, and $\beta_{\rm SN} = 5$. The metallicity is represented by [O/H]. We note that [O/H] $= x$ means that the abundance of oxygen is 10^x times the solar value (the solar oxygen abundance is assumed to be 0.013 in mass; e.g., Whittet 1992). We moreover assume that [O/H] $= \log(X_i/X_{i\odot})$ for all the elements. The data points are from Issa, MacLaren, & Wolfendale (1990; see also the references therein) by squares. The dust-to-gas ratio is calculated from the interstellar extinction and column densities of H I and H_2. Each value is evaluated at a galactocentric distance equivalent to that of the Sun (the galactocentric distance of each galaxy is properly scaled according to its size). The area marked with "dwarfs" represents a typical locus of dwarf irregular galaxies and blue compact dwarf galaxies (LF98).

The increase of $\beta_{\rm grow}$ means that accretion of heavy elements onto preexisting dust becomes efficient. Thus, for a fixed value of the metallicity, dust-to-gas ratio increases as $\beta_{\rm grow}$ increases. We also show the case of $\beta_{\rm grow} = 0$ and $\beta_{\rm SN} = 5$ (*dash-dotted line*), which is far from reproducing the data. This means that we should take into account the accretion onto the preexisting dust as Dwek & Scalo (1980) asserted. Thus, the models in LF98, which do not include the term of the accretion, cannot be applied to spiral galaxies. The equations in LF98 can be applied to dwarf galaxies, where the accretion process may be inefficient because of their low metallicity. The accretion process is properly considered in D98.

Dependence on $f_{{\rm in},i}$

In Figure 3.1*b*, the solid, dotted, and dashed lines show the $\mathcal{D}$–$X_{\rm O}$ relations for $f_{\rm in,O} = 0.4$, 0.1, and 0.01, respectively (in the case of $\beta_{\rm grow} = 2\beta_{\rm SN} = 10$ and the Salpeter IMF). In LF98, $f_{\rm in\,O} \simeq 0.4$ is suggested to be an optimistic upper limit. Figure 2 shows that the larger efficiency of metal production from heavy elements leads to the larger dust-to-gas ratio.

In the limit of $X_{\rm O} \to 0$, the solution of equation (3.35) reduces to $\mathcal{D} \simeq C f_{\rm in,O} X_{\rm O}$ (see also LF98), so that $\mathcal{D}$ scales linearly with $f_{\rm in,O}$. Thus, the precise value of $f_{\rm in,O}$ can be constrained by low-metal galaxies. Indeed, the difference among the three cases is significant

[5]The lower cutoff mass is different from $m_{\rm l}$. In this chapter, $m_{\rm l}$ is defined as the turn-off mass at the age of the galaxy.

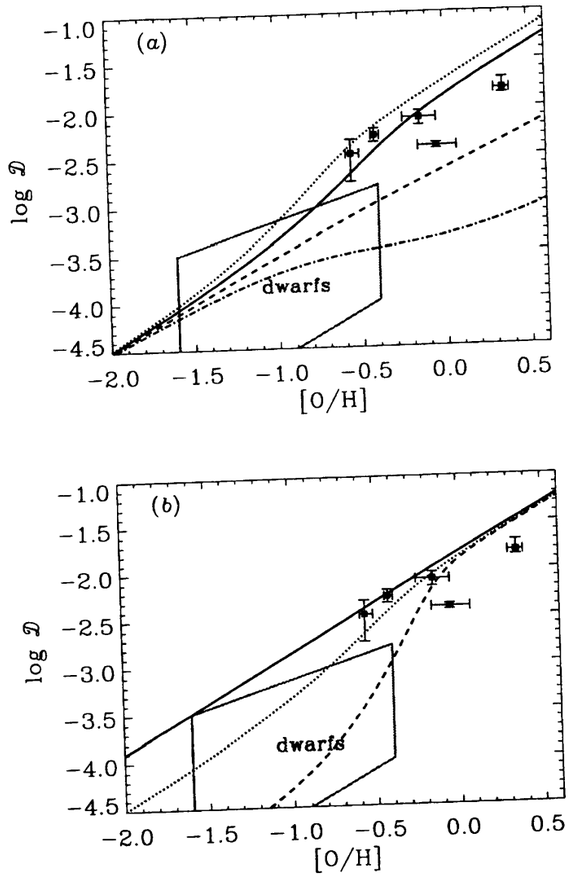

Figure 3.1: (*a*) Relations between dust-to-gas mass ratio ($\mathcal{D}$) and oxygen abundance (oxygen mass fraction $X_{\rm O}$) for various $\beta_{\rm grow}$ (dust accretion efficiency onto the preexisting dust grains). The data points shown with squares are for nearby spiral galaxies taken from Issa, MacLaren, & Wolfendale (1990). The area marked with "dwarfs" represents a typical locus of dwarf irregular galaxies and blue compact dwarf galaxies (Lisenfeld & Ferrara 1998). Here, $f_{\rm in,O} = 0.1$, $(\mathcal{R},\ y_{\rm O}) = (0.32,\ 7.2 \times 10^{-3})$, and $\beta_{\rm SN} = 5$ are assumed. The solid, dotted, and dashed lines represent the cases of $\beta_{\rm grow} = 10$, 15, and 5, respectively. The dash-dotted line shows the case of no accretion process onto the preexisting dust grains ($\beta_{\rm grow} = 0$ and $\beta_{\rm SN} = 5$). (*b*) Same as (*a*), but for various $f_{\rm in,O}$ (condensation efficiency of oxygen into dust grains). Here, $(\mathcal{R},\ y_{\rm O}) = (0.32,\ 7.9 \times 10^{-3})$, $\beta_{\rm grow} = 10$, and $\beta_{\rm SN} = 5$ are assumed. The solid, dotted, and dashed lines represent the cases of $f_{\rm in,O} = 0.1$, 0.5, and 0.01, respectively.

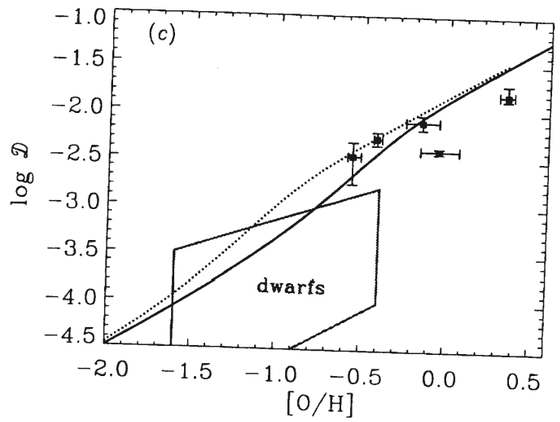

Figure 3.1: *Continued.* (*c*) Same as (*a*), but for various x (the slope of IMF). Here, $f_{\rm in,O} = 0.1$, $\beta_{\rm grow} = 10$, and $\beta_{\rm SN} = 5$ are assumed. The solid and dotted lines represent the cases of $x = 2.35$ and 2.7, respectively.

in the low-$X_{\rm O}$ region in Figure 3.1(*b*). It seems unlikely that $f_{\rm in,O} \lesssim 0.01$, since the data of the low-metal spirals cannot be reproduced by such small $f_{\rm in,O}$.

Dependence on IMF

The difference of mass function is reflected by different $\mathcal{R}$ and $y_{\rm O}$. We examine the case of $(0.32,\ 7.2 \times 10^{-3})$ and $(0.13,\ 1.8 \times 10^{-3})$ for $x = 2.35$ and 2.7, respectively. We present the result in Figure 3.1*c*. The results for $x = 2.35$ and 2.7 are represented by the solid and dotted lines, respectively. The differences among the results are too small (comparable to the typical observational errors) to determine which line is preferable.

3.4.2 Comment on the Expected Effect of Infall and Outflow

Infall

When the metallicity and the dust-to-gas ratio in the infall gas are much smaller than the interstellar value (i.e., $X_i^{\rm f} \ll X_i$ and $\mathcal{D}_i^{\rm f}$), the relation between the dust-to-gas ratio and the metallicity is not affected significantly. This is because equations (3.25) and (3.26) are not changed from the closed-box case. However, if the metallicity or dust-to-gas ratio is small as expected in the early phase of galaxy evolution, the pre-enrichment of the infall material may be important.

Outflow

The effect of the outflow was considered in LF98. The outflow influences the relation between the dust-to-gas ratio and the metallicity significantly if dust-to-gas ratio in the wind

is different from the value in the interstellar gas (i.e., $\mathcal{D}_i^w \neq \mathcal{D}_i$). However, if $\mathcal{D}_i^w \simeq \mathcal{D}_i$, the effect is not significant.

3.5 Summary and Conclusions

Based on the models proposed by LF98 and D98, we have examined the dust content in nearby spiral galaxies. We simplified the basic equations in D98 and applied the instantaneous recycling approximation to them. We treated one-zone model equations which describe the changing rate of dust-to-gas ratio including the terms of dust condensation from heavy elements ejected by stars, destruction by SN shocks, destruction in star-forming regions, and accretion of elements onto preexisting dust grains (§2.1). Assuming that the total dust mass is proportional to the mass of oxygen in the dust phase, we compared the results[6] with the data of nearby spiral galaxies (for the detailed comparison with the Galactic values, see D98, in which the data are excellently reproduced). Finally, we summarize the conclusions reached in this chapter:

[1] Unless we take into account the accretion process of heavy elements onto the pre-existing dust particles, we cannot explain the observed relations between dust-to-gas ratio and metallicity of nearby spiral galaxies. The accretion process is important for high-metallicity systems, since the collision rate between heavy-element atoms and dust grains is large. The data of dwarf galaxies, which are generally low-metallicity systems, may be explained even if the accretion process is neglected (LF98). The recent model by D98 properly treated the accretion.

[2] The efficiency of dust production from heavy element (denoted by $f_{{\rm in}i}$) can be constrained by the galaxies with low metallicity. It is unlikely that $f_{{\rm in}i} \lesssim 0.01$.

[3] As for IMFs, the change of x from 2.35 to 2.7 do not significantly change the resulting relation between dust-to-gas ratio and metallicity. The change is smaller than the scatter of the observed quantities.

[6] We should keep in mind the uncertainty concerning the observational data (e.g., the uncertainty in CO-to-H_2 mass conversion factor; Arimoto, Sofue, & Tsujimoto 1996).

Chapter 4

Nonlinear ISM and Dust-to-Gas Ratio

In this chapter, we present an evolution model for the dust-to-gas ratio on a galactic scale in a nonlinear interstellar medium (ISM). In order to understand the process of dust formation and evolution, it is indispensable to understand the physical properties and time evolution of ISM. Now ISM is known to be composed of gas with various temperature and density. Thus, the ISM is understood as a multi-phase gas. The most popular is the three-phase model proposed by McKee & Ostriker (1977). In this chapter, we review each component of the three phases, and introduce a time-evolution model for the ISM by Ikeuchi & Tomita (1983), which describes a nonlinear evolution of fractional mass of each component. In order to examine the evolution observationally, we first consider the star formation history of spiral galaxies. The discussion is based on Hirashita & Kamaya (2000). Then, we examine the evolution of dust-to-gas ratio based on Hirashita (2000b).

4.1 Overview of ISM

Studies of the ISM contribute to our understanding of the structure, kinematics, and evolution of galaxies (Dahlem 1997). The activity of star formation, its spatial distribution, and its temporal change depend strongly on the properties of the interstellar gas from which stars can form. Observational studies of ISM naturally started in our local vicinity—within the Galaxy (Milky Way). Here we briefly review "multi-phased" ISM. We are especially interested in the three phases as described by McKee & Ostriker (1977); the cold, warm, and hot media. Various ISM components with a variety of physical properties are compiled in Myers (1978). The typical temperature and number density are listed in Table 4.1.

Table 4.1: Typical temperature T and number density n of each phase in ISM

Phase	T (K)	n (cm^{-3})
Cold	10^2	10
Warm	10^4	0.1
Hot	10^6	10^{-3}

Since the growth and destruction rates of grains depend on the temperature and density of gas, understanding the physical properties of multiphased ISM is important for dust content in the ISM.

4.1.1 The Cold Medium

The cold neutral phase of the ISM is usually traced with H I absorption lines (Mebold et al. 1982). Spiral or irregular galaxies are known to contain such a cold gas. This phase is primarily associated with molecular gas existing in compact clouds. Such clouds are usually traced with CO transition lines.

Dust grains grow in such a cold medium through the accretion of heavy element (chapter 3). The efficient growth of grains are made possible in the dense environment where the probability of collision between grains and metal atoms is high. The timescale of the dust growth is estimated to be 10^7–10^8 yr (chapter 3).

4.1.2 The Warm Medium

The Warm Neutral Medium

The warm neutral medium is traced with H I line emission at 21 cm. This line is ubiquitous in the Galaxy (Hartmann & Burton 1997). The emission line usually shows a larger line width than the absorption line originating from the cold medium. This may be interpreted as a larger thermal velocity corresponding to several $\times 10^3$ K.

The Warm Ionized Medium

The warm ionized medium is found via diffuse Hα emission and pulsar dispersion studies. Sensitive observations of Hα emission show a fairly widespread distribution in the Galaxy not confined to the vicinity of hot stars. This indicates that ionized hydrogen gas with $T \sim 10^4$ K must be present in large portions in the ISM.

4.1.3 The Hot Medium

The existence of a hot component with very low density (10^{-3}–10^{-2} cm^{-3}) has been inferred from observations of the soft X-ray background and the absorption of starlight by highly ionized species (O VI, N V, C IV, Si IV, etc.) in the ISM. McKee & Ostriker (1977) studied the evolution of a supernova (SN) remnant in a warm intercloud medium. They showed that for intercloud densities and SN rates consistent with the solar neighborhood, the population of SN would disrupt the medium in a very short time, forcing a transition to hot phase domination (but see Slavin & Cox 1992, who demanded that the warm intercloud medium could well be stable, filling most of interstellar space). From the discussion of mass and energy balance, McKee & Ostriker determined the density and temperature of the hot gas as $10^{-2.5}$ cm^{-3} and $10^{5.7}$ K, respectively.

4.2 Various Star Formation Activity: Observation

One of the tests for the evolution of ISM on a galactic scale is to examine the star formation activities of galaxies, since stars are considered to form from the self-gravitational collapse

of ISM. In this section, we propose a scenario of star formation histories in giant spiral galaxies from the viewpoint of the three-phase model of ISM. Our standpoint is based on a very interesting observational result presented in Kennicutt, Tamblyn, & Congdon (1994, hereafter KTC94). According to their sample galaxies, there is a difference in present star-formation activity among morphological types of spiral galaxies (their §5.2). They used equivalent width of Hα as an indicator of star formation activity. The early-type spiral galaxies have a one-order-of-magnitude variety in b, which denotes the present-to-past ratio of star-formation rate (SFR), as being $b = 0.01$–0.1. On the other hand, $b = 0.5$–2, a range of just a small factor, in the late-type spiral sample.

There are various indicators of star formation rate of galaxies (Kennicutt 1998a; chapter 5). One of them is the far-infrared (FIR) luminosity. Tomita, Tomita, & Saitō (1996) found a difference in present star-formation activity among different morphological types of spiral galaxies (see also Devereux & Hameed 1997) from the FIR-to-B luminosity ratio. Tomita et al. (1996) commented that this variation may be a short-term change in the SFR in spiral galaxies and the duration of an episode of star formation activity is $\lesssim 10^8$ yr.

Color of galaxies is also an indicator of star formation activity (Tinsley 1980). Recently, Tomita, Takeuchi, & Hirashita (1999) examined the $U - V$ color and found the same trend as KTC94 among morphological types.

A theoretical interpretation for the various level of star formation activities in spiral galaxies is put by Kamaya & Takeuchi (1997, hereafter KT97). They pointed out that the short-term variation of star formation activity proposed by Tomita et al. (1996) may indicate that the ISM in a spiral galaxy is a non-linear open-system. That is, they suggested that the duration may result from the period of a limit cycle of mass exchange among various phases of the ISM (see Ikeuchi & Tomita 1983, hereafter IT83, for the limit-cycle behavior; see also Scalo & Struck-Marcell 1986). The word "open" indicates that a system exchanges mass and/or energy with the outside. In the case of Ikeuchi & Tomita, the system receives energy from SNe and radiate outside.

If the ISM in a galaxy is regarded as a non-linear open-system on a galaxy-wide scale, a limit-cycle star formation history may become possible (a general treatment for the emergence of a limit-cycle solution is described in §4.3.2). Indeed, the variance of the star formation activities of spiral galaxies can be understood as a short-term ($\lesssim 10^8$ yr) variation of their activities. Recent result by Rocha-Pinto et al. (2000) suggests that the Galactic star formation history indeed shows such a galaxy-wide variability (but the timescale is longer: Takeuchi & Hirashita 2000; Hirashita, Burkert, & Takeuchi 2001).

KT97's discussion was based on the sample of Tomita et al. (1996). In the subsequent discussions, we re-examine KT97's proposal more quantitatively than their original considerations through a comparison with KTC94. Moreover, we examine whether their scenario is consistent with the difference of SN rate among the morphological types of spirals, since the amplitude of the limit-cycle orbit is determined by the SN rate (§4.4). Thus, we can state clearly our motivation here. We aim to interpret the difference in star formation history among morphological types in the framework of the limit-cycle model of ISM in spiral galaxies.

According to a review by Ikeuchi (1988), he and his collaborators indicated that we might understand the dynamical evolution of the ISM on a galaxy-wide scale if we could describe galaxies as nonlinear open systems. (See also Nozakura & Ikeuchi 1984, 1988 and Tainaka, Fukazawa, & Mineshige 1993 for the spatial structure. We focus on the temporal behavior. In the future work, the spatial structure should be examined to see how large coherent structure

appears.) Here, we stress that one type of their models, the limit-cycle model, indicates a periodic star formation history (KT97). To understand the behavior of star formation activity of spiral galaxies, we focus on this interesting hypothetical behavior of the ISM. Adopting the limit-cycle model, KT97 insisted that the amplitude of the cyclic part of the SFR, Ψ', should be larger than the SFR of the quiescent era, $\bar{\Psi}$. Moreover, adopting a Schmidt (1959) law of index of 2, they predicted that the amplitude ratio of Ψ's, defined as $\mathrm{Max}(\Psi')/\mathrm{Min}(\Psi')$, should be ~ 50. Here, $\mathrm{Max}(\Psi')$ and $\mathrm{Min}(\Psi')$ indicate the maximum and minimum values of Ψ', respectively. However, since $\mathrm{Max}(\Psi')/\mathrm{Min}(\Psi')$ depends on the characteristic parameters for the limit-cycle model (IT83; or §4.3), we re-examine the amplitude for various parameters.

4.3 Cyclic Star Formation History: Model

Since our discussions are based mainly on KTC94, we summarize KTC94. KT97 is also reviewed. Although KT97's discussion is based on Tomita et al. (1996), their argument on the duration and the behavior of star formation activity is not altered even if we are based on KTC94.

Treating a data set of Hα equivalent widths of galactic disks with various morphologies, KTC94 have shown that the star formation activities present a wide spread for each morphological type (KTC94's Fig. 6). They derived b parameter which indicates the ratio of the present SFR to the past-averaged SFR.

Based on KT97, we re-interpret Figure 6 in KTC94: The KTC94's wide dispersion of the star formation activity is interpreted as evidence for a periodic or intermittent star-formation history on the scale of a giant galaxy. If galaxies have the same morphological type and the same age, such a large scatter as that in Figure 6 of KTC94 should not appear for near constant or monotonically declining SFRs. However, if cyclic star formation occurs in any spiral galaxy, we can easily understand why such a large scatter emerges. If the period of the cyclic star formation is several times 10^7 years, the dispersions in KTC94's Figure 6 do not contradict the hypothesis of KT97 by setting $b = \psi'/\bar{\psi}$, where ψ' and $\bar{\psi}$ are the cyclic and past-averaged SFR, respectively.

Indeed, such a periodic star formation history is proposed by Ikeuchi (1988) as cited by KT97. His discussion is based on the limit-cycle behavior of the fractional mass of each ISM shown by IT83. If the fractional component of the cold gas, where stars are formed, cyclically changes on a short timescale ($\sim 10^7$–10^8 yr), the SFR also varies cyclically. Thus, we review the formulation by IT83 in the next subsection.

4.3.1 Limit-Cycle Model of ISM (Ikeuchi–Tomita Model)

We review the limit-cycle model for the ISM proposed by IT83 (see also Scalo & Struck-Marcell 1986). The model has been utilized to interpret Tomita et al. (1996) (KT97). The limit-cycle behavior emerges if we treat the ISM as a non-linear open system. As long as the ISM is a non-linear open system, it spontaneously presents a dissipative structure (Nozakura & Ikeuchi 1984).

First of all, we should note that the galaxy disk is treated as one zone. The ISM is assumed to consist of three components each with its temperature T and density n (McKee & Ostriker 1977); the hot rarefied gas ($T \sim 10^6$ K, $n \sim 10^{-3}$ cm^{-3}), the warm gas ($T \sim 10^4$ K, $n \sim 10^{-1}$ cm^{-3}), and the cold clouds ($T \sim 10^2$ K, $n \sim 10$ cm^{-3}). The fractional masses

of the three components are denoted by X_h, X_w, and X_c, respectively. A trivial relation is

$$X_\mathrm{h} + X_\mathrm{w} + X_\mathrm{c} = 1. \tag{4.1}$$

The following three processes are considered in IT83 (see also Habe, Ikeuchi, & Tanaka 1981): [1] the sweeping of the warm gas into the cold component at the rate of $a_* X_\mathrm{w}$ ($a_* \sim 5 \times 10^{-8}$ yr^{-1}); [2] the evaporation of cold clouds embedded in the hot gas at the rate of $b_* X_\mathrm{c} X_\mathrm{h}^2$ ($b_* \sim 10^{-7}$–10^{-8} yr^{-1}); [3] the radiative cooling of the hot gas by mixing with the ambient warm gas at the rate of $c_* X_\mathrm{w} X_\mathrm{h}$ ($c_* \sim 10^{-6}$–10^{-7} yr^{-1}). Writing down the rate equations and using equation (4.1), IT83 obtained

$$\frac{\mathrm{d}X_\mathrm{c}}{\mathrm{d}\tau} = -BX_\mathrm{c}X_\mathrm{h}^2 + A(1 - X_\mathrm{c} - X_\mathrm{h}), \tag{4.2}$$

$$\frac{\mathrm{d}X_\mathrm{h}}{\mathrm{d}\tau} = -X_\mathrm{h}(1 - X_\mathrm{c} - X_\mathrm{h}) + BX_\mathrm{c}X_\mathrm{h}^2, \tag{4.3}$$

where $\tau \equiv c_* t$, $A \equiv a_*/c_*$, and $B \equiv b_*/c_*$.

The solutions of equations (4.2) and (4.3) are classified into the following three types (IT83):

[1] $A > 1$; all the orbits in the (X_c, X_h)-plane reduce to the node (0, 1) (node type),

[2] $A < 1$ and $B > B_\mathrm{cr}$; all the orbits reduce to a stable focus $[(1-A)/(AB+1),\ A]$ (focus type),

[3] $A < 1$ and $B < B_\mathrm{cr}$; all the orbits converge on a limit-cycle orbit (limit-cycle type),

where $B_\mathrm{cr} \equiv (1 - 2A)/A^2$. Obviously, case [3] is important if we wish to predict a cyclic star formation history. According to the summary of the limit-cycle model by Ikeuchi (1988), the period of a cycle is several times 10^7 years, as depicted in his Figure 4. Since this period is much shorter than the characteristic timescales in galaxy evolution such as the gas consumption timescale (> 1 Gyr: KTC94's τ_R), the cyclic change of SFR will produce a scatter in the observed star formation activities in spiral galaxies even if their ages are similar. In Figure 4.1, we show the time evolution of the cold and hot components when $A = 0.38$ and $B = 1.0$.

4.3.2 Brief Review of Nonlinear System

When we raise our eyes toward the sky, we see clouds that has a spatial structure. The structure attracts scientists as well as poets. It is evident that the structure should be understood from a macroscopic, not a microscopic, viewpoint. The structure is sustained by the convection that continuously transport thermal energy. The system with macroscopic flow of energy and (or) material is generally called a nonequilibrium system or an open system. Since a linear system cannot sharpen the boundary of clouds, a nonlinearity is necessary to make the clouds sharply outlined. Thus, the system should be open and nonlinear to reproduce the structure of clouds.

Not only a spatial structure, but also a temporal behavior characterizes nonlinear systems. As an example of a model of nonlinear system, we consider equations (4.2) and (4.3). Defining two functions $F(X_1, X_2)$ and $G(X_1, X_2)$ as

$$F(X_1, X_2) \equiv -BX_1X_2^2 + A(1 - X_1 - X_2)\,, \tag{4.4}$$

$$G(X_1, X_2) \equiv -X_2(1 - X_1 - X_2) + BX_1X_2^2\,, \tag{4.5}$$

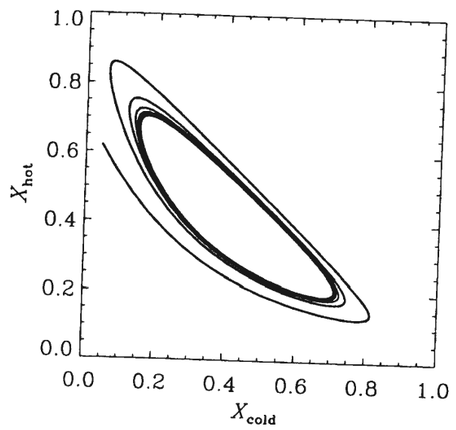

Figure 4.1: Time evolution of the fractional masses of the cold and the hot components, $X_{\rm cold}$ and $X_{\rm hot}$. The values for the parameters are set as $A = 0.38$ and $B = 1.0$. The initial condition is $(X_{\rm cold},\ X_{\rm hot}) = (0.0,\ 0.7)$.

we rewrite the model equations as

$$\frac{{\rm d}X_1}{{\rm d}\tau} = F(X_1,\, X_2)\,, \tag{4.6}$$

$$\frac{{\rm d}X_2}{{\rm d}\tau} = G(X_1,\, X_2)\,. \tag{4.7}$$

Here a general discussion for the non-linear system is made with the above set of equations. Such a type of equations is investigated in the field of the chemical reaction (Nicolis & Prigogine 1977).

First, we determine an equilibrium solution by solving $F(X_1,\, X_2) = G(X_1,\, X_2) = 0$. We denote the solution as $(X_1^0,\, X_2^0)$. The stability of this solution is examined by linearizing equations (4.6) and (4.7). For the linear analysis, we define perturbations x_1 and x_2 both of which have small (infinitesimal) amplitudes:

$$X_1 = X_1^0 + x_1\,, \tag{4.8}$$

$$X_2 = X_2^0 + x_2\,. \tag{4.9}$$

Dropping quantities that enter in equations (4.6) and (4.7) of any order higher than linear, we obtain

$$\frac{{\rm d}x_1}{{\rm d}\tau} = \left.\frac{\partial F}{\partial X_1}\right|_0 x + \left.\frac{\partial F}{\partial X_2}\right|_0 y \equiv ax + by\,, \tag{4.10}$$

$$\frac{{\rm d}x_2}{{\rm d}\tau} = \left.\frac{\partial G}{\partial X_1}\right|_0 x + \left.\frac{\partial G}{\partial X_2}\right|_0 y \equiv cx + dy\,, \tag{4.11}$$

where the subscript "0" indicates the value at $(X_1,\, X_2) = (X_1^0,\, X_2^0)$. We the functional form of x and y as

$$\begin{pmatrix} x_1 \\ y_1 \end{pmatrix} = \begin{pmatrix} x_1^0 \\ y_1^0 \end{pmatrix} \exp(\lambda\tau)\,, \tag{4.12}$$

where λ is the solution of

$$\begin{vmatrix} a-\lambda & b \\ c & d-\lambda \end{vmatrix} = 0\,. \tag{4.13}$$

The equilibrium state $(X_1^0,\, X_2^0)$ is stable if ${\rm Re}\,\lambda < 0$. However, if ${\rm Re}\,\lambda > 0$, the state is unstable. In this case, the system starting near $(X_1^0,\, X_2^0)$ evolves to another state. However, this evolution is often converged on a cycle in a nonlinear system. This cycle is called limit cycle. Such a cycle is present in case [3] in §4.3.1 and is investigated in IT83.

4.3.3 Oscillatory Model of SFR

According to KT97, we test the non-linear evolution of ISM. First, we define the present quiescent component of the SFR as $\bar{\psi}$ and the oscillatory component of the SFR as ψ'. Then, the total SFR is denoted as

$$\psi = \bar{\psi} + \psi'. \tag{4.14}$$

Our definitions are adequate when the period of oscillation of the SFR is much smaller than the cosmic age (e.g., Sandage 1986). According to Schmidt (1959), the SFR in a galaxy is approximately expressed as SFR $\propto n^p$ $(1 < p < 2)$, where n is the mean gas density of the galaxy. If we interpret n as the gas density of a cold cloud, which can contribute to the star formation activity, we expect the oscillatory part of the SFR to be

$$\psi' \propto X_{\rm c}^{1.5}, \tag{4.15}$$

where we have assumed that $p = 1.5$ (Kennicutt 1998b). Using this relation and equations (4.2) and (4.3), the variation of the star formation activity (i.e., ψ' as a function of τ) is calculated. For example, according to Figure 6 in Ikeuchi (1988), this mass fraction of the cold gas, $X_{\rm c}$, can vary from ~ 0.1 to ~ 0.9. Thus, we expect the magnitude of the variation of ψ' to be about two orders of magnitude during one period of the oscillation.

Since our model follows IT83, the structure of a model galaxy is hypothesized to be one-zone, that is, the local phenomena of the ISM are averaged in space. The simplicity of the one-zone approximation gives the advantage that the background physical processes are easy to see.

As a first step, we treat a model galaxy as being a one-zone object which is a non-linear open system. Habe et al. (1981) stated in their §7 that for the one-zone assumption to be acceptable it is necessary that the mean distance between SN remnants (SNRs) be less than 100 pc (if a characteristic lifetime of SNRs of $\tau_{\rm life} \sim 10^7$ yr and a mean expansion velocity of 10 km s^{-1} are adopted). This is because the SNRs should affect the whole disk for the one-zone treatment. The distance of less than 100 pc means that there are $N \sim 10^4$ SNRs in a galaxy disk, if the disk size of 10 kpc is assumed. This number is possible if SNe occur every 10^3 yr ($\tau_{\rm life}/N \sim 10^7$ [yr]$/10^4$). Considering that the SN rate in a spiral galaxy is typically

$1/100$–$1/50$ yr^{-1} (Cappellaro et al. 1993), the mean distance between SNRs is less than 100 pc even if 10–20 massive stars are clustered in a region.

Indeed, from the observational viewpoint, Rocha-Pinto et al. (2000) have shown that the star formation history of the Galaxy does present a short-term variability whose timescale is ~ 1 Gyr (see also Takeuchi & Hirashita 2000). Though they adopted the sample stars in the solar neighborhood, they showed by estimating the diffusion time of the stars that the sample represents the stars in the Galaxy-wide scale. Based on this observational evidence as well as the discussions in the previous two paragraphs, we accept the one-zone treatment by IT83 and apply it to the ISM on a galaxy-wide scale.

Once we accept the one-zone treatment, we need global observational measures of a galactic disk to examine our scenario. In this paper, the Hα equivalent width in KTC94 is the global physical parameter. KTC94 declared that their data excluded the bulge component and that they represent the disk component.

4.3.4 Application to KTC94

For the comparison between the model prediction and the observational data, we relate b defined in KTC94 (the ratio of the present SFR to the past-averaged SFR) to the model prediction. The parameter b is calculated from the equivalent width of Hα emission. According to KT97, we can assume that $b \simeq \psi'/\bar{\psi}$ if the large variance of b in Figure 6 of KTC94 originates from a short-term variation. We combine IT83's model with the star formation history via the Schmidt law (equation 4.15). For example, when $X_{\rm c} = 0.1$ at the minimum SFR and $X_{\rm c} = 0.7$ at the maximum (Fig. 1 of IT83), the value of $X_{\rm c}^p$ changes from 0.03 to 0.59 during the cycle if $p = 1.5$. Accordingly, we find that the maximum SFR is about 20 times larger than the minimum SFR, since ψ' is proportional to $X_{\rm c}^p$ (eq. [4.15]). Thus, using the cyclic star-formation scenario, we find the maximum of b also becomes 20 times larger than the minimum b in this numerical example.

To summarize, the large variance of b in Figure 6 of KTC94 is naturally derived, if the limit-cycle model is a real evolutionary picture of ISM. In the next section, we examine this point more precisely, in order to reproduce the variance of star formation activities for each morphological type of spiral galaxies. In the following discussions, we examine $\max(\psi')/\min(\psi')$, where $\max(\psi')$ and $\min(\psi')$ are maximum and minimum values of the oscillatory SFR (the maximum and minimum are defined by the maximum and minimum star formation rates during a period of the limit cycle, respectively), and thus $\max(\psi')/\min(\psi') \equiv \max(X_{\rm c}^p)/\min(X_{\rm c}^p)$. In the rough estimate in the previous paragraph, $\max(\psi')/\min(\psi')$ is 20 with $p = 1.5$. Here, we define

$$F_{\rm c} \equiv \frac{\max(\psi')}{\min(\psi')}, \tag{4.16}$$

for convenience in the subsequent sections. Using this relation and equations (4.2) and (4.3), the variation of the star formation activity (i.e., ψ' as a function of τ) is calculated, and $F_{\rm c}$ is evaluated finally.

4.4 Scenario of Limit-Cycle Star Formation

To propose a scenario of star formation history for spiral galaxies based on the limit-cycle model, let us start with a very interesting observational result. According to KTC94, the

early-type sample has a larger variance of SFR than the late-type sample. As a first step, we reconstruct this observational tendency in the framework of IT83. Then, we perform several numerical analyses to examine parameters which implement the limit-cycle oscillation of the cold phase of the ISM. For the ISM in spiral galaxies, the full possible ranges of the parameters of A and B (e.g., Habe et al. 1981) are $A = a_*/c_*$ of ~ 0.05 to ~ 0.5 and that $B = b_*/c_*$ of ~ 0.01 to ~ 1, respectively. In the following discussions, we focus on the parameter sets for the limit-cycle type (case [3] in §4.3.1).

Two of the results of differently parametrized limit-cycle behavior are displayed in Figures 4.2*a* and *b*, where the SFRs are normalized to the minimum SFR. In Figure 4.2*a*, we find an amplitude ($F_{\rm c}$) of about 10, which might correspond to the result of the Sa sample in KTC94. Figure 4.2*b* corresponds to the amplitude of about 4 for Sc in KTC94.

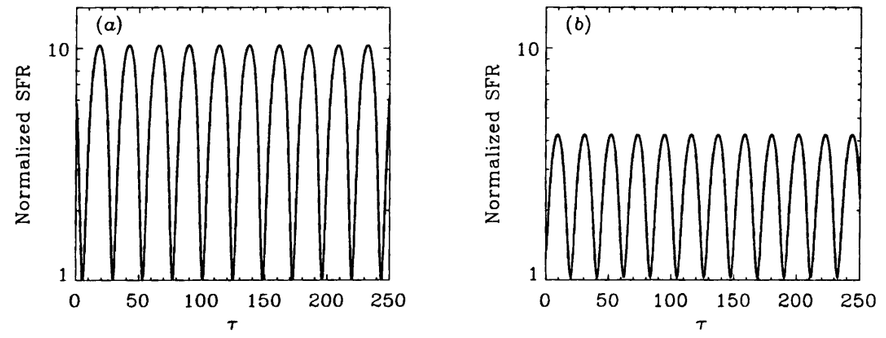

Figure 4.2: Time variation of SFR normalized by the minimum SFR. The timestep is normalized to the cooling time of the hot gas determined by the rate of mixing between hot and warm components ($\sim 10^6$ yr). (*a*) $A = 0.38$ and $B = 1.0$ are adopted to match the variance of the Sa sample in KTC94. The amplitude $F_{\rm c}$ is 10. (*b*) $A = 0.40$ and $B = 1.0$ match the variance of the Sc sample in KTC94. The amplitude $F_{\rm c}$ is 4.

Clearly, the difference in the amplitude between the Sa and Sc galaxies for the KTC94 data sets can be reproduced via the models which yield Figures 4.2*a* and *b*. We also present $F_{\rm c}$ for various A and B in Table 4.2, from which we observe that the value of $F_{\rm c}$ is more sensitive to A than to B. Indeed, from the rough estimate, $\delta F_{\rm c}/\delta A \sim -133/0.08 \sim -1600$ for $B = 1.0$ and $\delta F_{\rm c}/\delta B \sim -119/1.5 \sim -80$ for $A = 0.34$. Thus, the two figures are presented for different values of A. Here, we state an important point: The early-type spiral galaxies favor a small A, while the late-type ones are consistent with a large A.

The variation of the amplitude in accordance with A and B is qualitatively interpreted as follows. Small A (or small B) indicates that the transition from the warm to the hot component (or the cold to the warm component) is inefficient. Thus, when A (or B) is small, we must wait for $X_{\rm w}$ (or $X_{\rm c}$) to become large before the phase transition can become important, since the transition rate is described by $AX_{\rm w}$ (or $BX_{\rm c}X_{\rm h}^2$). Thus, the amplitude and the period become large for small A (or B). This interpretation of the relation between A (or B) and the amplitude is qualitatively robust. This means that the scenario proposed

Table 4.2: F_c as a function of A and B

		B			
		0.5	1.0	1.5	2.0
A	0.32	355	137	61	29
	0.34	129	52	24	10
	0.36	57	23	9	3
	0.38	27	10	4	—
	0.40	15	4	—	—

NOTE: We show the value of F_c if $B < B_c$ (the condition for the limit-cycle behavior) is satisfied. Otherwise, "—" is marked. See text for the definitions of quantities.

in this paper is unchanged even if a more elaborate model such as Ikeuchi, Habe, & Tanaka (1984) is used.

As a next step, we examine the SFR variance via the effect of A. According to the definition of A in §2.2, we expect a larger rate of SNe for large A (e.g., Sc) than for small A (e.g., Sa). Then, the result in the previous paragraph predicts an important point that the early-type spiral galaxies have smaller *present* SN rate than the late-type spirals. This is confirmed in the following two points:

[1] The higher SFR per unit optical luminosity in later type spiral galaxies (Figure 6 of KTC94) indicates that the Type II SN rate per unit optical luminosity is higher in later types. Thus, it is natural in the context of our model that the late-type spirals have larger A than the early-types.

[2] The expected trend of the SN rate for early-to-late types has been found by Cappellaro et al. (1993). They examine the SN rate per blue luminosity in various types of spirals, and present a summary of their results in their Table 4. We can confirm via their Table 4 that our scenario of limit-cycle SFR is consistent with the observational trend of SN rate as the galactic morphology varies. Moreover, the present SFR is reflected by the present rate of Type II SNe. According to Cappellaro et al., Sc-types show higher Type II SN rates than Sa types. Then, we can infer that the SFR of Sc galaxies is larger than that of Sa galaxies, which is compatible with Figure 6 of KTC94.

From these pieces of evidence, we find a consistent picture of the SFR variance in the spiral sample as a function of morphology via the scenario of the limit-cycle star formation history. We note that the large gas-to-stars mass ratio in late-type spiral galaxies is probably the reason for the large SFR, and that a larger mean SFR yields a smaller variance because of a larger SN rate.

The trend of F_c with varying B is also consistent with the different SN rates among morphological types. Since B physically means the efficiency of the evaporation of the cold component via conduction (one of the so-called SN feedback effects), B increases with increasing SN rate. Because a large value of B tends to reduce F_c as can be seen in Table 1, a small F_c is caused when the SN rate is large. Thus, from a similar argument to that in the previous paragraph, late-type spiral galaxies ought to have small values of F_c. Considering

the sensitivity of F_c to A (Table 4.2), however, we insist that A, not B, is the dominant contributor to the determination of the amplitude F_c.

4.5 Comments on Cyclic Star Formation History

4.5.1 Physical Mechanism

What is the underlying physical mechanism responsible for the variation in A and B? Since A and B are related to the Type II SN rate, this question reaches the most basic and unsolved question: What is the physical mechanism responsible for the different star formation activities among morphological types? First of all, recall that the later spirals have larger bulge-to-disk ratio than the earlier spirals. This can mean that the net volume of disk of the later spirals is larger than that of the earlier spirals. Once we accept the larger volume of disk of the later spiral galaxies, we expect that Type II SN rate per galaxy is higher in the late types than in the early types because of the large disk, where on-going star formation is generally observed. Moreover, the parameter c_* is determined from the mixing rate between the warm and hot gases. Then, if the volume of disk is effectively larger in the late types than in the early types, the late-type spirals may have smaller values of c_* than the early-types because the ISM will travel a larger distance before the mixing. Since $A = a_*/c_*$ and $B = b_*/c_*$, the late type spirals tend to have larger A and B than the early types. Therefore, as an implication, we propose that the size of the disk of galaxies is a factor that physically produces the difference in A and B among the morphologies of spirals.

We expect that the difference in A and B is produced by an interplay between the size effect described in the previous paragraph and the SN rate. In fact, the question has been answered from an observational viewpoint in §5.3 of KTC94 by stating

> "From an observational point of view, the progression in disk star formation histories with morphological type is not surprising, since one of the fundamental classification criteria is disk resolution, which should relate at least indirectly to the fraction of young stars in the disk."

We have presented a consistent picture for the variance of star formation activities in spiral galaxies by relating the differences in variance among morphological classes with the SN rate. However, since an earlier-type sample has a lower gas-to-stellar mass ratio, its mean SFR will be lower but its variance will in any case tends to be larger because of the stochastic fluctuations. In order to see whether the variance is caused by a purely stochastic process or not, an amplitude of a stochastic SFR should be given in a physically reasonable way. In other words, we should specify what kind of the stochastic process is physically reasonable. Though our model is not stochastic, it provides a way to give an amplitude of the variable SFR. To be fair, however, another modeling for the variation of the SFR, probably a stochastic modeling, may provide another interpretation for the variance of SFR in KTC94.

4.5.2 Star Formation History of the Milky Way

In the field of the chemical evolution of the Galaxy (the Milky Way), Eggen, Lynden-Bell, & Sandage (1962) have inspired the modeling. From the correlation between the ultraviolet (UV) excess and orbital eccentricity of stars, they concluded that the Galaxy formed by collapse on a free-fall timescale from a single protogalactic cloud. An alternative picture of

halo formation is proposed by Searle & Zinn (1978). They argued that Galactic system is formed from the capture of fragments such as dwarf galaxies over a longer timescale than that proposed by Eggen et al. In any case, determining the timescale of the infall of matter and the chemical enrichment is an important problem to resolve the formation mechanism of the Galactic system. Indeed, there have been a number of papers that investigated the formation and chemical evolution of the Galaxy (e.g., Matteucci & François 1989) and spiral galaxies (e.g., Lynden-Bell 1975; Sommer-Larsen 1996).

Observational study is now progressing. Recently, Rocha-Pinto et al. (2000) found from observed age distribution of the late-type stars that the star formation history of the Galaxy is indeed intermittent. Takeuchi & Hirashita (2000) compared the Rocha-Pinto et al.'s data with the prediction from the infall model, showing that the oscillatory behavior is statistically significant. Hirashita, Burkert, & Takeuchi (2001) constructed an infall model with an oscillatory star formation history.

Takeuchi & Hirashita (2000) suggested a two-component model for the star formation history in the Galaxy as

$$\psi_{\rm obs} = \psi_{\rm infall} + \varepsilon\,, \tag{4.17}$$

where $\psi_{\rm obs}$ and $\psi_{\rm infall}$ are the observed star formation history in Rocha-Pinto et al. (2000) and that in the best-fit infall model by Takeuchi & Hirashita (2000), respectively, and the residual, ε, is produced by a probability distribution with zero mean and dispersion σ^2. They simply assume that σ^2 is time-independent, showing that σ is comparable to $\psi_{\rm infall}$.

If we assume that the large variation of the SFR is typical of spiral galaxies, the star formation activities of them should show a variety. The large value of the variance (σ) is consistent with previous works that suggested the variety of star formation activities of spiral galaxies (Kennicutt et al. 1994; Tomita et al. 1996; Devereux & Hameed 1997). Furthermore, the kurtosis of the residual, $K = -0.81$, which means that ε is distributed flatly and is not strongly concentrated around the mean. Indeed, in Figure 8 of Tomita et al. (1996), there seems to be little concentration of star formation activity around the mean, which is consistent with the flat distribution shown by Takeuchi & Hirashita (2000).

4.5.3 Comment on Dwarf Irregular Galaxies

For the sample of dwarf irregular galaxies (dIrrs), a scatter of star formation activity, which may indicate intermittent star formation activities, is seen. For example, Marlowe et al. (1995) showed the age of the burst ranges from "on-going" to $\sim$ 1 Gyr. The equivalent widths of Hα also show a wide range of present star formation activities of dIrrs (Marlowe, Meurer, & Heckman 1999).

Hirashita (2000) examined the nature of the star-formation activities of dwarf irregular galaxies (dIrrs) by considering two processes: stellar feedback and cooling. The former is the heating process by stars (SNe, stellar winds, UV radiations, thermal conduction, etc.), and the latter is important to initiate the next star-formation activity. First, he phenomenologically applied the observed propagation velocity of star formation to an estimation of the propagation timescale. The typical timescale of the propagation is 10^{7-8} yr in dIrrs. Next, he estimated the cooling time of gas heated by the feedback mechanism. For dIrrs, the typical timescale for the cooling is nearly 1 Gyr, which is longer than the propagation timescale mentioned above. Comparing the two timescales, he finally suggested that the star-formation

activity of dIrrs are intermittent.[1] The small size (i.e., the short propagation timescale) and the small metallicity (i.e., the short cooling timescale) are both responsible for the intermittence. Efficient interstellar mixing may prevent intermittence, because it makes the cooling time shorter by an order of magnitude. Thus, an examination of the mixing efficiency is important for a thorough understanding of the star-formation histories of dIrrs.

4.6 Cyclic Change in Dust-to-Gas Ratio

Dust grains grow in cold clouds efficiently through the accretion of heavy element. This means that the dust-growth efficiency on a galaxy-wide scale depends on the fractional mass of the cold gas (Seab 1987; McKee 1989; Draine 1990; Hirashita 2000b). Thus, the efficiency varies on a timescale of the phase transition of the ISM.

Hirashita (2000b) combined the framework of Hirashita (1999a) with a theoretical work on multiphase ISM and suggested the time variation of the dust-to-gas ratio by the phase transition. In this chapter, we aim at constructing a model of the time evolution of dust-to-gas ratio including the effect of the ISM phase transition.

4.6.1 Basic Equations

In order to describe the change of the dust-to-gas ratio because of the phase transition of ISM, we should first model the time evolution of the dust-to-gas ratio in a galaxy. The basic equations in chapter 3 are adopted for this purpose. We also need a model for the ISM phase change. We apply the Ikeuchi–Tomita model (eqs. [4.2] and [4.3]), which describes the time evolution of the fractional masses of the three components in the ISM.

For the time evolution of the dust-to-gas ratio, we adopt the model in chapter 3. Equations (3.31) and (3.32) become

$$\tau_{\rm SF}\frac{dX_i}{dt} = \mathcal{Y}_i\,, \tag{4.18}$$

$$\tau_{\rm SF}\frac{d\mathcal{D}_i}{dt} = f_{{\rm in},i}(\mathcal{R}X_i + \mathcal{Y}_i) - [\mathcal{R} - \beta_{\rm grow}(1-f_i) + \beta_{\rm SN}]\mathcal{D}_i\,, \tag{4.19}$$

where $\tau_{\rm SF} \equiv M_{\rm g}/\psi$ (timescale of gas consumption; e.g., Roberts 1963). The timescales above are estimated in the case of typical spiral galaxies as $\tau_{\rm SF} \sim$ 1–10 Gyr (Kennicutt, Tamblyn, & Congdon 1994).

The timescale of dust growth is shorter if a galaxy contains a large amount of the cold gas. This can be seen from equation (3.34), which includes the dependence on $X_{\rm cold}$, the fractional mass of the cold component. This dependence indicates that the dust growth occurs most efficiently in the cold and dense environment. Since $X_{\rm cold}$ is changed temporally according to the Ikeuchi–Tomita model, we define a constant $\beta'_{\rm grow}$ as

$$\beta'_{\rm grow}X_{\rm cold} \equiv \beta_{\rm grow}\,. \tag{4.20}$$

The destruction timescale of the dust $\beta_{\rm SN}$ is kept constant for simplicity, since we would like to concentrate on the time variation of the dust growth efficiency. The star formation history should be taken into account in order to model the time dependence of $\beta_{\rm SN}$. Moreover,

[1] The shorter propagating timescale than the cooling timescale indicates that the system can be treated as a one zone. That is, the phase transition of the interstellar gas occurs coherently over the whole galaxy.

Table 4.3: Examined Models

Model No.	A	B	$c\tau_{\rm SF}$	type
1.....	1.2	3.0	100	runaway
2.....	0.4	3.0	100	stationary
3a.....	0.3	3.0	100	limit-cycle
3b.....	0.3	3.0	1000	limit-cycle
4a.....	0.3	0.5	100	limit-cycle
4b.....	0.3	0.5	1000	limit-cycle

the time variation of the SN rate also contributes to the time variation of the fractional masses of the three ISM components. Because of such complexities in the time dependence of $\beta_{\rm SN}$, we simply treat $\beta_{\rm SN}$ as constant.

The model by IT83 is used to calculate the time evolution of the filling factors of the three ISM phases. Their model was reviewed in §4.3.1. The result is used to calculate the dust formation efficiency, which is related to $X_{\rm cold}$ as explained in the previous subsection.

Following equations (4.2) and (4.3), we calculate the time evolution of the fractional mass. As representative parameter sets of the limit-cycle orbit, we examine the case of $(A,\ B) = (0.3,\ 3.0)$ and $(A,\ B) = (0.3,\ 0.5)$ (denoted by Models 3 and 4 in Table 4.3, respectively).[2] The cycle periods of the former case is about three times shorter than that of the latter.

In Table 4.3, the adopted parameters are summarized. The column "type" means the behavior of the solutions and named "runaway," "stationary" and "limit-cycle" for the cases [1], [2] and [3] in §4.3.1, respectively. We note that all the parameter sets above are examined in IT83 (their Figures 1 and 3).

Since we are interested in a timescale much shorter than $\tau_{\rm SF}$, which is also interpreted as metal-production timescale through equation (4.18), we treat X_i as constants. Then, equation (4.19) is solved for oxygen abundance ($i = {\rm O}$, because we adopted the oxygen as a tracer element in the previous work, Hirashita 1999b: see also Lisenfeld & Ferrara 1998):

$$c_*\tau_{\rm SF}\frac{{\rm d}\mathcal{D}_{\rm O}}{{\rm d}\tau} = f_{\rm in,O}(\mathcal{R}X_{\rm O} + \mathcal{Y}_{\rm O}) - [\mathcal{R} - \beta_{\rm grow}(1 - f_{\rm O}) + \beta_{\rm SN}]\mathcal{D}_{\rm O}\,, \tag{4.21}$$

where we express the time in a nondimensional manner by using $\tau = c_*t$. We note the relation $f_{\rm O} = \mathcal{D}_{\rm O}/X_{\rm O}$. We fix the parameters as $\tau_{\rm SF} = 3 \times 10^9$ yr (e.g., Kennicutt et al. 1994), $f_{\rm in,O} = 0.05$ (Hirashita 1999b), $\mathcal{R} = 0.32$, $\mathcal{Y}_{\rm O} = 7.2 \times 10^{-2}$ (chapter 3), $\beta'_{\rm grow} = 100$ (corresponding to $\tau_{\rm grow} = \tau_{\rm SF}/100 = 3 \times 10^7$ yr), $\beta_{\rm SN} = 10$ (Hirashita 1999a, b), and $X_{\rm O} = 0.013$ (the solar system abundance). The dependence on these parameters above are described in Lisenfeld & Ferrara (1998) and Hirashita (1999a, b) except for c_* and $\tau_{\rm SF}$. The parameter c_* scales the phase transition timescale, and we examine the cases of $c_*\tau_{\rm SF} = 100$ and 1000 (Table 4.3: $c_*^{-1} = 3 \times 10^6$–3×10^7 yr; IT83). We note that c_* appears in the form of the nondimensional parameter $c_*\tau_{\rm SF}$. We examine only the case of $c_*\tau_{\rm SF} = 100$ in Models 1 and 2, since the qualitative behavior of the dust-to-gas ratio is the same, irrespective of which value of $c_*\tau_{\rm SF}$ is adopted. Finally, the total dust-to-gas ratio $\mathcal{D}$ is calculated from equation (3.36).

[2]Two cases for each model are examined for different values of c_* (Models 3a, 3b, 4a, and 4b).

We solve the basic equations for the parameters listed in Table 4.3. The initial condition for the filling factors are set according to IT83: $(X_{\rm cold},\ X_{\rm hot}) = (0.0,\ 0.1)$ except for the Model 4 and $(X_{\rm cold},\ X_{\rm hot}) = (0.0,\ 0.7)$ for Model 4. The initial dust-to-gas ratio is set as $\mathcal{D} = 6 \times 10^{-3}$ (Galactic value; §2.2.4) for all the models. Models 3 and 4 are examined for two different values of c_* listed in Table 4.3. Fixing $\tau_{\rm SF} = 10^9$ yr, $c_*\tau_{\rm SF} = 100$ and 1000 mean $c_* = 10^{-7}$ yr^{-1} and 10^{-6} yr^{-1}, respectively.

4.6.2 Results

The result of Model 1 is displayed in Figure 4.3. Because the cold gas disappears, the dust growth becomes ineffective. Then the dust-to-gas ratio converge to $\sim 1.2 \times 10^{-4}$ in the dust destruction timescale ($\sim 3 \times 10^8$ yr, i.e., 10 in units of c_*^{-1}). The final value for the dust-to-gas ratio is determined by the equilibrium between the supply rate from stars and the destruction rate by SNe as shown later in equation (4.23).

Model 1 represents the efficient sweeping of warm gas in comparison with the radiative cooling of the hot gas. Thus, the swept gas is first converted into the cold component and then into hot gas (IT83). If the hot gas escapes out of the galaxy owing to its large thermal energy, this model corresponds to the galactic wind model of elliptical galaxies (IT83; Arimoto & Yoshii 1987).

The final value of the dust-to-gas ratio in Model 1 is calculated by considering a stationary state, ${\rm d}\mathcal{D}_{\rm O}/{\rm d}t = 0$, in equation (4.21):

$$\frac{\beta_{\rm grow}}{X_{\rm O}}\mathcal{D}_{\rm O}^2 + (\mathcal{R} - \beta_{\rm grow} + \beta_{\rm SN})\mathcal{D}_{\rm O} - f_{\rm in,O}(\mathcal{R}X_{\rm O} + \mathcal{Y}_{\rm O}) = 0\,. \tag{4.22}$$

Because of the constant dust injection from stars at the rate of $f_{\rm in,O}(\mathcal{R}X_{\rm O} + \mathcal{Y}_{\rm O})$, the dust-to-gas ratio is not exactly 0 even after a long time. Since $X_{\rm cold} = 0$, we have $\beta_{\rm grow} = 0$. Thus, the solution of equation(4.22) is

$$\mathcal{D} = C\mathcal{D}_{\rm O} = \frac{Cf_{\rm in\,O}(\mathcal{R}X_{\rm O} + \mathcal{Y}_{\rm O})}{\mathcal{R} + \beta_{\rm SN}} = 1.2 \times 10^{-4}\,, \tag{4.23}$$

for the adopted parameters $C = 2.2$, $X_{\rm O} = 0.013$, $f_{\rm in\,O} = 0.05$, $\mathcal{R} = 0.32$, $\mathcal{Y}_{\rm O} = 7.2 \times 10^{-3}$, and $\beta_{\rm SN} = 10$. This indeed matches the final value of the dust-to-gas ratio in Model 1.

Next, the result of Model 2 is presented in Figure 4.4. As shown in IT83, the solution for $X_{\rm cold}$ reduces to a stable point $(1 - A)/(AB + 1) = 0.27$ (i.e., $\beta_{\rm grow} = 27$). The stable stationary state is realized at a finite dust-to-gas ratio, which is determined so that the dust formation rate is balanced with the dust destruction rate. The value is calculated from equation (4.21). Putting the adopted parameters, the positive solution is $\mathcal{D} = C\mathcal{D}_{\rm O} \simeq 0.018$, which matches the stationary value in Figure 4.4. Analytically, the value is expressed as

$$\mathcal{D} = C\mathcal{D}_{\rm O} = \frac{\beta_{\rm grow} - \beta_{\rm SN} - \mathcal{R}}{\beta_{\rm grow}}CX_{\rm O}, \tag{4.24}$$

since $\beta_{\rm grow}\mathcal{D}_{\rm O} \gg f_{\rm in,O}(\mathcal{R}X_{\rm O} + \mathcal{Y}_{\rm O})$. This condition means that in dust mass increase the growth in clouds is more effective than the supply from stars.

Finally, the limit-cycle case is examined in Figures 4.5 and 4.6. The four sets of parameters listed in Table 4.3 are examined (Models 3a, 3b, 4a, and 4b). The resulting time evolution of the cold component of ISM and the dust-to-gas ratio is presented in Figures 4.5 and 4.6. As

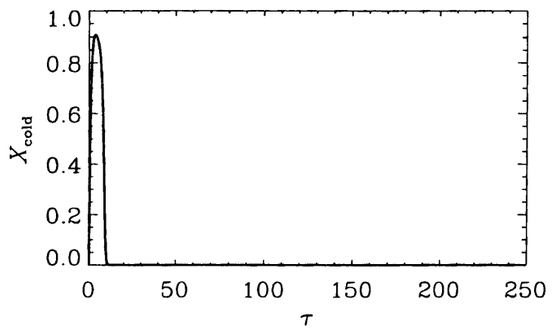

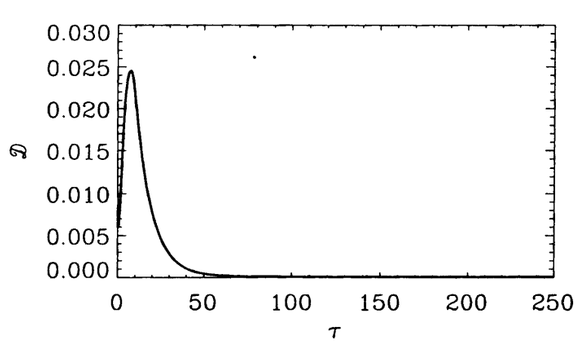

Figure 4.3: *Upper panel*: the time evolution of the the cold-gas mass filling factor ($X_{\rm cold}$) for Model 1. The initial condition is ($X_{\rm cold}$, $X_{\rm hot}$) = (0.0, 0.1). The adopted values of the parameters are $A = 1.2$, $B = 3.0$, and $c_*\tau_{\rm SF} = 100$. The timestep is normalized by $c^{-1} \simeq 3 \times 10^7$ yr. *Lower panel*: the time evolution of the dust-to-gas ratio ($\mathcal{D}$).

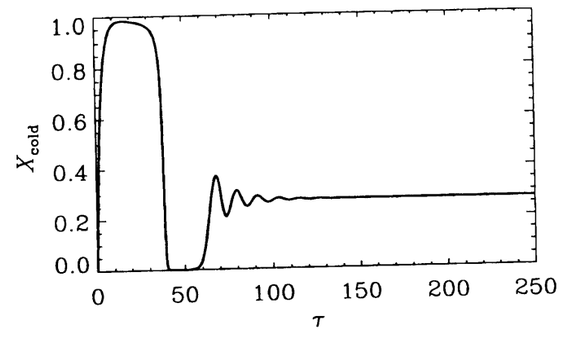

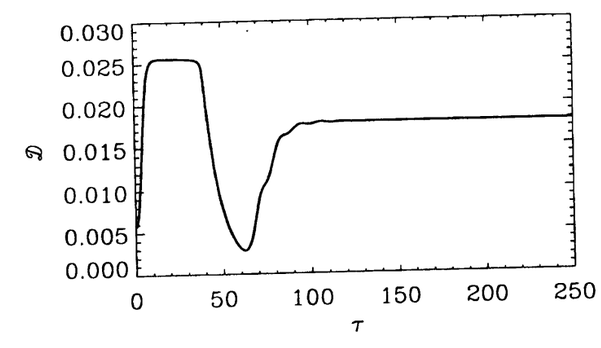

Figure 4.4: The same as Fig. 4.3, but for Model 2. The initial condition is ($X_{\rm cold}$, $X_{\rm hot}$) = (0.0, 0.1). The adopted values of the parameters are $A = 0.4$, $B = 3.0$, and $c_*\tau_{\rm SF} = 100$. The timestep is normalized by $c^{-1} \simeq 3 \times 10^7$ yr.

expected, the dust-to-gas ratio oscillates in response to the fractional mass variation of the cold component, though the amplitude of the variation largely depends on the parameters. Comparing Figures 4.5 and 4.6,[3] we see that the amplitude becomes larger if the period of the oscillation is longer. This is because the dust has enough time to grow if the period is long. Also from the comparison between the two lines in each figure, we find that the smaller c_* makes the amplitude larger. Since small c_* means that a timestep of the phase transition model (eqs. [4.2] and [4.3]) is long in the real time unit ($\tau = 1$ corresponds to $t = c_*^{-1}$), the dust has enough time to grow in the case of smaller c_*. The timescale of the dust growth relative to that of the phase transition determines the amplitude. This point is again discussed in the next section.

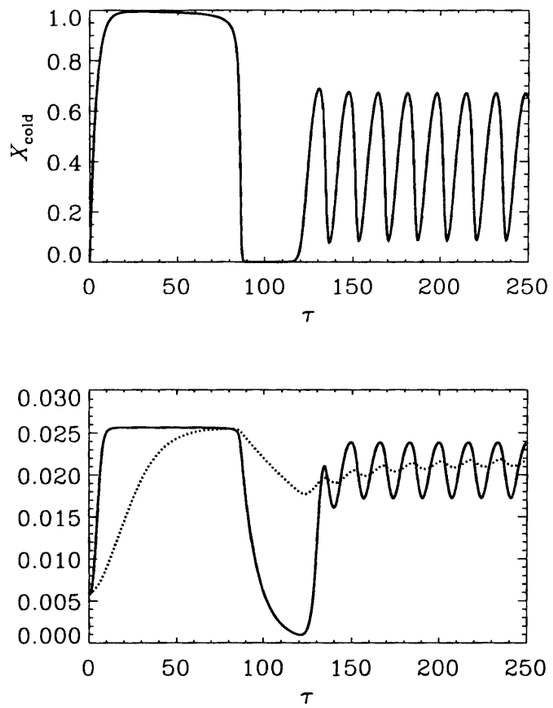

Figure 4.5: Same as Fig. 4.3, but for Model 3. The solid and dotted lines represents Models 3a and 3b, respectively. The initial condition is $(X_{\rm cold},\ X_{\rm hot}) = (0.0,\ 0.1)$.

[3]Models 3a and 4a (or Models 3b and 4b) should be compared.

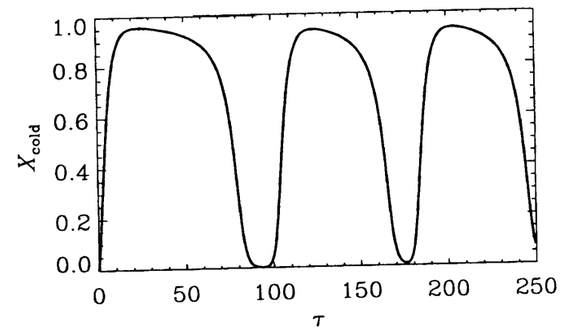

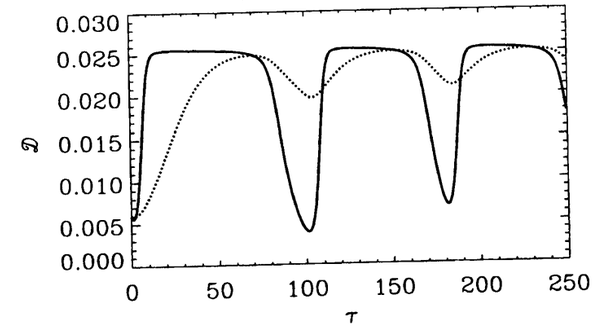

Figure 4.6: Same as Fig. 4.3, but for Model 4. The solid and dotted lines represents Models 4a and 4b, respectively. The initial condition is $(X_{\rm cold},\ X_{\rm hot}) = (0.0,\ 0.7)$.

4.7 Discussions

4.7.1 Timescales

In the runaway and stationary solutions (Models 1 and 2), the dust-to-gas ratio is settled into a stationary value determined by equation (4.22) after the dust formation and destruction timescales ($\sim 10^8$ yr). In the limit-cycle type solutions (Models 3 and 4), the amplitude of the dust-to-gas oscillation largely depends on the timescale of the phase transition. In this subsection, we discuss the phase-transition and dust-formation timescales in the limit-cycle model.

From the solution of the model equations (Figs. 4.5 and 4.6), we find that the dust-to-gas ratio oscillates in response to the filling factor of the cold component. However, the amplitude of the oscillation is highly dependent on the values of the parameters A, B, and c_*. In other words, the amplitude is determined by the relation between the timescale of the phase transition (or the period of the oscillation) and that of the dust growth timescale. In the following, we discuss the relation between the the period of the phase transition (denoted by $\tau_{\rm tr}$) and the dust growth timescale ($\tau_{\rm grow}$).

In order for the dust to grow, the dust must have enough time for the growth, i.e., $\tau_{\rm grow} < \tau_{\rm tr}$. This condition is equivalent to

$$\frac{\tau_{\rm grow}}{X_{\rm cold}} < \tau_{\rm tr}\,, \tag{4.25}$$

which reads the following inequality by using $\beta'_{\rm grow}$:

$$\frac{\tau_{\rm tr}}{\tau_{\rm SF}} > \frac{1}{\beta'_{\rm grow} X_{\rm cold}}. \tag{4.26}$$

Putting $\beta'_{\rm grow} = 100$ and $X_{\rm cold} = 0.5$, we obtain $\tau_{\rm tr}/\tau_{\rm SF} > 1/50$ for the enough dust growth, which realizes the large amplitude of the time variation of the dust-to-gas ratio. This means that the timescale of the phase transition should be larger than several $\times\ 10^7$ yr for the sufficient dust growth, since $\tau_{\rm SF} \sim 3$ Gyr (Kennicutt et al. 1994). Here, we note that the timestep in Figures 3 and 4 is c^{-1} in the physical unit and that $c^{-1} = 3 \times 10^6$–3×10^7 yr. In the longer unit ($c^{-1} = 3 \times 10^7$ yr; corresponding to Figures 3a and 4a), the amplitude of the dust-to-gas-ratio oscillation is large. On the contrary, in the shorter unit ($c^{-1} = 3 \times 10^6$ yr; corresponding to Figures 3b and 4b), the amplitude is much smaller because the timestep is shorter and thus the condition (4.26) is difficult to be satisfied. Moreover, comparing Figures 3a and 4a, we see that the amplitude is larger if the period is longer.

In Figure 4.6, the maximum of the dust-to-gas ratio is larger than the minimum by an order of magnitude. Thus, the dust-to-gas ratio in spiral galaxies can show an order-of-magnitude oscillation. We should note that the parameter range is reasonable for the spiral galaxies (Ikeuchi 1988). Thus, we have confirmed the interpretation of the scatter in the dust-to-gas ratio by Hirashita (2000b), who interpreted the scatter in the dust-to-gas ratio of the nearby spiral sample as the short-term ($\sim 10^7$–10^8-yr) variation of the dust-to-gas ratio with the maximum-to-minimum ratio of more than 4.

4.7.2 Effect of Chemical Evolution

In the discussions above, the metallicity was fixed because the timescale of the phase transition is much shorter than that of the chemical enrichment. However, the time range shown in

Figures 4.3–4.6 (250 timesteps) corresponds to 7.5 Gyr when the $c_*\tau_{\rm SF} = 100$ is adopted. Thus, we need to examine the effect of the chemical evolution here.

To include the effect of chemical evolution, we solve equation (4.18) to examine the time variation of metallicity. If $\tau_{\rm SF}$ is fixed for simplicity, the solution of equation (4.18) becomes

$$X_{\rm O} = \frac{y_{\rm O}\tau}{c_*\tau_{\rm SF}}\,. \tag{4.27}$$

In other words, we simply assume a constant rate of metal enrichment to examine a effect of the chemical evolution qualitatively. We solve basic equations in §2.3 for the time-variable $X_{\rm O}$ described by equation (4.27). As a representative case, we adopt the parameter set identical to Model 4a in Table 4.3, since the oscillation behavior of the dust-to-gas ratio is the most prominent (Figure 4.6). The result is shown in Figure 4.7. We see that the qualitative behavior of the dust-to-gas ratio is the same as the results for constant metallicity, except for the gradual increase of dust-to-gas ratio. This increase is due to the metal production, from which dust is formed.

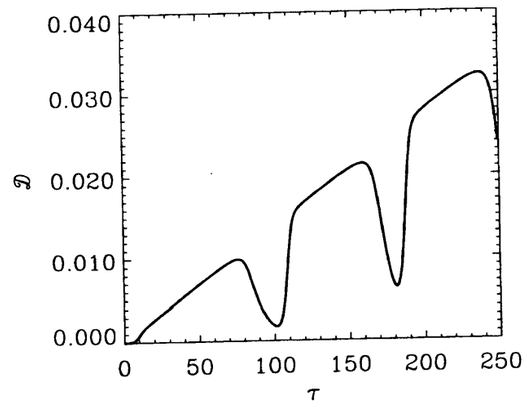

Figure 4.7: Time evolution of the dust-to-gas ratio. The model parameters are same as Model 4a, but the effect of the steady chemical enrichment is included. A constant rate of metal enrichment is assumed.

Thus, two behaviors of the temporal variation is coupled: One is the gradual increase of the dust-to-gas ratio on the timescale of chemical enrichment, and the other is the short-term variation of the dust-to-gas ratio owing to the ISM phase changes.

We also show the relation between the dust-to-gas ratio and oxygen abundance. This is the same type of plot as Figures 3.1*a–c*. The same data is adopted. The scatter of the dust-to-gas ratio for the spiral sample (*squares*) are reproduced with the oscillatory behavior. This implies that the scatter of the dust-to-gas ratio in spiral sample is due to the phase change of gas.

We note that the effect of chemical evolution is of significant importance if $\tau_{\rm SF}$($\sim$ timescale of the chemical enrichment) is short. Especially for starburst galaxies, $\tau_{\rm SF} \sim 10^8$ yr, which is

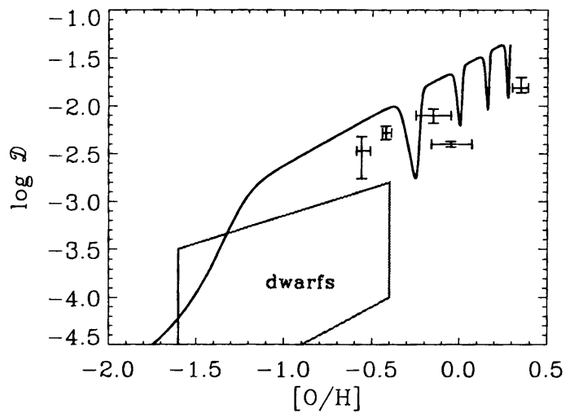

Figure 4.8: Relation between dust-to-gas ratio and oxygen abundance for the same model as Fig. 4.7. The same data as Figs. 3.1*a*–*c* are adopted.

comparable to $\tau_{\rm tr}$. In this case, the metal enrichment also proceeds from the starburst in $\tau_{\rm SF}$, and thus the assumption of the constant metallicity is never satisfied. The same discussion may also be applied to the initial burst in the formation epoch of galaxies, when $\tau_{\rm SF}$ is nearly the value of starburst galaxies ($\sim 10^8$ yr; the dynamical time).

4.7.3 Observational Implications

We have shown that the dust-to-gas ratio varies on a timescale of the ISM phase transition ($\sim 10^7$–10^8 yr) in spiral galaxies. The amplitude of the variation can be an order of magnitude. The result also suggests that the variation is partially responsible for the scatter in the FIR-to-optical flux ratio of spiral sample in Tomita et al. (1996), since the dust content as well as the stellar heating (dust temperature) is responsible for the FIR luminosity (e.g., Whittet 1992, p. 170).

We comment on the dust content in dwarf galaxies. Lisenfeld & Ferrara (1998) modeled the time evolution of the dust amount in star-forming dwarf galaxies (dwarf irregular galaxies and blue compact dwarf galaxies). Based on their model and considering the dust formation in cold clouds (Dwek 1998), Hirashita (1999b) presented that the dust growth in dwarf galaxies is negligible compared with the dust condensation from metal ejected by stars. This is because the metallicity of dwarf galaxies is much smaller than that of spiral galaxies and the collision between grains and metal atoms is not frequent enough for efficient growth of the grains. Thus, the oscillation of dust-to-gas ratio through the variation of the dust growth efficiency is difficult in dwarf galaxies. In this case the scatter of the dust-to-gas ratio of the dwarf sample may be interpreted to reflect the various efficiency of the gas outflow (Lisenfeld & Ferrara 1998). The wind may easily blow out of dwarf galaxies because of their shallow gravitational potentials (Larson 1974; De Young & Heckman 1994), though the distribution of dark matter largely affects the process of the outflow (Mac Low & Ferrara 1999; Ferrara

& Tolstoy 2000).

We should note that the timescale of the phase transition in dwarf galaxies is expected to be longer because of their longer cooling timescale. Since the metal-line cooling is the dominant cooling mechanism for the hot gas (Raymond, Cox, & Smith 1976), the small metallicity of dwarf galaxies, typically $\sim 1/10$ of the spiral galaxies, makes the cooling time longer by an order of magnitude ($> 10^8$ yr). Thus, once the hot component becomes dominant in a dwarf galaxy, the dwarf galaxy must wait for the hot component to cool down for more than 10^8 yr, during which the growth of dust grains is prevented. This as well as the mechanism in the previous paragraph makes the dust growth difficult. Indeed, the dust-to-gas ratios in dwarf galaxies are known to be much smaller than those in spiral galaxies (e.g., Gondhalekar et al. 1986).

Part III

Infrared Emission and Galaxy Evolution

Chapter 5

Infrared Emission and Chemical Evolution

There are many aspects for the galaxy evolution. One of them is the star formation history (SFH).[1] The SFH of a galaxy may reflect its dynamical evolution. This means that a theoretical model for the dynamical evolution may be constrained by the SFH. From observational viewpoint, it is relatively easy to trace the radiation from stars. Thus, revealing the SFH of a galaxy is important both theoretically and observationally.

When we want to know the SFH of a galaxy during its lifetime, its color and metallicity are important diagnostic quantities (e.g., Tinsley 1972). The evolution of the color and the metallicity results from the superposition of the successive star formation during the lifetime of the galaxies. Thus, if we try to reveal the evolution of the galaxies, we always need to estimate star formation rate (SFR) on a galactic-wide scale. There are many methods to estimate SFR of galaxies from observational quantities (Kennicutt 1998a). The present SFR of galaxies is usually traced with the radiation of young massive stars. Since young massive stars emit ionizing photons, the intensity of a hydrogen recombination line is often used to estimate SFR. Kennicutt (1998b) derived a formula to estimate the SFR from the Hα luminosity, $L_{\mathrm{H}\alpha}$, as

$$\frac{\mathrm{SFR}}{1\ M_\odot\ \mathrm{yr}^{-1}} = 3.05 \times 10^{-8} \left(\frac{L_{\mathrm{H}\alpha}}{1\ L_\odot} \right) . \tag{5.1}$$

We also use luminosities of ultraviolet (UV) continuum (Madau, Pozzetti, & Dickinson 1998), nebular lines (e.g., [O II]; Gallagher, Bushouse, & Hunter 1989), and so on for indicators of SFR. Especially, [O II]λ3727 Å is a useful line for $z \lesssim 0.4$, where the Hα emission is out of the optical bands.

In this chapter, we are especially interested in the conversion formula from infrared (IR) emission originating from dust grains to their SFR. Since the absorption cross section of the dust is strongly peaked in the UV, the IR emission from dust can be a sensitive tracer of the young stellar population (chapter 2). Indeed, IR luminosity and Hα luminosity are correlated (Lonsdale Persson & Helou 1987; cf. Savage & Thuan 1992). Kennicutt (1998b) estimated SFR from IR luminosity in an extreme case where the bolometric luminosity is equal to the IR luminosity. This is applicable to starburst galaxies (Soifer et al. 1987). Buat & Xu (1996)

[1] Star formation history is defined as the time evolution of star formation rate. Star formation rate is defined as the gas mass converted into stars per unit time.

adopted an empirical approach by utilizing the observed relation between the UV luminosity and the IR luminosity.

Recently Inoue et al. (2000, hereafter IHK00) derived a theoretical conversion formula from IR luminosity to the SFR by developing a model of dusty H II regions by Petrosian, Silk, & Field (1972). We will examine how metallicity (or dust-to-gas ratio) affects the conversion factor of IHK00. Fortunately, it is possible for us to perform this, since the effects of the metallicity and the dust-to-gas ratio are well parameterized in their formula. Here, we present it as

$$\frac{\mathrm{SFR}}{1\ M_\odot\ \mathrm{yr}^{-1}} = \frac{3.3\times10^{-10}(1-\eta)}{0.4-0.2f+0.6\epsilon}\left(\frac{L_{\mathrm{IR}}}{1\ L_\odot}\right), \tag{5.2}$$

where f is the fraction of ionizing photons absorbed by hydrogen, ϵ is the efficiency of dust absorption for nonionizing photons, L_{IR} is the observed luminosity of dust in the wavelength range of 8–1000 μm, and η is the cirrus fraction of L_{IR}. In equation (5.2), f and ϵ depend on the dust-to-gas ratio.[2] According to Hirashita (1999a, b), moreover, the dust-to-gas ratio is expressed as a function of metallicity (chapter 3). Therefore, the relation between L_{IR} and SFR depends on metallicity via the two parameters, f and ϵ. In this chapter, we examine the importance of the metallicity in our conversion law quantitatively. As a conclusion, that dependence is not always negligible when we compare SFRs of very young galaxies with those of present galaxies. Another approach to the IR luminosity from the chemical evolution model is described in Takagi et al. (1999), which is based on a spectral synthesis model.

5.1 SFR from IR luminosity

First of all, IHK00's formula is explained. Their formula is useful for estimating the SFR of various morphological types of galaxies.

5.1.1 IHK00's Formula

IHK00's formula is derived from the model for the IR luminosity of an H II region. H II region is known to be luminous in IR, which is interpreted as a reprocessed radiation of stellar light. Petrosian et al. (1972) estimated the IR luminosity from dusty H II regions with a simple analytic approximation. The analysis by IHK00 is based on their result. They assumed Case B (Baker & Menzel 1938),[3] where the Lyman-series photons, emitted when an electron jumps down to the ground level ($n=1$), are completely reabsorbed with no reabsorption at longer wavelengths. In this case, each Lyman photon emitted from a level with $n\geq3$ will be converted after reabsorptions and reemissions into photons of lower frequency and a Lyman α (Lyα) photon, which either escapes in the line wings or is absorbed by dust. Assuming Case B, Petrosian et al. (1972) derived the following equation for the IR luminosity,

$$L_{\mathrm{IR}} = L(\mathrm{Ly}\alpha) + (1-f)\langle h\nu\rangle_{\mathrm{ion}}N_{\mathrm{u}} + \epsilon L_{\mathrm{nonion}}\,, \tag{5.3}$$

where $\langle h\nu\rangle_{\mathrm{ion}}$ is the averaged energy of a ionizing photon, and L_{IR}, $L(\mathrm{Ly}\alpha)$, and L_{nonion} are luminosities of IR radiation from dust, Lyα, and nonionizing photons, respectively. They

[2] Although there might be dependence of $(1-\eta)$ on the dust-to-gas ratio, the ambiguity of the dependence is significantly large. We focus our attention on f and ϵ. The cirrus fraction is examined in §5.2.2.

[3] In Case A, all photons in the Lyman series are assumed to escape with no reabsorption.

assumed that all Lyman α (Lyα) photons produced by hydrogen recombination process in an H II region are absorbed by dust within this region and then reemitted as IR radiation (§5.1.5). This is reflected in the first term of the right-hand side in equation (5.3). The second term represents the energy of ionizing photons absorbed directly by dust within the H II region. Then, the last term denotes the energy of nonionizing radiation absorbed by dust in or nearby an ionized region, especially, in clouds surrounding this region.

We now consider the luminosity of the Lyman-α emission line within H II regions. Under Case B approximation, every ionizing photon will eventually form one hydrogen atom with the $n=2$ level. In this process, about two-thirds of recombining electrons will reach the 2p state and go down to 1s, emitting a Lyman-α photon. The remaining one-third of recombining electrons will reach the 2s state, and two continuum photons will be emitted simultaneously within 1 second because the transition from the 2s to the 1s is forbidden for any one photon process (e.g., Spitzer 1978). Thus, $L(\mathrm{Ly}\alpha)$ in terms of S is $0.67h\nu_{\mathrm{Ly}\alpha}fS$, where $\nu_{\mathrm{Ly}\alpha}$ is the frequency at the Lyman-α emission.

The luminosity of ionizing photons from central sources, L_{ion}, is written as $\langle h\nu\rangle_{\mathrm{ion}}S$. When we set $h\nu_{\mathrm{Ly}\alpha}$=10.2 eV and $\langle h\nu\rangle_{\mathrm{ion}}\sim15$ eV, the luminosity of Lyman-α is given by

$$L(\mathrm{Ly}\alpha) = 0.67\frac{h\nu_{\mathrm{Ly}\alpha}}{\langle h\nu\rangle_{\mathrm{ion}}}fL_{\mathrm{ion}} \simeq 0.45fL_{\mathrm{ion}}. \tag{5.4}$$

Therefore, equation (5.3) is reduced to

$$L_{\mathrm{IR}}(8-1000\mu\mathrm{m}) = (1-0.55f)L_{\mathrm{ion}} + \epsilon L_{\mathrm{nonion}}, \tag{5.5}$$

where $\epsilon\equiv1-e^{-\tau}$ is an averaged dust-absorption-efficiency of nonionizing photons from central sources in H II regions.

They further used an analytical fitting formula for the stellar mass–luminosity relation and Salpeter's initial mass function (IMF) with the stellar mass range of 0.1–100 $M_\odot$), deriving the relation between L_{ion} and L_{nonion}. Then, they derived the stellar mass responsible for the luminosity. Dividing the stellar mass with a typical timescale, they finally derived the formula as presented in equation (5.1).

For the IR luminosity, the luminosity in the range sensitive to *IRAS* (40–120 μm) is often used (we denote this luminosity as L_{IRAS}). According to IHK00, the relation between L_{IR} (defined as the luminosity in 8–1000 μm) and L_{IRAS} is $L_{\mathrm{IR}}=1.4L_{\mathrm{IRAS}}$.

Now it will be convenient to define the factor C_{IR} as

$$\mathrm{SFR} = C_{\mathrm{IR}}L_{\mathrm{IR}}\,, \tag{5.6}$$

$$C_{\mathrm{IR}} \equiv \frac{3.3\times10^{-10}(1-\eta)}{0.4-0.2f+0.6\epsilon}\ [M_\odot\ \mathrm{yr}^{-1}\ L_\odot^{-1}]\,. \tag{5.7}$$

IHK00 commented that if the IMF of Scalo (1986) is adopted, C_{IR} becomes 0.8 times as large as the Salpeter case. If 60 $M_\odot$ is adopted for the upper mass cutoff for stars with the Salpeter IMF, C_{IR} becomes 1.4 times larger. Thus, they concluded that the choice of an IMF cause uncertainty of a factor of 2 to C_{IR}.

We focus on the dependence of C_{IR} on metallicity. The dependence of C_{IR} on dust-to-gas ratio is included through f and ϵ as will be described in §§5.1.2 and 5.1.3. We will check our model observationally in §5.1.7. Then, using the relation between the dust-to-gas ratio and the metallicity, we will obtain the metallicity dependence of C_{IR}.

5.1.2 Dependence of f on dust-to-gas ratio

The dependence of f (eq. [5.7]) on dust-to-gas ratio is obtained from Spitzer (1978, hereafter S78). We define $\tau_{\rm S,d}$ and $\tau_{\rm S,H}$ as the optical depths of the dust and of the neutral hydrogen atoms, respectively, for the Lyman-continuum photons over a path length equal to the Strömgren radius $r_{\rm S}$ (see S78 or eq. [5.10] for the definition of $r_{\rm S}$). Since the radius of a dust-free H II region is estimated to be $r_{\rm S}$, it is very useful to normalize the length scale by $r_{\rm S}$. To define a "radius," the H II region should be well described by a spherically symmetric geometry. A number of authors (e.g., Rowan-Robinson 1980) studied the IR properties of samples of H II regions and concluded that they could be modeled adequately by spherically symmetric dust clouds surrounding young massive stars.

First, we calculate $\tau_{\rm S,d}/\tau_{\rm S,H}$ for an H II region. Here, both $\tau_{\rm S,d}$ and $\tau_{\rm S,H}$ are approximated with the optical thickness at the Lyman limit (912 Å). Assuming that the dust-to-gas ratio in the H II region is the same as that in the averaged value in the interstellar space, we obtain

$$\frac{\tau_{\rm S,d}}{\tau_{\rm S,H}} = \frac{\tau_{\rm S,d}}{n_{\rm H} s r_{\rm S}} = 12\,\frac{E_{B-V}}{N_{\rm H} s}\,, \tag{5.8}$$

where the dust extinction at 912 Å, A_{912}, is taken to be $13E_{B-V}$ mag according to the Galactic extinction property (Fig. 2.2), and $\tau_{\rm S,d} = A_{912}/(2.5\log_{10} e)$. Moreover, $n_{\rm H}$ and $s = 6.30\times10^{-18}$ cm^2 denote the number density of the hydrogen and the absorption coefficient for a hydrogen atom in the $n = 1$ level (eq. [5.6] of S78), respectively, and the column density $N_{\rm H}$ is defined as $N_{\rm H} \equiv n_{\rm H} r_{\rm S}$.

If we assume that the physical properties of grains such as extinction curve are unchanged, $E_{B-V}/N_{\rm H}$ is proportional to the dust-to-gas mass ratio $\mathcal{D}$. According to S78, $\mathcal{D} = 6\times10^{-3}$ when $N_{\rm H}/E_{B-V} = 5.9\times10^{21}$ mag^{-1} cm^{-2} (§§7.2 and 7.3 of S78). Thus, equation (5.8) reduces to

$$\frac{\tau_{\rm S,d}}{\tau_{\rm S,H}} = \frac{1}{3100}\left(\frac{\mathcal{D}}{6\times10^{-3}}\right). \tag{5.9}$$

This is the same as equation (5.23) in S78 but the explicit expression of the dependence on $\mathcal{D}$.

Next, we calculate $\tau_{\rm S,H} = n_{\rm H} s r_{\rm S}$. The Strömgren radius is estimated by

$$N_{\rm u} = \frac{4\pi}{3} r_{\rm S}^3 n_{\rm e} n_{\rm p} \alpha^{(2)}\,, \tag{5.10}$$

where $n_{\rm e}$ and $n_{\rm p}$ are the number densities of electrons and protons, and $\alpha^{(2)}$ is the recombination coefficient to the $n = 2$ level. If we assume that the hydrogen is fully ionized, we obtain

$$r_{\rm S} = 1.4\left(\frac{N_{\rm u}}{10^{48}\ {\rm s}^{-1}}\right)^{1/3}\left(\frac{n_{\rm H}}{10^2\ {\rm cm}^{-3}}\right)^{-2/3}\ {\rm pc}\,, \tag{5.11}$$

where $N_{\rm u}$ represents the number of ionizing photons emitted from central stars per second. In this equation, we have assumed that the temperature of the H II region is 8000 K (i.e., $\alpha^{(2)} = 3.09\times10^{-13}$ cm^3 s^{-1}; see eq. [5.14] of S78). Using the estimation of the Strömgren radius above, we obtain

$$\tau_{\rm S,H} = 2.7\times10^3\left(\frac{n_{\rm H}}{10^2\ {\rm cm}^{-3}}\right)^{1/3}\left(\frac{N_{\rm u}}{10^{48}\ {\rm s}^{-1}}\right)^{1/3}, \tag{5.12}$$

Combining this with equation (5.9), $\tau_{\rm S,d}$ is estimated as

$$\tau_{\rm S,d} = 0.87\left(\frac{\mathcal{D}}{6\times10^{-3}}\right)\left(\frac{n_{\rm H}}{10^2\ {\rm cm}^{-3}}\right)^{1/3}\left(\frac{N_{\rm u}}{10^{48}\ {\rm s}^{-1}}\right)^{1/3}. \tag{5.13}$$

We note that $\tau_{\rm S,d}$ becomes large as $N_{\rm u}$ increases. This is because the large $N_{\rm u}$ means the large size of the H II region. As the size of an H II region becomes larger, the probability that the dust grains absorb the photons inside the H II region increases. Thus, we can believe the dependence of $\tau_{\rm S,d}$ on $N_{\rm u}$ in equation (5.13) to be reasonable.

Next, we estimate the fraction of the ionizing photons absorbed by dust grains. Because of the grain absorption, the size of an H II is smaller than $r_{\rm S}$. The radius of the ionizing region, $r_{\rm i}$, is expressed as

$$fN_{\rm u} = \frac{4\pi}{3} r_{\rm i}^3 n_{\rm e} n_{\rm p} \alpha^{(2)}\,, \tag{5.14}$$

where f is the same as that in equation (5.2). If we define $y_{\rm i} \equiv r_{\rm i}/r_{\rm S}$, we obtain from equations (5.10) and (5.14)

$$f = y_{\rm i}^3\,. \tag{5.15}$$

A useful relation between $\tau_{\rm S,d}$ and $y_{\rm i}$ was given in Table 5.4 of S78, where $y_{\rm i}$ is estimated from the following expression (eq. [5.29] of S78):

$$3\int_0^{y_{\rm i}} y^2 e^{y\tau_{\rm S,d}}\,{\rm d}y = 1\,. \tag{5.16}$$

In Figure 5.1*a*, we show f as a function of $\tau_{\rm S,d}$.

We often need a value of f for $\tau_{\rm S,d} \sim 1$. This optical depth corresponds to the "surface" of an H II region observed at the Lyman limit. From Figure 5.1a, we estimate $f \sim 0.5$ at $\tau_{\rm S,d} \sim 1$. If we want to estimate the dust absorption on the scattered surface of the star-forming region, thus, we may use $f \sim 0.5$ as being a reasonable rough estimation.

When we consider the dependence of f on the dust-to-gas ratio, a large ambiguity exists: The number of ionizing photons per H II region is unknown, since the typical number and mass function of OB stars in an H II region is difficult to determine exactly. Fortunately, for the purpose of finding the dependence on $\mathcal{D}$, this is resolved by calibrating the "Galactic" f with the value of Orion Nebula. According to Petrosian et al. 1972, $f = 0.26$ for the Nebula. They also commented that the value explains the IR emission from the H II region. Adopting $f = 0.26$ as the typical value of the Galaxy, we obtain $\tau_{\rm S,d} = 2.7$ for the typical Galactic H II regions (we consider $\mathcal{D} \sim 6\times10^{-3}$ for such regions) from Figure 5.1a. Hence we write

$$\tau_{\rm S,d} = 2.7\left(\frac{\mathcal{D}}{6\times10^{-3}}\right). \tag{5.17}$$

This is consistent with equation (5.13) if we assume $n_{\rm H} = 10^2$ cm^{-3} and $N_{\rm u} \simeq 3.0\times10^{49}$ s^{-1}. Thus, the net effects of mass function and number of OB stars are included in equation (5.17). For readers' convenience, we list the number of ionizing photons from stars with various spectral types in Table 5.1. Our simple treatment is convenient for our motivation to find the dependence of $C_{\rm IR}$ on $\mathcal{D}$. Combining equation (5.17) with equation (5.16), we obtain f as a function of $\mathcal{D}$ as shown in Figure 5.1*b*.

Table 5.1: Number of ionizing photons emitted from OB stars per unit time

Spectral Type	$T_{\rm eff}$ (K)	$N_{\rm u}$ 10^{48} s^{-1}
O5.....	47,000	51
O6.....	42,000	17
O7.....	38,500	7.2
O8.....	36,500	3.9
O9.....	34,500	2.1
B0.....	30,900	0.43
B1.....	22,600	0.0033

NOTE.—Data is from Table 5.3 of Spitzer (1978). $T_{\rm eff}$ is the effective temperature of each star.

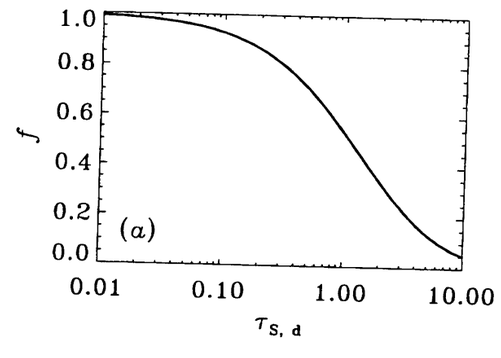

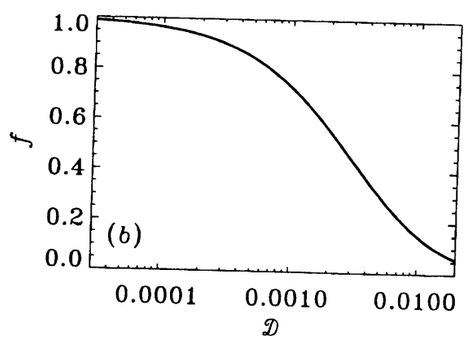

Figure 5.1: (*a*) Fraction of the ionizing photons absorbed by hydrogen, f, as a function of $\tau_{\rm S,d}$ (optical depth of dust for the nonionizing photons over a distance equal to the Strömgren radius). (*b*) Fraction of the ionizing photons absorbed by hydrogen, f, as a function of the dust-to-gas ratio, $\mathcal{D}$.

5.1.3 Dependence of ϵ on dust-to-gas ratio

In IHK00, ϵ (eq. [5.7]) is defined by

$$\epsilon \equiv 1 - e^{-\tau_{\rm nonion}}, \tag{5.18}$$

where $\tau_{\rm nonion}$ is the mean optical depth of dust for nonionizing photons. That is, ϵ represents the efficiency of the dust absorption of nonionizing photons. IHK00 estimated $\epsilon = 0.9$ ($\tau_{\rm nonion} = 2.3$) from the averaged visual extinction of Usui, Saitō, & Tomita (1998)'s sample ($A_V \sim 1$ mag) and the Galactic extinction curve between 1000 Å and 4000 Å by Savage & Mathis (1979). This wavelength range is fit for our purpose, since most of the nonionizing photons from OB stars are emitted in the wavelength well shorter than 4000 Å.

It is obvious that $\tau_{\rm nonion}$ depends on the dust-to-gas ratio. If the column density of gas contributing to the absorption of nonionizing photons is fixed, $\tau_{\rm nonion}$ is proportional to the dust-to-gas ratio. Since we are interested in the dependence of $C_{\rm IR}$ on $\mathcal{D}$, we simply adopt the relation $\tau_{\rm nonion} \propto \mathcal{D}$. Here, we determine the numerical value of $\tau_{\rm nonion}$ as

$$\tau_{\rm nonion} = 2.3 \left(\frac{\mathcal{D}}{6 \times 10^{-3}} \right), \tag{5.19}$$

so that $\tau_{\rm nonion}$ becomes 2.3 for the Galactic dust-to-gas ratio. By combining equations (5.2) and (5.19), we obtain ϵ as a function of $\mathcal{D}$ as shown in Figure 5.2.

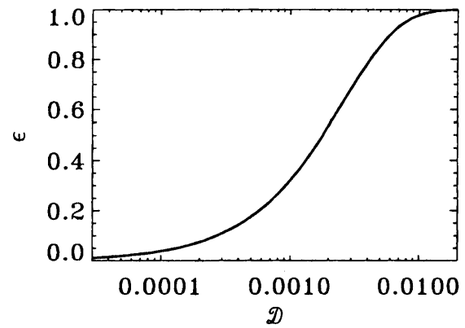

Figure 5.2: Fraction of the nonionizing photons absorbed by dust, ϵ, as a function of the dust-to-gas ratio, $\mathcal{D}$.

5.1.4 Cirrus Fraction

The fraction of the cirrus component, η, remains to be determined. In this chapter, an empirical value of η is simply adopted. According to Lonsdale Persson & Helou (1987), $\eta \sim 0.5$–0.7 for their sample spiral galaxies. We use $\eta = 0.5$ as adopted in IHK00 (the averaged value for Usui et al. 1998's sample) in the current estimate for our SFR or $C_{\rm IR}$. We need to find the variation of the cirrus fraction by the change of $\mathcal{D}$. However, it is very

difficult for us to determine it reasonably. Hence, as only a first step, we adopt a constant η. This means that a universal η for any galaxy is assumed. Unfortunately, this assumption of $\eta = 0.5$ breaks if we are interested in the starburst galaxies. When we examine the sample of starburst galaxies, indeed, it is reasonable to assume $\eta \simeq 0$. This is because young stars dominate the radiation field that heats the dust (Soifer, Houck, & Neugebauer 1987a). Here, we only comment that ambiguity of a factor of ~ 2 on SFR exists owing to the assumption of $\eta = 0.5$. However, we will examine some simple cases for varying η as a function of $\mathcal{D}$ in §5.2.2.

5.1.5 Absorption of Lyman-α photons by dust

Here, we should note the treatment of Lyα photons. Since IHK00's derivation of equation (5.2) is based on Case B, Lyα photons are assumed to be easily trapped in an H II region. Thus, during the resonant scatterings in an H II region, all the Lyα photons are assumed to be absorbed by grains here as in IHK00.

In fact, the Lyα photons escape with the probability of the order of $\sim 1/\tau_{\rm L\alpha}$ (Osterbrock 1989; Emerson 1996), where $\tau_{\rm L\alpha}$ is the optical depth of the Lyα photons. This means that the number of scatter of Lyα photons before the escape is $\sim \tau_{\rm L\alpha}$. According to S78, $\tau_{\rm L\alpha} \sim 10^4$ for a typical H II region. Hence, the dust grains absorb the Lyα photons in an H II region with a high probability.

If the dust-to-gas ratio is significantly smaller than the Galactic value, the dust grains may not efficiently absorb the Lyα photons in H II regions. However, in realistic situations, an H I envelope on a galactic scale generally exists around H II regions. When a Lyα photon escapes from an H II region, it will be absorbed very soon by the neutral hydrogens surrounding the ionized region. This is because efficient resonant scattering is also expected in the H I envelope. Hence, even if there are only small amount of dusts, we can expect a sufficient chance for dusts to absorb the Lyα photons before they escape from the H I envelope. In the considerations hereafter, we assume that $L_{\rm IR}$ include both the components from the H II regions and the H I envelope. We check this point below by assuming that the scattering is a random-walk process of a Lyα photon (Adams 1972).

First of all, we define a path length of the Lyα photons, $l_{\rm path}$. It is estimated as being $l_{\rm path} \sim \tau_{\rm Ly\alpha}^2 l_{\rm Ly\alpha}$ where $\tau_{\rm Ly\alpha}$ means the optical depth for Lyα photons and $l_{\rm Ly\alpha}$ is the mean free path of the Lyα photons. The square to $\tau_{\rm Ly\alpha}$ means that the resonant scattering is assumed to be a random-walk process of photons. Next, we define an optical depth of dust grains for Lyα photons. It is $\tau_{\rm dust} \sim \pi a^2 l_{\rm path} n_{\rm dust}$ where a is a size of the dusts and $n_{\rm dust}$ is a number density of them. Here, we will discuss whether the Lyα photons have a chance to escape from galaxies. We are interested in a star-forming region surrounded by the H I gas envelope. The scale length of the H I envelope, L, may be estimated to be about 100 pc, which corresponds to the thickness of the disk of spiral galaxies. In such case, $\tau_{\rm Ly\alpha}$ is estimated to be about $L/l_{\rm Ly\alpha}$. Then, we find $\tau_{\rm dust} \sim \pi a^2 n_{\rm dust} L^2 / l_{\rm Ly\alpha}$. Using $\mathcal{D}$, it is expressed as

$$\tau_{\rm dust} \sim \frac{\pi a^2 n_{\rm H} \mathcal{D} L^2 m_{\rm p}}{l_{\rm Ly\alpha} m_{\rm dust}}, \tag{5.20}$$

where $m_{\rm p}$ is proton mass and $m_{\rm dust}$ is dust mass for an assumed spherical dust with mass density of 3 g cm^{-3}. Adopting $n_{\rm H} = 0.1$ cm^{-3} for a diffuse H I medium, $a = 0.1$ μm, $\mathcal{D} = 6 \times 10^{-5}$, $L = 100$ pc, and the resonant-scattering cross section of Lyα photons 2×10^{-13} cm^2, we find $\tau_{\rm dust} \sim 5 \times 10^2$. Thus, $\tau_{\rm dust}$ is much larger than unity. This means that most

of the Lyα photons are absorbed even if the dust-to-gas ratio is as small as 0.01 times the Galactic value. As a conclusion, we can safely assume that almost all the Lyα photons cannot escape from the parent star-forming galaxies, although they may escape from the star-forming regions.

5.1.6 Dependence of $C_{\rm IR}$ on dust-to-gas ratio

In the above subsections, we have expressed f and ϵ as functions of the dust-to-gas ratio ($\mathcal{D}$), while η is treated as a constant. We also assume a typical star-forming region whose mean density of gas and production rate of ionizing photons are about 10^2 cm^{-3} and 3.0×10^{49} s^{-1}, respectively. Then, we can express $C_{\rm IR}$ defined in equation (5.7) as a function of the dust-to-gas ratio. In Figure 5.3, we present $C_{\rm IR}$ as a function of $\mathcal{D}$, where we adopt $\eta = 0.5$ (§5.1.4). From this figure, we find that the coefficient of the conversion from IR light to SFR becomes about 4 times smaller for $\mathcal{D} \sim 6 \times 10^{-3}$ (the Galactic value; $C_{\rm IR} = 1.8 \times 10^{-10}$ $M_\odot$ yr^{-1} $L_\odot^{-1}$) than that for $\mathcal{D} \sim 6 \times 10^{-5}$ (0.01 times the Galactic value; $C_{\rm IR} = 7.5 \times 10^{-10}$ $M_\odot$ yr^{-1} $L_\odot^{-1}$).

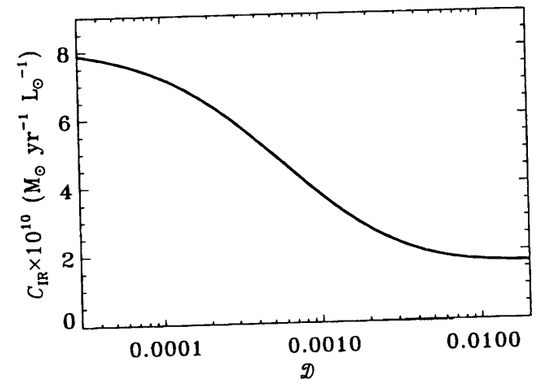

Figure 5.3: $C_{\rm IR}$ (conversion coefficient from the dust luminosity to the star formation rate) as a function of the dust-to-gas ratio, $\mathcal{D}$.

$C_{\rm IR}$ is also changed if we adopt a different extinction curve. In the previous discussions, we have adopted the extinction curve of the Galaxy. The current paragraph examines how the relation between $C_{\rm IR}$ and $\mathcal{D}$ changes when we adopt the extinction curve of the Small Magellanic Cloud (SMC) with the other quantities being adopted in this chapter unchanged. In the SMC-type extinction law, the ratio of the optical depth in equation (5.8) becomes two times larger, because the UV extinction is enhanced in the SMC extinction (for the SMC extinction curve, see Fig. 3.9 of Whittet 1992). This indicates that the same estimation performed in §5.1 is possible if we make the normalization of $\mathcal{D}$ half (i.e., the normalization with 6×10^{-3} is changed to 3×10^{-3}). Thus, we can find a rough dependence of f on $\mathcal{D}$ from Figure 5.1*b* by doubling $\mathcal{D}$ (i.e., the line in Figure 5.1*b* is moved to the left by 0.3 dex). Since $\mathcal{D}$ of SMC is about 5×10^{-4} (Issa et al. 1990), we find $f \simeq 0.75$ for the SMC extinction case, while $f \simeq 0.85$ if we adopt the extinction law of the Galaxy. We can apply the same

scaling to ϵ. For $\mathcal{D} \simeq 5 \times 10^{-4}$, $\epsilon \simeq 0.34$ for the SMC extinction case, while $\epsilon \simeq 0.18$ for the Galactic extinction case. As a result, at $\mathcal{D} \simeq 5 \times 10^{-4}$, $C_{\rm IR} \simeq 3.6 \times 10^{-10}\ M_\odot\ {\rm yr}^{-1}\ L_\odot^{-1}$ for the SMC extinction, while $C_{\rm IR} \simeq 5.0 \times 10^{-10}\ M_\odot\ {\rm yr}^{-1}\ L_\odot^{-1}$ for the Galactic extinction. Thus, we should be aware of the effect of extinction law on our conversion formula, but the effect is small (a factor of 1.4). If we remember that the uncertainty owing to the IMF is a factor of 2 (e.g., IHK00), we find that the dependence of $C_{\rm IR}$ on the the extinction curve is not very important. We note that we can estimate $C_{\rm IR}$ for the SMC-type extinction by moving the line in Fig. 5.3 to the left by 0.3 dex (a factor of 2).

5.1.7 Observational check

Here, we examine whether the values of f and ϵ that we adopted for the Galactic value (i.e., $f = 0.26$ and $\epsilon = 0.9$) is consistent with the properties of H II regions. We examine the ratio between the ionizing-photon luminosity and the IR luminosity. This ratio was extensively examined in 1970s (e.g., Harper & Low 1971).

We start with equation (5.3). By adopting Salpeter's IMF and a mass–luminosity relation of stars, IHK00 derived $L_{\rm nonion} = 1.5\langle h\nu\rangle_{\rm ion} N_{\rm u}$. Then, according to Mezger (1978), we define the IR excess (IRE) as

$$\mathrm{IRE} \equiv \frac{L_{\rm IR}}{h\nu_{{\rm Ly}\alpha} f N_{\rm u}} = a + (1 - f + 1.5\epsilon)\,\frac{\langle h\nu\rangle_{\rm ion}}{h\nu_{{\rm Ly}\alpha} f}, \tag{5.21}$$

where $\nu_{{\rm Ly}\alpha}$ is the frequency of the Lyα radiation, and a is the Lyα photons that reach the 2p state and go down to 1s (i.e., $L({\rm Ly}\alpha) = a h\nu_{{\rm Ly}\alpha} f N_{\rm u}$).[4] According to S78, $a \simeq 0.67$. In Figure 5.4, we express the IRE as a function of the dust-to-gas ratio $\mathcal{D}$.

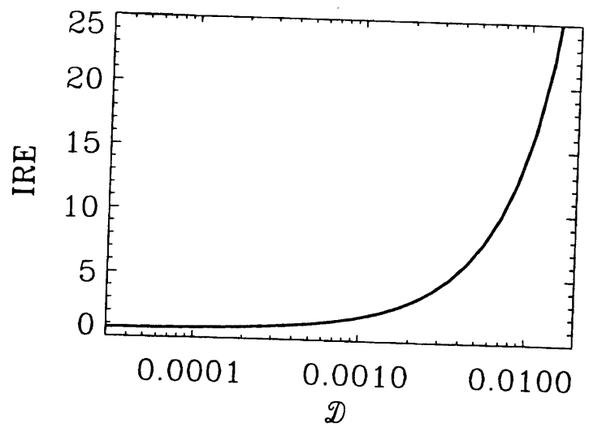

Figure 5.4: IRE (infrared excess) as a function of the dust-to-gas ratio, $\mathcal{D}$.

[4]The other photons decay to the ground state with a two-photon process.

Adopting $f = 0.26$ and $\epsilon = 0.9$ for the Galactic values (§§5.1.2 and 5.1.3), we obtain IRE = 11, where we have assumed that $\langle h\nu\rangle_{\rm ion}$ is equal to $h\nu$ at the Lyman limit (912 Å). According to Harper & Low 1971), $5 \lesssim$ IRE $\lesssim 10$ (see also Aannestad 1978; Mezger 1978; Maihara et al. 1981) for Galactic H II regions. Figure 7.3 in S78 showed that the IR luminosity of H II region is larger than predicted from Lyα luminosity by an order of magnitude (i.e., IRE ~ 10). Thus, f and ϵ that we adopt in this chapter is consistent with the properties of the Galactic H II regions within the scatter of observed IRE.

Another test of our model is possible if we use the data of H II regions in the Large Magellanic Cloud (LMC; DeGioia-Eastwood 1992). Table 3 of DeGioia-Eastwood (1992) indicates systematically lower IREs for the LMC H II regions (IRE = 1–4; the median is 1.6) than for the Galactic ones. If the dust-to-gas ratio of 1/5 times the Galactic value is adopted (e.g., Issa, MacLaren, & Wolfendale 1990), $f \simeq 0.7$ and $\epsilon \simeq 0.2$. Then we obtain IRE $\simeq 3$ for the LMC. Although this lies in the range of the observed IRE, it is larger than the median (1.6) by a factor of two. This may be due to the dust destruction by the intense stellar radiation field in the LMC. In this case, the dust-to-gas ratio may be systematically smaller in H II regions than the averaged value over the whole interstellar medium (ISM). The extinction curve may also change according to environment (metallicity, stellar radiation field, etc.). However, as stated in Misselt, Clayton, & Gordon (1999), the relation between dust properties and environment is complicated.

Anyway, our formulation predicts the IRE of H II regions not only in the Galaxy but also in the LMC correctly within a factor of two. Thus, we consider equation (5.17) and (5.19) to be reasonable in spite of simplification in their derivation. Therefore, we discuss the metallicity dependence of $C_{\rm IR}$ and its effect on the cosmic SFH by using the relation between $C_{\rm IR}$ and $\mathcal{D}$ as shown in Figure 5.3 in the following sections. We note that $C_{\rm IR}$ as a function of $\mathcal{D}$ will give us an insight into the variation of $C_{\rm IR}$ owing to chemical evolution.

5.2 Effect of Chemical Evolution

5.2.1 Metallicity Dependence of the Conversion Formula

In order to obtain the metallicity dependence of the conversion formula (eq. 5.2), which depends on the dust-to-gas ratio as shown in the previous section, we must relate $\mathcal{D}$ and metallicity. Here, we adopt the relation between them in chapter 3, where we constructed a new evolution model of the dust amount in the galactic environment, insisting an importance that the dusts can grow via the accretion of the metal elements in the cool and neutral components of ISM. Then, the relation between $\mathcal{D}$ and metallicity explains whole the observational relation for both the giant and dwarf galaxies. Here, we adopt the solid line in Figure 3.1*a* as the relation between the dust-to-gas ratio and the metallicity, since the line seems to reproduce the relation over the large metallicity range.

Once we accept the relation of the solid line in Figure 3.1*a*, we relate $C_{\rm IR}$ and [O/H] by using the relation between the dust-to-gas ratio and $C_{\rm IR}$ (Fig. 5.3). Here, we note that [O/H] $= x$ means that the abundance of oxygen is 10^x times the solar value. The relation between $C_{\rm IR}$ and [O/H] is presented in Figure 5.5. We see that if [O/H] in the ISM evolves from -2 to 0 via the chemical evolution, the coefficient of the conversion from IR light to SFR becomes about 4 times smaller. Thus, when we would like to determine the SFR precisely within a factor of 4, we should not neglect the effect of metallicity.

Let us recall that $\eta = 0.5$ is assumed. A galaxy is expected to experience a starburst

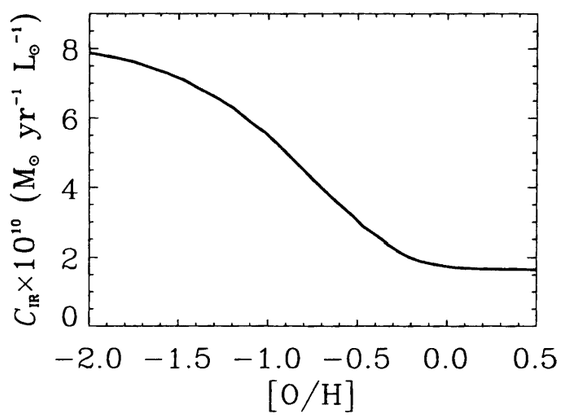

Figure 5.5: C_{IR} (conversion coefficient from the dust luminosity to the star formation rate) as a function of the oxygen abundance, [O/H].

phase at the beginning of its evolution. In a starburst galaxy, $\eta = 0.0$ may be reasonable. Especially in the beginning of the galaxy evolution, we can expect a starburst phase. Thus, the conversion factor of C_{IR} can be estimated as 1.7×10^{-9} at the initial starburst era of galaxies ($f = 1$ and $\epsilon = 0$ are assumed, since we treat the initial phase, when the metallicity is almost 0). Since C_{IR} with $\eta = 0.5$ is accepted for the moderate phase of star formation as normal disk galaxies at the present epoch, the increment of C_{IR} for starburst galaxies with low metallicity is about ten. Thus, we should never forget the ambiguity via the assumption of a constant η. For this point to be resolved, we should model the dependence of $(1 - \eta)$ on $\mathcal{D}$. In our current knowledge, unfortunately, it seems difficult to construct a physically reasonable model. However, we try to examine the change of η as a function of $\mathcal{D}$ in the next subsection.

5.2.2 Dependence of Cirrus Fraction on Metallicity

In the above, we have assumed that the cirrus fraction of the IR luminosity, η, is 0.5. Here, we examine how C_{IR} is affected owing to the change of η. There is a large uncertainty about observational estimate of η. But, theoretically, we consider some simple cases where the change in η cannot be neglected in our conversion formula.

The assumption of $\eta = 0.5$ breaks if we are interested in starburst galaxies. When we examine a sample of starburst galaxies, indeed, it is reasonable to assume $\eta \simeq 0$. This is because young stars dominate the radiation field that heats the dust, and the optical depth of dust is so large that almost all of the bolometric luminosity is emitted in the IR (Soifer et al. 1987a; Kennicutt 1998b). For the starburst galaxies, thus, the dependence of C_{IR} on the metallicity is obtained by putting $\eta = 0$ into equation (5.7), while the dependence of f and ϵ on the metallicity is the same as described in §5.2. The result is shown in Figure 5.6. We see that C_{IR} in this figure is larger by a factor of 2 than that in Figure 5.5.

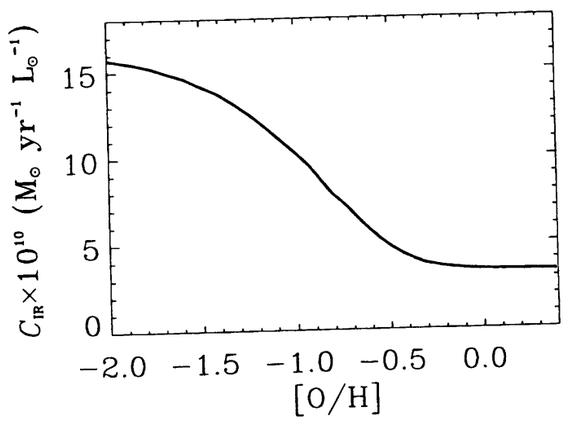

Figure 5.6: C_{IR} (conversion coefficient from the IR dust luminosity to the star formation rate) as a function of the oxygen abundance, [O/H], for starburst galaxies. The cirrus fraction η is assumed to be 0.

Next, we consider a possible change in η of spiral galaxies as a function of metallicity. The cirrus fraction of spiral galaxies is not negligible at the present epoch ($\eta \simeq 0.5$ for nearby spiral galaxies; Lonsdale Persson & Helou 1987). In the beginning of a spiral galaxy's evolution, when only a little metal is produced, $\eta = 0.0$ may be reasonable. Thus, the first approximation for the dependence of η on the dust-to-gas ratio is

$$\eta = 0.5 \left(\frac{\mathcal{D}}{6 \times 10^{-3}} \right) . \tag{5.22}$$

If we adopt this relation, we obtain Figure 5.7 as the relation between C_{IR} and metallicity. We note that our simple treatment as equation (5.22) is only applicable for [O/H] $\lesssim 0$, because $\eta > 1$ does not make sense. This means that we need a nonlinear modeling of the relation between η and $\mathcal{D}$ near the solar metallicity. We may need to consider a complex mode of evolution of ISM, whose nonlinearity causes intermittent SFH (chapter 4; Kamaya & Takeuchi 1997; Hirashita 2000b; Hirashita & Kamaya 2000; Takeuchi & Hirashita 2000). One of the important quantities may be the volume filling factor of H II regions. Comparing C_{IR} at [O/H] ~ -2 with that at [O/H] ~ 0, we see that C_{IR} changes by an order of magnitude as the chemical enrichment proceeds. Thus, if we want to know the realistic cosmic evolution of galaxies from L_{IR}, the metallicity evolution of cirrus must also be examined.

5.2.3 Prospect to Synthetic Stellar Population Models

Spectrophotometric evolution of galaxies is usually modeled by using a population synthesis of stars (e.g., Arimoto & Yoshii 1986; Kodama & Arimoto 1997), which is based on stellar evolutionary track. The spectral synthesis technique, for the starlight alone, consists in summing up the spectra of each stellar generation, provided by the single stellar population

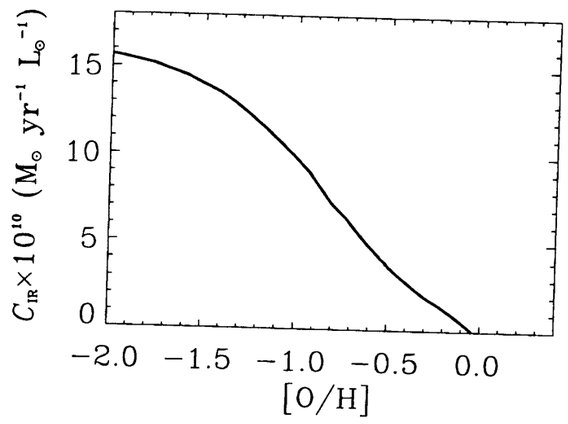

Figure 5.7: C_{IR} (conversion coefficient from the IR dust luminosity to the star formation rate) as a function of the oxygen abundance, [O/H], for spiral galaxies. The cirrus fraction η is assumed to be proportional to the dust-to-gas ratio.

(SSP) of the appropriate age and metallicity, weighted by the SFR at the time of stars' birth. IMF should be also determined to assume the stellar mass distribution in an SSP. If we express the spectrum of an SSP whose age is t as $f_\lambda(t)$, we obtain a synthetic spectrum $F_\lambda(t)$ from the following equation:

$$F_\lambda(t) = \int_0^t \psi(t-\tau)\, f_\lambda(\tau)\, \mathrm{d}\tau\,, \tag{5.23}$$

where $\psi(t)$ is the SFR at t. Such a model is often useful in estimating the age of a stellar system from its color or spectrum (e.g., Tinsley 1980; Guiderdoni & Rocca-Volmerange 1987; Bruzual & Charlot 1993; Leitherer & Heckman 1995). The uncertainty in a synthetic model is caused by the dearth of reliable spectral libraries for cool and non-solar composition stars and by the uncertain properties of post-main-sequence stars (Charlot, Worthey, & Bressan 1996).

Several groups have extended the spectral synthesis modeling to far-IR (FIR) wavelength by including the reprocessing of stellar light by dust grains (Mazzei, Xu, & De Zotti 1992; Silva et al. 1998; Takagi, Arimoto, & Vansevičius 1999; Efstathiou, Rowan-Robinson, & Siebenmorgen 2000; Popescu et al. 2000). The discussions in this chapter may be examined for more realistic but complicated situations by using such synthesis models.

5.3 Comments on the Cosmic Star Formation History

One of the observational test for scenarios of structure formation in the universe is to determine the cosmic SFH. The cosmological evolution of SFR is derived from the comoving density of galactic light (Lilly et al. 1996). For example, Madau et al. (1996) applied the

Table 5.2: Metallicity and C_{IR} as functions of z

z	$\log(Z/Z_\odot)$	C_{IR} $[M_\odot\ \mathrm{yr}^{-1}\ L_\odot^{-1}]$
0.0	0.00	1.7×10^{-10}
0.5	−0.22	1.8×10^{-10}
1.0	−0.48	2.4×10^{-10}
2.0	−1.02	5.2×10^{-10}
3.0	−1.50	7.1×10^{-10}
4.0	−1.79	7.6×10^{-10}
5.0	−1.88	7.8×10^{-10}

conversion formula from UV light to the SFR and showed that the SFR as a function of the redshift z seems to have a peak at $z \sim 1$–2. The cosmic SFR as a function of z has been revised and discussed in many papers (e.g., Steidel et al. 1999), and frequently called the Madau plot at the moment.

The cosmic SFR at $z \sim 3$ has been investigated extensively. Meurer, Heckman, & Calzetti (1999) estimated the UV luminosity density at $z \sim 3$, correcting for the dust absorption. On the other hand, the cosmic SFR at $z \sim 3$ is also determined from the dust-emission at the sub-millimeter (sub-mm) observational wavelength (Hughes et al. 1998; Barger et al. 1998). The observations of the dust emission has an importance that the absorbed light by the dust grains in the UV–visible range is "recovered" in the longer wavelength range. We can convert the sub-mm light to the SFR by applying the formula proposed in IHK00. If we take into account the chemical evolution of galaxies on a cosmological timescale (Pei & Fall 1995; Calzetti & Heckman 1999; Pei, Fall, & Hauser 1999), however, we must examine the dependence of the conversion formula on metallicity as seen in the previous sections. We note that this increment is introduced via f and ϵ mainly.

According to such a motivation, we apply the results obtained in the previous sections, especially Figure 5.5 and its related discussions, to the cosmic SFH. We focus on the evolution of C_{IR} along the metal enrichment history. As known very well, the conversion from metallicity to z is not uniquely determined. As a first step, however, we consider the evolution of our conversion law along the metal enrichment with the aid of previous researches that determined the metallicity as a function of z. We adopt Pei et al. (1999) as a recent modeling of the cosmic chemical evolution.

Pei et al. (1999) modeled the cosmic SFH and chemical evolution and calculated the evolution of dust amount. Considering the absorption and reprocessing of light by dust, they determined the cosmic chemical evolution after the calibration with the Madau plot derived mainly from the UV luminosity. The resultant metallicity evolution as a function of z is shown in the second column of Table 5.2. Though their treatment of the evolution of the dust-to-gas ratio is not just the same as our treatment, for readers' qualitative understanding, we present a relation between the metallicity and the redshift z from their Figure 8. The consistent model, as stated in the previous paragraph, is needed if we translate exactly the evolution of C_{IR} along the metallicity to that along z. Admitting that difficulty, however, we can stress that our results are useful to find the evolution of C_{IR} along the metallicity.

We also present C_{IR} in third column of Table 5.2 calculated from the relation between

metallicity and $C_{\rm IR}$ as shown in Figure 5.5. Here we assume that $\log(Z/Z_\odot) = [{\rm O/H}]$. From Table 5.2, we see that the factor $C_{\rm IR}$ is about 4 times larger at $z \sim 3$ than that at $z \sim 0$. Thus, we should take care of the chemical evolution of the galaxies if we determine the cosmic SFH from the dust emission within a factor of 4. Deriving the cosmic SFH from IR–sub-mm observation will be made possible by the future observational projects (e.g., Appendix of Takeuchi et al. 1999). Our formulation in this chapter will be useful in the conversion from the comoving luminosity density in the IR–sub-mm range to the comoving density of the SFR, resolving the metallicity evolution of the SFR conversion law.

Finally, we should mention that Pei et al. (1999)'s model treats averaged quantities for each redshift and focuses only on the redshift dependence. Thus, our Table 5.2 must be applied to the data averaged for each z. In other words, we should not apply them to each individual galaxy at a certain z. Indeed, there is strong dependency of metallicity on local density according to the numerical simulation by Cen & Ostriker (1999). For each galaxy, Figure 5.5 should be used instead after their metallicity is known.

As a future work, it would be interesting to investigate the earliest evolutionary stage of galaxies. As shown in Nishi & Tashiro (2000), star formation activities in galaxies whose metallicity is less than 1/100 times the solar value are strongly regulated owing to the lack of coolant (see Tamura, Hirashita, & Takeuchi 2001 for an observational discussion). Thus, IR emission from galaxies with extremely low metallicity should be discussed by including the regulation effect.

5.4 Summary of this Chapter

Based on IHK00's formulation, we consider the factor $C_{\rm IR}$ in the conversion formula between the IR luminosity and the SFR, each of which is defined in equations (5.6) and (5.7). The factor $C_{\rm IR}$ becomes 1.7×10^{-10}, 5.2×10^{-10}, and 7.9×10^{-10} $M_\odot$ yr^{-1} $L_\odot^{-1}$ for the metallicity of 1, 0.1, 0.01 times the solar value, respectively. Thus, $C_{\rm IR}$ differs by a factor of 4 in the range. Importantly, applicability of our formula is observationally confirmed by IREs of the Galaxy and the LMC. Applying our result to the cosmic SFH, we have found that the the factor $C_{\rm IR}$ may be about 4 times larger at $z \sim 3$ than that at $z \sim 0$. Thus, we should take care of the chemical evolution of galaxies if we determine the cosmic SFH from the dust emission within a factor of 4.

Chapter 6

Galaxy Number Count in Far Infrared

6.1 Present Status of Far-Infrared Number Count

There have been a number of advances in understanding galaxy evolution over the last several years by optical redshift surveys of galaxies (e.g., Lilly et al. 1995). These surveys have been revealing the star-formation history (SFH) of the universe up to $z \sim 1$. The star-formation rate around $z = 1$ is found to be several times larger than that at $z = 0$. The Lyman-break technique also provides the star-formation properties of galaxies at around $z = 3$ based on the rest ultraviolet (UV) light (e.g., Steidel et al. 1996), and the star-formation rate in the universe seems to have a peak at $z \sim 1$–2 (Madau et al. 1996; but see Steidel et al. 1999). However, optical and UV light may severely suffer from extinction by dust.

The far infrared (FIR) is an important wavelength to trace the SFH of the universe, because the energy absorbed by dust at UV and optical regions is re-emitted in FIR and extinction in FIR is very small. Furthermore, for starburst galaxies, the bulk of the energy is released in FIR; the survey by the Infrared Astronomical Satellite (*IRAS*) discovered hundreds of galaxies emitting well over 95% of their total luminosity in the infrared (IR; e.g., Soifer, Houck, & Neugebauer 1987). Thus, surveys only in UV and optical wavelengths are not sufficient to clarify the SFH of the universe. We also need to investigate the SFH in the FIR bands. Indeed, the recent detection of the cosmic infrared background radiation by *COBE* appears to have comparable brightness to the total intensity in deep optical counts (Fixen et al. 1998; Hauser et al. 1998), which indicates that the infrared region is responsible for roughly half of the energy released by nucleosynthesis in stars.

In the FIR wavelengths, galaxy evolution is discussed based on the number count of the *IRAS* all-sky survey with a flux limit of ~ 1 Jy at 60 μm. Hacking, Condon, & Houck (1987) and Saunders et al. (1990) showed that the observed counts of faint 60-μm sources are about twice as high as the non-evolutionary model prediction, suggesting the presence of source evolution. However, since the depth of the *IRAS* survey is only $z \sim 0.1$ in median (Sanders & Mirabel 1996), a deeper survey is indispensable to explore the higher redshift universe. A survey much deeper than the *IRAS* survey was performed with ISOPHOT aboard the Infrared Space Observatory (*ISO*; Kessler et al. 1996) at the Lockman Hole with a flux limit of 45 mJy at 175 μm (Kawara et al. 1998). According to Kawara et al. (1998), the surface density of sources brighter than 150 mJy at 175 μm agrees with the model by Guiderdoni et al. (1997),

who took into account the burst of star formation whose timescale of gas consumption (~ 1 Gyr) is ten times smaller than that observed in normal disk galaxies (Kennicutt, Tamblyn, & Congdon 1994). Matsuhara et al. (2000) investigated the FIR brightness fluctuations at 90 μm and 175 μm in the Lockman Hole by using the same data as Kawara et al. (1998). They gave constraints on the galaxy number count down to 35 mJy at 90 μm and 60 mJy at 170 μm, which indicate a stronger evolution than that predicted by Guiderdoni et al. (1997). Puget et al. (1999) published source counts based on 175-μm ISOPHOT observations of Marano field covering ~ 0.25 square degrees. Based on estimate by Takeuchi et al. (2001a), a much wider coverage is clearly necessary in the next step to reduce the effect of galaxy clustering (i.e., cosmic variance). Thus, wide surveys as will be conducted by ASTRO-F, the next-generation Japanese IR satellite, is indispensable.[1]

The source counts at 90 and 175 μm are much higher than predicted by no-evolution model (e.g., Takeuchi et al. 2000). According to Takeuchi et al. (2000), the number count as well as the cosmic IR background are explained if the galaxy luminosity strongly evolves from $z = 0$ to $z = 1$ by a factor of 10–100.

ASTRO-F will be launched in 2004. The Far-Infrared Surveyor (FIS) as well as the (near- and mid-) Infrared Camera (IRC) is planned to be on-board. A point source survey in the whole sky will be carried out by the FIS with a depth of 15–50 mJy at 50–200 μm by using unstressed and stressed Ge:Ga 2-D array detectors (Kawada et al. 1998).[2] Since the sensitivity of the FIS (Table 6.1) is 10–100 times higher than that of *IRAS*, the ASTRO-F survey is expected to detect an enormous number of galaxies ($\sim$ several $\times 10^6$ in the whole sky; Takeuchi et al. 1999, hereafter T99). This survey will contribute to studying the SFH and detecting primeval galaxies at high redshift (T99). The survey, however, will not be able to determine the precise redshift (distance) of the detected objects. The rough redshift may be estimated from the multi-wavelength data in the FIR–millimeter range (Takeuchi et al. 2001a).

In order to obtain the precise redshift and to know the natures of the detected sources (e.g., Galactic objects, star-forming galaxies, or AGNs), optical or near-IR (NIR) follow-up observations is necessary. Follow-ups will enable us to obtain a systematic and homogeneous large database that will be more useful for studying the evolution of star-forming galaxies and AGNs as well as the properties of large-scale structures. In the optical and NIR wavelengths, the Subaru telescope is available when the ASTRO-F survey starts. Hence, the instrumental conditions for the follow-up will be excellent and the follow-up of the ASTRO-F survey will be a timely project.

In this chapter, we review the number count model by T99 and Hirashita et al. (1999) in order to see necessary tools for prediction of number count. We concentrate on the ASTRO-F survey and its optical follow-up. Throughout this chapter we adopt a Hubble constant of $H_0 = 75$ km s^{-1} Mpc^{-1} and a deceleration parameter of $\Omega_0 = 0.2$ and the cosmological constant $\Lambda = 0$, unless otherwise stated.

[1]The European Large Area *ISO* Survey (ELAIS) covers 12 square degrees at 6.7, 15, 90, and 175 μm (Oliver et al. 2000).

[2]The FIS also has spectroscopic capability by a Fourier spectrometer covering 50–200 cm^{-1} with spectral resolution of 0.2 cm^{-1}. The same detector arrays for the all-sky survey are used, and these two functions are switched.

Table 6.1: Flux limits of the ASTRO-F far-infrared scanner

Wavelength [μm]	5σ-detection limit [mJy]
50	20
70	15
120	30
150	50

6.2 Model of Far-Infrared Number Count

Models of the source counts generally fall into two groups. The first fall includes those that are tied closely to observations but make no attempt to incorporate a detailed physical model for how galaxies evolve. For example, T99 based their model on the local FIR luminosity function observationally derived from the *IRAS* observations and on the spectral energy distributions (SEDs) of galaxies based on observed spectra of dust emission in the mid-IR–submillimeter (sub-mm) waveband. Instead of making attempt to incorporate our limited understanding of how galaxies evolve, they just assumed simple functional forms for the evolution and investigated how the counts changed as the parameters of these functions were changed. The other category includes the models that incorporate detailed physical models for the way in which galaxies evolve (Wang 1991; Franceschini et al. 1994; Guiderdoni et al. 1998). In this section we review the model used by T99 (in the former category) to calculate the expected number count of the ASTRO-F survey in FIR bands in order to see what information a FIR number count contains.

6.2.1 Spectral Energy Distribution

The assumed SEDs in T99 consist of two components, cool cirrus and hot starbursts, following Rowan-Robinson & Crawford (1989). The cirrus component represents the dust heated mainly by late-type stars, while the starburst component stands for emission from dust heated by hot early-type stars associated with intense starbursts (e.g., Sanders & Mirabel 1996). The model spectrum of the cirrus component is taken from the Galactic interstellar dust model by Désert, Boulanger, & Puget (1990). In T99, it was assumed that galaxies with $L_{\rm IR} < 10^{10}\ L_\odot$ have only the cirrus component, where $L_{\rm IR}$ is defined as the IR luminosity integrated in the wavelength range from 3 μm to 1 mm. Galaxies with larger $L_{\rm IR}$ have both the cirrus and starburst components; an IR luminosity in excess of $10^{10}\ L_\odot$ is assumed to come from the starburst component. The spectrum of the starburst component $L_{{\rm s}\nu}$ is composed of two-temperature modified blackbody radiation, $L_{{\rm s}\nu} = \alpha\nu B_\nu(T_{\rm cool}) + \beta\nu B_\nu(T_{\rm hot})$, where $B_\nu(T)$ is the Planck function with temperature T; both α and β are normalizing constants. Here, the temperatures of the two components are given by $T_{\rm cool} = 60(L_{\rm s}/10^{11}\ L_\odot)^{0.1}$ K and $T_{\rm hot} = 175(L_{\rm s}/10^{11}\ L_\odot)^{0.1}$ K, where $L_{\rm s}$ is the luminosity of the starburst component integrated over the range from 3 μm to 1 mm (Beichman & Helou 1991). The normalizing constants α and β are determined so that 70% of the starburst component comes from the cool component and 30% from the hot component (Beichman & Helou 1991). The model SED is scaled properly to yield the given $L_{\rm IR}$. The resulting SEDs are presented in Figure

6.1.

In the model, AGNs are not considered, since the number of AGNs is expected to be negligible compared with the number of normal and starburst galaxies (Beichman & Helou 1991). Even if the evolution of AGNs is considered, this will also be the case (Pearson 1996).

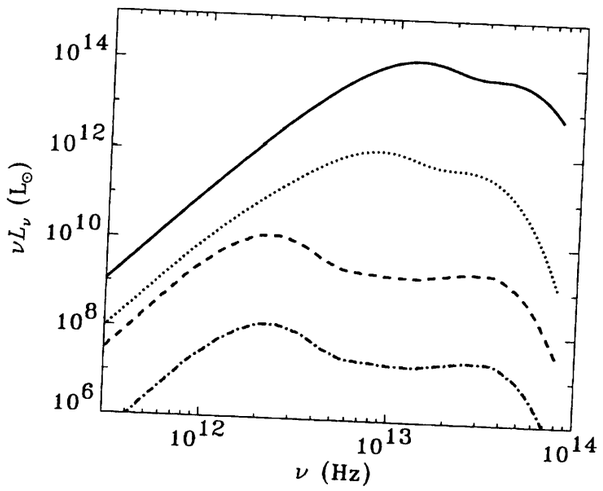

Figure 6.1: Spectral energy distributions (SEDs) assumed in Takeuchi et al. (1999). The solid, dotted, dashed, dot-dashed lines represent the SEDs for $L_{\rm IR} = 10^{14}\ L_\odot$, $10^{12}\ L_\odot$, $10^{10}\ L_\odot$, $10^{8}\ L_\odot$, respectively.

6.2.2 Local Luminosity Function

The local FIR luminosity function of galaxies is derived from the *IRAS* data (Soifer et al. 1987b). Since Soifer et al. (1987b) used the FIR luminosity at 60 μm, T99 converted it into their $L_{\rm IR}$ by using their model SEDs (Fig. 6.1). An analytical fitting to the data leads to the following double-power-law form of the luminosity function:

$$\log[\phi_0(L_{\rm IR})] = \begin{cases} 7.9 - 1.0\log(L_{\rm IR}/L_\odot) & \text{for } 10^8\ L_\odot < L_{\rm IR} < 10^{10.3}\ L_\odot; \\ 17.1 - 1.9\log(L_{\rm IR}/L_\odot) & \text{for } 10^{10.3} L_\odot < L_{\rm IR} < 10^{14}\ L_\odot; \\ \text{no galaxies} & \text{otherwise,} \end{cases} \tag{6.1}$$

where ϕ_0 is the number density of galaxies in $\mathrm{Mpc}^{-3}\ \mathrm{dex}^{-1}$ at $z = 0$. We note that Saunders et al. (1990) suggested another functional form for the IR luminosity function, which behaves as a log-normal distribution for the luminous end and as a power-law form for the faint end.

6.2.3 Survey Limit

ASTRO-F is a survey-type IR telescope in space. Its major goal is to achieve a whole-sky survey in the FIR wavelength region with an order-of-magnitude higher sensitivity and higher

angular resolution as well as with a longer wavelength photometric band than those of the *IRAS* survey (Kawada 1998).

The flux limit of the all-sky ASTRO-F survey is estimated by Kawada (1998) to be 20 mJy at $\sim 50\ \mu$m, 15 mJy at $\sim 70\ \mu$m, 30 mJy at $\sim 120\ \mu$m, and 50 mJy at $\sim 150\ \mu$m (Table 6.1; for recent information, see Takahashi et al. 2000). In the shorter wavelength region of 50–110 μm, the sensitivity is limited by both the internal and background noise, while in the longer wavelength range of 110–170 μm the detection limit is constrained by confusion effects of the interstellar cirrus in the Galaxy. Much better point-source detection limits can be expected in a limited sky areas near to the ecliptic poles, where the survey scan will be repeated more than a hundred times. In this chapter we adopt a conventional value of the point-source detection limit expected for the all-sky survey.

6.2.4 Redshift Distribution of ASTRO-F Galaxies

Assuming the above SED and luminosity function of galaxies, T99 calculated the redshift distribution of ASTRO-F galaxies which were regarded as point sources there. The redshift distribution per unit solid angle and unit redshift is formulated as

$$\frac{\mathrm{d}^2N}{\mathrm{d}\Omega\,\mathrm{d}z} = \frac{\mathrm{d}^2V}{\mathrm{d}\Omega\,\mathrm{d}z}\int_{L_{\rm lim}(z)}^{\infty} \phi(L'_{\rm IR}, z)\,\mathrm{d}\log L'_{\rm IR}, \tag{6.2}$$

where the effect of evolution is included in the luminosity function at z, $\phi(L'_{\rm IR}, z)$, and the comoving volume element per str and per z is denoted as $\mathrm{d}^2V/\mathrm{d}\Omega\mathrm{d}z$ (Ω is the solid angle). In equation (6.2), $L_{\rm lim}(z)$ is the limiting luminosity for the source at z. The limiting luminosity is determined by the detection limit (§6.2.3). The limit as a function of z is listed in Table 6.2 for the 120-μm survey. $L_{\rm lim}(z)$ becomes $10^{14}\ L_\odot$ at $z \sim 5$ so that no galaxies are detected in $z > 5$ due to upper luminosity cutoff of the luminosity function (eq. [6.1]). The comoving volume element can be expressed in terms of cosmological parameters as

$$\frac{\mathrm{d}^2V}{\mathrm{d}\Omega\mathrm{d}z} = \frac{c}{H_0}\frac{d_{\rm L}^2}{(1+z)^3\sqrt{1+2q_0z}}, \tag{6.3}$$

where c is the speed of light and $d_{\rm L}$ is the luminosity distance:

$$d_{\rm L} = \frac{c}{H_0 q_0^2}[zq_0 + (q_0 - 1)(\sqrt{2q_0z+1} - 1)]\,. \tag{6.4}$$

The resultant number count per z in the whole sky is shown in Figure 6.2 for 50-, 70-, 120-, and 150-μm surveys in the case of no evolution. The total number count of the ASTRO-F galaxies integrated over all the redshift range is several times 10^6 in the whole sky at each wavelength. The 120-μm survey is the deepest ($z \sim 5$). Both of the 70- and 150-μm surveys reach $z \sim 4.5$ and the 50-μm survey reaches $z \sim 3.5$. Hence, the 120-μm survey is preferable to detect high-z galaxies. As for lower redshift region, the number at 150 μm is by one order of magnitude smaller than the others in the range of $0.2 \lesssim z \lesssim 1$, and the number count at 50 μm is by one order of magnitude smaller than that in the other bands at $z \lesssim 0.2$. The redshift distribution of the ASTRO-F galaxies is discussed further in T99.

6.2.5 Treatment of Galaxy Evolution

For galaxy-evolution models, T99 treated pure luminosity evolution and pure density evolution. In this subsection, we briefly review the method to include the evolution effect.

Table 6.2: The minimum $L_{\rm IR}$ detected by ASTRO-F 120-μm survey

Redshift (z)	$L_{\rm lim}(z)$ $[L_\odot]$
0.2	10^{11}
1.0	10^{12}
3.0	10^{13}
5.0	10^{14}

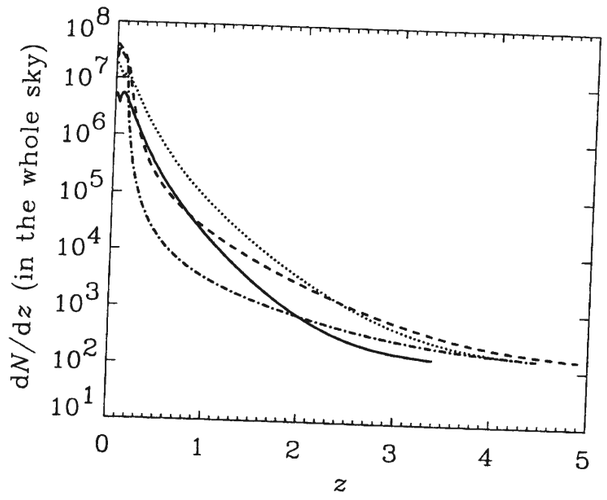

Figure 6.2: Number of the ASTRO-F galaxies per unit z. The solid, dotted, dashed, and dash-dotted lines represent 50-, 70-, 120-, and 150-μm surveys, respectively.

Pure Luminosity Evolution

The pure luminosity evolution model in T99 means that the luminosities of galaxies change as a function of redshift with the functional forms of the luminosity function being fixed (eq. [6.1]). The effect of the luminosity evolution of the galaxies is so modeled that the luminosities of galaxies increase by a factor of $f(z)$ at a redshift z:

$$L_{\rm IR}(z) = L_{\rm IR}(z=0)\, f(z)\,. \tag{6.5}$$

The function $f(z)$ is empirically given in T99 as

$$f(z) = \exp\left[Q\frac{\tau(z)}{t_{\rm H}}\right], \tag{6.6}$$

where Q, $\tau(z)$, and $t_{\rm H}$ are, respectively, a parameter defining the magnitude of evolution, look-back time as a function of z, and the Hubble time $1/H_0$. This means that the timescale of galaxy evolution is $t_{\rm H}/Q$.

Pure Density Evolution

The pure density evolution in T99 means that only the comoving number density of galaxies changes as a function of redshift with the luminosities of the galaxies fixed. The density evolution is so modeled by using a function $g(z)$ that the comoving number density at z is $g(z)$ times larger than that at $z = 0$:

$$\phi(z,\, L_{\rm IR}) = \phi_0(L_{\rm IR})\, g(z)\,, \tag{6.7}$$

where $\phi(z,\, L_{\rm IR})$ is the luminosity function in the comoving volume at the redshift of z. For $g(z)$, T99 adopted the functional form similar to $f(z)$ defined in equation (6.6):

$$g(z) = \exp\left[P\frac{\tau(z)}{t_{\rm H}}\right], \tag{6.8}$$

where P is a parameter representing the magnitude of the evolution.

Determination of Parameters and Observational constraints

In T99, each of the evolutionary parameters (P and Q) is determined by a comparison with the *IRAS* extragalactic source count data. Excluding four statistically poorest points, the values fit best to the data of *IRAS* Point Source Catalog (Joint IRAS Science Working Group 1985) and Hacking & Houck (1987) are $P = 2.7$ or $Q = 1.4$. Recent *ISO* result may indicate stronger evolution (§6.1). The cosmic IR background radiation predicted by the model of T99 is not well reproduced but partially consistent with the DIRBE and FIRAS results (Puget et al. 1996; Fixsen et al. 1998; Hauser et al. 1998) in the FIR region. We note that the sub-mm background radiation predicted by T99 is a few–ten times larger than the DIRBE and FIRAS results. The redshifted dust emission, whose peak is located at 30–100 μm at the rest frame of the galaxy (Figure 1 of T99), largely contributes to the submillimeter background. Thus, constraint on the galaxy evolution in the high-redshift universe from the sub-mm background is suggested to be useful for future work. Indeed recent modeling by Takeuchi et al. (2001b) is motivated by such a constraint. The model is also compared with the SCUBA data (Smail et al. 1997; Hughes et al. 1998; Barger et al. 1998) in Appendix of T99.

6.3 ASTRO-F Galaxies in Optical and NIR Wavelengths

In this section, we estimate the number of the ASTRO-F galaxies for B ($\lambda = 4400$ Å) and H ($\lambda = 16500$ Å) bands. Galaxy evolution is not taken into account at first. The effects of the evolution are considered later in this section (§6.3.3).

6.3.1 Method for Calculation

We calculate the expected numbers of the ASTRO-F galaxies at B and H bands in the following way:

[1] Two populations for the ASTRO-F galaxies are assumed; starburst population and normal spiral population. We define the starburst population as galaxies whose $L_{\rm IR}$ exceeds $10^{10}\ L_\odot$. This classification of the populations corresponds to two different compositions of FIR SEDs in §6.2.1.

[2] For the UV-to-FIR SED of each population, we use averaged SEDs of sample galaxies in Schmitt et al. (1997; Figure 1.1). They collected the nearby galaxies from the catalog of UV IUE spectra (Kinney et al. 1993, 1996), whose ground-based spectra observed with apertures matching that of IUE ($10'' \times 20''$) were available. The sample contains 6 normal spirals and 26 starburst galaxies. The starburst galaxies are divided into two categories: the high-reddened sample (15 galaxies) and the low-reddened sample (11 galaxies) at $E(B-V) = 0.4$. The reddening was calculated in Calzetti, Kinney, & Storchi-Bergmann (1994) from the Balmer decrement. Here, we use the high-reddened sample, so that the UV or optical luminosity density converted from the FIR luminosity density gives fainter estimation. The conversion of $L_{\rm IR}$ to the luminosity for each band (at frequency ν) is made for the two populations using the averaged SEDs as $\mathcal{L}_\nu/\mathcal{L}_{60\,\mu{\rm m}} = \alpha_\nu$, where $\mathcal{L}_\nu = \nu L_\nu$. We should note that $\mathcal{L}_{60\,\mu{\rm m}}$ and $L_{\rm IR}$ are related to each other (§6.2.1). The value of α_ν, which is assumed to be a function of ν only, is listed in Table 6.3. The ratio of luminosity density at ν to that at $60\,\mu$m is kept constant for each population. We should keep in mind that the scatter of α_ν is large (an order of magnitude) in observational data. Since our estimation is made for FIR-selected sample, use of SEDs in Spinoglio et al. (1995), in which the sample was selected at 12 μm, is better. However, we need UV data to evaluate the optical magnitude of galaxies at high redshift, and thus we used the data in Schmitt et al. (1997). It is worth noting that the FIR-to-optical SEDs of 12-μm sample in Spinoglio et al. (1995, their Figure 11) is consistent with the value of α_ν in Table 6.3 within an order-of-magnitude, typical scatter of the data in Schmitt et al. (1997).

Table 6.3: Parameter (α) for the conversion of luminosities.

Population (band)	α^*
Starburst (B) ...	0.10
Normal (B)	4.0
Starburst (H) ...	0.12
Normal (H)	10

NOTE.—$*$ $\alpha = \mathcal{L}_\nu/\mathcal{L}_{60\mu{\rm m}}$, where $\mathcal{L}_\nu = \nu L_\nu$ (L_ν is luminosity density of a galaxy).

[3] The local luminosity function $\phi_0(M_{{\rm AB}\nu})$ (Mpc^{-3} mag^{-1}) is made based on Soifer et al. (1987b) by using the above conversion of the luminosity density. The definition of the AB magnitude ($M_{{\rm AB}\nu}$) is given by Oke and Gunn (1983);

$$M_{{\rm AB}\nu}\,[{\rm mag}] = -2.5 \log f_\nu\,[{\rm erg\ cm^{-2}\ s^{-1}\ Hz^{-1}}] - 48.594\,, \tag{6.9}$$

where $B = M_{\rm AB} + 0.2$ and $H = M_{\rm AB} - 1.4$. The B-band luminosity function is described as follows. For the normal population,

$$\log \phi_0\ [{\rm Mpc^{-3}\ mag^{-1}}] = 5.08 + 0.38 M_{{\rm AB}B,{\rm abs}}, \quad (-19.8 < M_{{\rm AB}B,{\rm abs}} < -14.8). \tag{6.10}$$

where ϕ_0 is the local number density of the ASTRO-F galaxies per magnitude, and the subscript "abs" refers to absolute magnitude. The upper and lower luminosities correspond to $L_{\rm IR} = 10^{10}\ L_\odot$ ($\mathcal{L}_{60\ \mu{\rm m}} = 10^{9.2}\ L_\odot$) and $L_{\rm IR} = 10^{8}\ L_\odot$ ($\mathcal{L}_{60\ \mu{\rm m}} = 10^{7.2}\ L_\odot$), respectively. For the starburst population, double-power-law fitting is executed as follows:

$$\log \phi_0\ [{\rm Mpc^{-3}\ mag^{-1}}] = \begin{cases} 0.02 + 0.16 M_{{\rm AB}B,{\rm abs}} & (-18.0 < M_{{\rm AB}B,{\rm abs}} < -15.8), \\ 12.07 + 0.83 M_{{\rm AB}B,{\rm abs}} & (-25.6 < M_{{\rm AB}B,{\rm abs}} < -18.0), \end{cases} \tag{6.11}$$

where the boundary values for the luminosity correspond to $L_{\rm IR} = 10^{14}\ L_\odot$ ($\mathcal{L}_{60\ \mu{\rm m}} = 10^{13.2}\ L_\odot$; $M_{{\rm AB}B,{\rm abs}} = -25.6$), $L_{\rm IR} = 10^{10.3}\ L_\odot$ ($\mathcal{L}_{60\ \mu{\rm m}} = 10^{10.1}\ L_\odot$; $M_{{\rm AB}B,{\rm abs}} = -18.0$), and $L_{\rm IR} = 10^{10}\ L_\odot$ ($\mathcal{L}_{60\ \mu{\rm m}} = 10^{9.2}\ L_\odot$; $M_{{\rm AB}B,{\rm abs}} = -15.8$). For H band, the luminosity function of the normal population is

$$\log \phi_0\ [{\rm Mpc^{-3}\ mag^{-1}}] = 6.00 + 0.38 M_{{\rm AB}H,{\rm abs}} \quad (-22.2 < M_{{\rm AB}H,{\rm abs}} < -17.2), \tag{6.12}$$

while the starburst luminosity function is

$$\log \phi_0\ [{\rm Mpc^{-3}\ mag^{-1}}] = \begin{cases} 0.10 + 0.15 M_{{\rm AB}H,{\rm abs}} & (-19.6 < M_{{\rm AB}H,{\rm abs}} < -17.4), \\ 13.40 + 0.83 M_{{\rm AB}H,{\rm abs}} & (-27.2 < M_{{\rm AB}H,{\rm abs}} < -19.6). \end{cases} \tag{6.13}$$

The fraction of starburst galaxies is 2% of total number of field galaxies at $M_{{\rm AB}B} \sim -20$ mag (see e.g., Small et al. 1997 for the number density of field galaxies).

[4] The K-corrections, $K(z)$ is expressed by 5-order polynomials fitted to the data of SEDs in Schmitt et al. (1997) as $K(z) = a_1 z + a_2 z^2 + a_3 z^3 + a_4 z^4 + a_5 z^5$. The results of the fitting are presented in Table 6.4. The residual of the fitting of $K(z)$ is less than 0.2 mag in most of the considered z range and 0.5 mag in the worst case; the values are less than the scatter of the luminosity density of the sample in Schmitt et al. (1997).

Table 6.4: The coefficient a_n for the K-correction.

Population (band)	a_1	a_2	a_3	a_4	a_5
Starburst (B)	2.1	−1.2	0.25	-2.3×10^{-2}	7.4×10^{-4}
Normal (B)	5.7	−2.6	−0.39	-1.3×10^{-2}	-4.6×10^{-4}
Starburst (H)	−0.49	0.38	-7.0×10^{-2}	5.2×10^{-3}	-1.4×10^{-4}
Normal (H)	−0.22	0.35	-3.3×10^{-2}	1.1×10^{-4}	3.3×10^{-5}

[5] Finally, the number count of ASTRO-F galaxies per square degree is calculated according to the following formula:

$$N(< M_{\mathrm{AB}\nu}) = \oint \mathrm{d}\Omega \int_0^\infty \mathrm{d}z \int_{M_{\mathrm{AB}\nu,\mathrm{lim}}(z)}^\infty \mathrm{d}\, M_{\mathrm{AB}\nu}\, \phi(M_{\mathrm{AB}\nu}) \frac{\mathrm{d}^2 V}{\mathrm{d}z\, \mathrm{d}\Omega}\,, \tag{6.14}$$

where $M_{\mathrm{AB}\nu,\mathrm{lim}}(z)$ is the limiting magnitude corresponding to $L_{\mathrm{lim}}(z)$ (§6.2.3).

6.3.2 Results

The cumulative number count of ASTRO-F galaxies detected at 20 μm are presented in Figures 6.3*a* (B band) and 6.3*b* (H band). These figures show that number of ASTRO-F galaxies brighter than $B_{\mathrm{AB}} \sim 19$ mag (or $H_{\mathrm{AB}} \sim 16$ mag)[3] increases as the magnitude increases with a slope of 0.6 (dex mag^{-1}), which is the value for the no evolution case in the Euclidean geometry.[4] The figures also show that no ASTRO-F galaxies are detected in the magnitude region fainter than $B_{\mathrm{AB}} \sim 22$ mag (or $H_{\mathrm{AB}} \sim 21$ mag) for starbursts and $B_{\mathrm{AB}} \sim 19$ mag (or $H_{\mathrm{AB}} \sim 16$ mag) for normal spirals. Each of these magnitudes corresponds to optical flux density of each population, which is detected at the flux limit of the ASTRO-F survey. About 60 normal galaxies and 80 starbursts per square degree are detected within this limit. The redshifts of normal spirals are less than 0.1 (T99), as expected from the slope of the counts. In Figures 6.4*a* and 6.4*b*, we also present the number count of starbursts in various redshift range ($z < 0.2$, $0.2 < z < 1$, $1 < z < 3$, and $3 < z$) in the case of the 120-μm survey. About 90% of the starbursts detected by ASTRO-F are located at the redshift of $z < 0.2$ (40% at $z < 0.1$ and 50% at $0.1 < z < 0.2$). For $z \lesssim 3$, the ASTRO-F galaxies are brighter than $B_{\mathrm{AB}} \sim 22$ (or $H_{\mathrm{AB}} \sim 20$), corresponding to the detection limit of ASTRO-F. One high-z ($z > 3$) galaxy exists per ~ 10 square degrees.

We used the high-reddened SED of Schmitt et al. (1997) as that of starburst galaxies (subsection 6.3.1). The UV-to-FIR ratio of the luminosity density for the low-reddedned SED is about twice as large as that for the high-reddened SED. Thus, the optical counterpart of ASTRO-F galaxies may be brighter than is expected in this chapter by two times (~ 0.8 mag), if the dust extinction is lower. Even if the deceleration parameter of the universe is not 0.1, but 0.5, there is no significant change in the detected number at $z \lesssim 2$. The number increases by 20% around $z = 3$.

6.3.3 Effects of Galaxy Evolution

Guiderdoni et al. (1997) calculated the number count of galaxies in FIR wavelength based on models constructed through detailed physical processes related to the evolution of galaxies (see also Franceschini et al. 1994). However, there is a great deal of theoretical uncertainty concerning the physical processes governing galaxy formation and evolution. Indeed, the primary motivation of the *semianalytic* model as Gioderdoni et al. (1997) is to search the parameter space of galaxy formation and evolution and to investigate the response of the result to the parameters (e.g., White & Frenk 1991; Lacey & Cole 1993). In the model, one starts from a power spectrum of primordial density fluctuations, follows the formation and merging of dark matter halos, and adopts various prescriptions for gas cooling, star formation, and feedback. Here, we adopt an "empirical approach" based on the luminosity

[3] B_{AB} and H_{AB} are the apparent AB magnitudes in B and H bands, respectively.

[4] The slope is explained in §6.4.

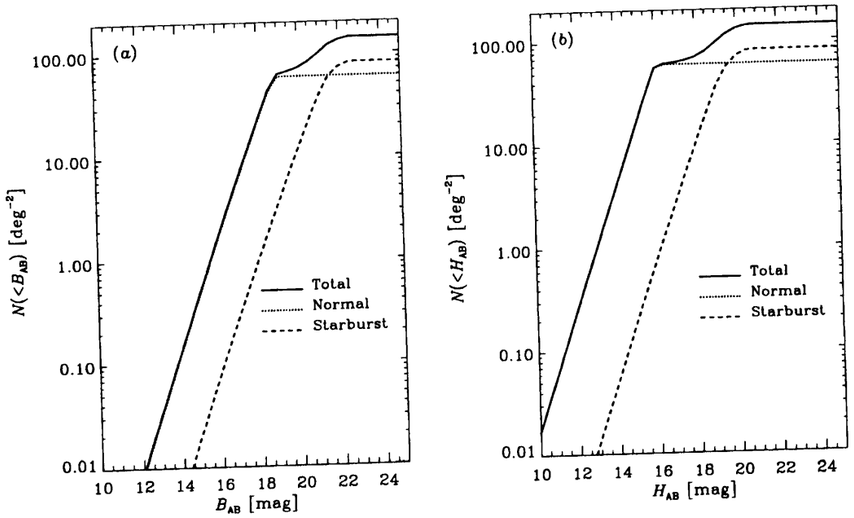

Figure 6.3: (a) Cumulative number count of the ASTRO-F galaxies in the B band (per square degree). The dotted and dashed lines represent the number of normal and starburst populations, respectively. The total number count is also shown with the solid line. (b) Same as (a), but in the H band.

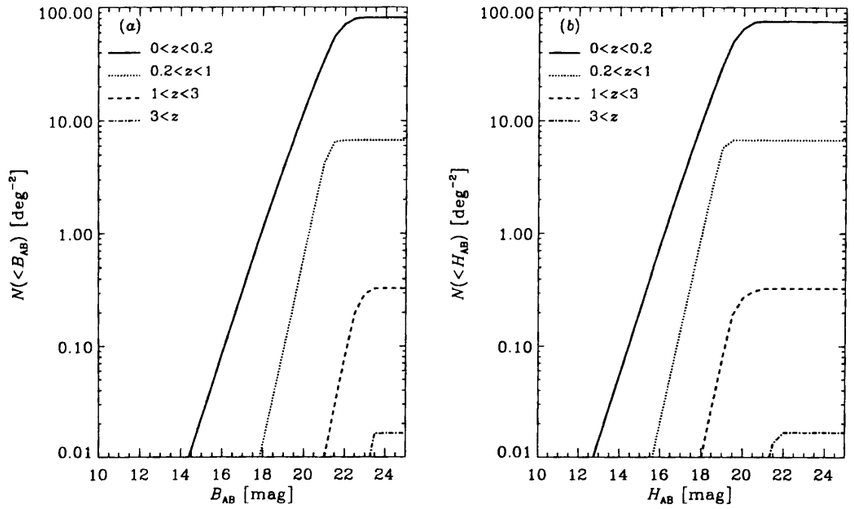

Figure 6.4: (a) Cumulative number counts of the starburst population in various ranges of redshift in the B band. The solid line represents the number count of starbursts in the redshift range of $0 < z < 0.2$, the dotted line $0.2 < z < 1$, the dashed line $1 < z < 3$, and the dash-dotted line $3 < z$. (b) Same as (a), but in the H band.

function and SEDs observed in the local universe. "Empirical" means that the model is based on observational data.

We only investigate the pure luminosity evolution defined in T99 and §6.2.5. The evolution with the parameter $Q = 1.4$, which T99 determined by using *IRAS* extragalactic source count data, is examined here. This model shows the luminosity evolution by a factor of 1.9 at $z = 1$, 2.4 at $z = 2$, and maintains this evolutionary factor in $z \gtrsim 2$. We assume for simplicity that the luminosity of galaxies evolves in such a way that the ratio of FIR to optical luminosity is kept constant. Apparently, the photometric evolution model from optical to FIR range should be included in the future. The spectral evolution model as described in §5.2.3 will be useful.

Figures 6.5*a* and 6.5*b* present the effect of evolution for the starburst population. Since almost all of the ASTRO-F galaxies reside in low-z areas, the effect of galaxy evolution is not significant (increase of about 20%). We also present the number count for various range of z in Figures 6.6*a* and 6.6*b*. Comparing Figures 6.4 and 6.6, we see that the effect of evolution is significant for high-z galaxies; the number of low-z ($z < 1$), intermediate-z ($1 < z < 3$), and high-z ($z > 3$) galaxies is 100, 20, and 0.2 per square degree, respectively.

The intensity of cosmic IR background radiation (e.g., Fixen et al. 1998) also constrains the magnitude of galaxy evolution. Since $Q = 1.4$ is almost the upper limit, stronger evolutions with our model break the constraint (T99). The density evolution of the luminosity function in T99 gives almost the same results, since the parameter for the density evolution is determined from the same calibration as that of the luminosity evolution (see T99 for details).

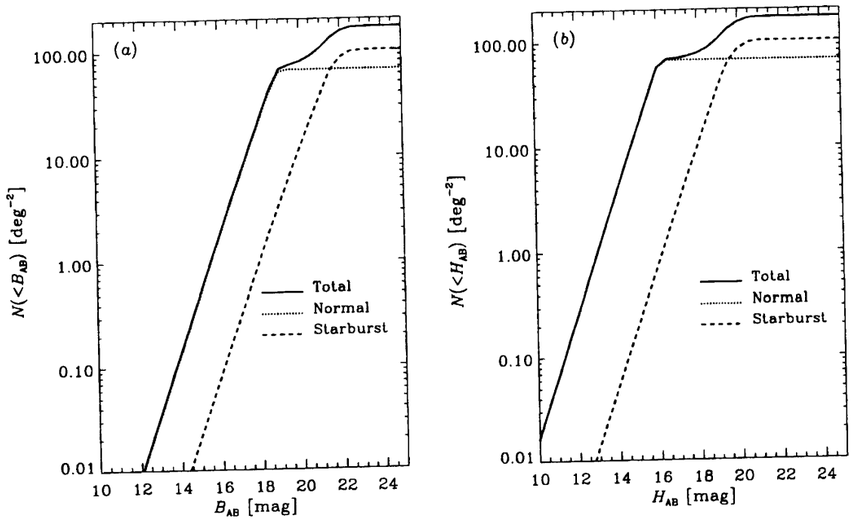

Figure 6.5: (a) Cumulative number count of the starburst population with our luminosity-evolution model (*solid line*). The dashed line indicates the count without evolution. (b) Same as (a) but at H band.

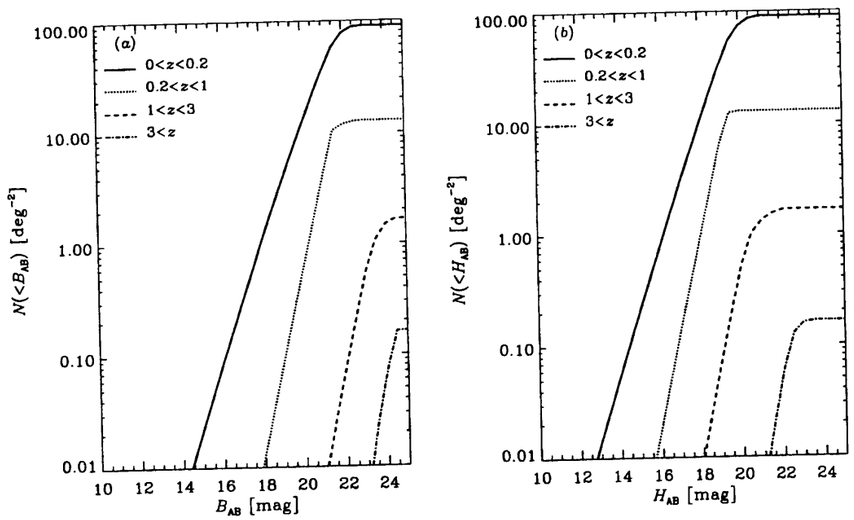

Figure 6.6: (a) Number counts of the starburst population with the luminosity evolution in various ranges of redshift in the B band (the meaning of the lines are the same as Fig. 6.4*a*). (b) Same as (a) but in the H band.

6.4 Supplementary Review: Slope of Number Count

As stated in §6.3.2, the slope of the number count in the Eucledian universe is 0.6. This slope is derived as follows. Let us start with the relation between the luminosity L and flux S:

$$4\pi d^2 S = L\,, \tag{6.15}$$

The number count $N(>S)$ (the number of galaxies whose flux is brighter than S) is expressed as

$$N(>S) = \int \phi(L)\,\frac{4\pi}{3} d^3\,\mathrm{d}L \propto S^{-3/2}\,, \tag{6.16}$$

where $\phi(L)$ is the luminosity function ($\phi(L)\,\mathrm{d}L$ is the number of galaxies whose luminosity is between L and $L+\mathrm{d}L$ per unit volume). Since the magnitude is defined as $m = 2.5\log S +$ constant, we obtain

$$\log N(>S) = 0.6m + \text{constant}\,. \tag{6.17}$$

6.5 Summary and Future Strategy

We adopted the "empirical approach" model to predict the optical and NIR number count of galaxies expected to be detected by ASTRO-F. This model is based on the local observed data of *IRAS*, and is an extension of the *IRAS* results to a high-z universe. According to our model, such ASTRO-F galaxies have magnitude $m_{\mathrm{AB}\nu} \lesssim 21$ at the B and H bands. The expected number of ASTRO-F galaxies at B and H bands per square degree is estimated to be 80 for starburst galaxies and 60 for normal spirals. This value is about 10% of the optical/NIR number count at the same magnitude. As for the redshift distribution, almost all of the normal galaxies are located at $z \lesssim 0.1$, and about 40% of the starburst galaxies are at $z < 0.1$, 50% at $0.1 < z < 0.2$, 10% at $0.2 < z < 1$, and 1% at $z > 1$.

By considering the results obtained above together with the effects of the evolutions, the scientific targets of optical/NIR follow-up observations of ASTRO-F galaxies would be twofold:

[1] The star formation history as well as a large-scale structure of the universe up to $z \sim 1$ is traced. The environmental effects on star formation in galaxies will be an important issue.

[2] Extremely bright starburst galaxies in a high-z universe is searched. They may be in an early stage of galaxy evolution.

ASTRO-F is expected to determine the position of a FIR source with an accuracy of 5″ (Kawada 1998), which is estimated based on the accuracy of telescope pointing and of fitting to a beam profile. The observed number counts of galaxies in the b_{J} and K bands show that about 10^{-2} galaxies exist in a $5'' \times 5''$ field at an AB magnitude of 21 mag (e.g., Broadhurst, Ellis, & Glazebrook 1992). This means that a chance coincidence between ASTRO-F galaxies and normal optical galaxies is negligible within this magnitude limit, and thus we can select optical counterpart of ASTRO-F galaxies almost uniquely. Since the expected redshifts of most of such ASTRO-F galaxies are low ($z \lesssim 1$), the optical spectroscopy will be good enough to determine the redshifts and natures of the sources. Considering that the number density of

ASTRO-F galaxies brighter than $m_{\mathrm{AB}} \simeq 21$ mag is $\sim 100\ \mathrm{deg}^{-2}$, a multi-object spectrograph with a wide field of view (such as a fiber multi-object spectrograph) equipped to a 4–8-m class telescope is the best instrument to follow up the ASTRO-F survey. The obtained database will be used to trace the SFH and large scale structures up to $z \sim 1$.

It will be very inefficient to find high-z ultra-luminous FIR galaxies in such a survey described in the previous paragraph because of its very low surface density. We need another approach to obtain a sample of high-z ultra-luminous FIR galaxies. It is expected that we can make a rough estimate of the redshifts of ASTRO-F galaxies based on a FIR color–color diagram of the sources by using three ASTRO-F bands, as described in T99. Takeuchi et al. (2001a) extended this technique to the sub-mm wavelength. Their basic idea is based on the fact that the peaks in the spectra of the thermal radiation from the heated dust at high z is redshifted to a longer wavelength. After selecting the high-z galaxies based on their FIR colors, we need to conduct deep spectroscopic observations which target these objects. Since such high-z objects will have faint magnitude ($m_{\mathrm{AB}} \lesssim 23$), any optical counterparts may not be uniquely identified; chance probability is not negligible in this magnitude range. Furthermore, "dusty" galaxies may have fainter optical magnitude. Thus, deep multislit optical/NIR spectroscopy or the integral field unit of a field of view of $\sim 10''$ will be required. Since making slitlets in a 5″–10″ region would be difficult, the fiber spectroscopy would be the most efficient way to identify the FIR source. Subaru telescope will be equipped with Fiber Multi-Object Spectrograph (Maihara et al. 2000), which will be useful in the follow-up observations.

REFERENCES

Aannestad, P. A., 1978, ApJ, 220, 538

Adams, T. F. 1972, ApJ, 174, 439

Allamandola, L. J., Tielens, A. G. G. M., & Barker, J. R. 1989, ApJS, 71, 733

Arimoto, N., & Yoshii, Y., 1986, A&A, 164, 260

Baker, J. G., & Menzel, D. H. 1938, ApJ, 88, 52

Barger, A. J., Cowie, L. L., Sanders, D. B., Fulton, E., Taniguchi, Y., Sato, Y., Kawara, K., & Okuda, H. 1998, Nature, 394, 248

Barlow, M. J. 1978, MNRAS, 183, 367

Beichman, C. A., & Helou, G. 1991, ApJ, 370, L1

Blain, A. W. MNRAS, 295, 92

Borghesi, A., Bussoletti, E., Colangeli, L. 1987, ApJ, 314, 422

Broadhurst, T. J., Ellis, R. S., Glazebrook, K. 1992, Nature, 355, 55

Bruzual, A., & Charlot, S. 1993, ApJ, 405, 538

Buat, V., & Xu, C. 1996, A&A, 306, 61

Cappellaro, E., Turatto, M., Benetti, S., Tsvetkov, D. Yu., Bartunov, O. S., & Makarova, I. N. 1993, A&A, 273, 383

Carleton, N. P., Elvis, M., Fabbiano, G., Willner, S. P., Lawrence, A., & Ward, M. 1987, ApJ, 318, 595

Cen, R., & Ostriker, J. P. 1999, ApJ, 519, L109

Charlot, S., Worthey, G., & Bressan, A. 1996, ApJ, 367, 126

Cohen, J. G. 1977, ApJ, 214, 86

Connolly, A. J., Szalay, A. S., Dickinson, M., SubbaRao, M. U., & Brunner, R. J. 1997, ApJ, 486, L11

Cowie, L. L. 1978, ApJ, 225, 887

Cox, N. 2000, Allen's Astrophysical Quantities, 4th ed. (New York: Springer)

Dahlem, H. 1997, PASP, 109, 1298

Debye, P. 1909, Ann. Phys., NY 30, 59

DeGioia-Eastwood, K. 1992, ApJ, 397, 542

Désert, F.-X., Boulanger, F., & Puget, J. L. 1990, A&A, 237, 215

Devereux, N. A. 1996, in New Extragalactic Perspectives in the New South Africa, ed. D. L. Block & J. M. Greenberg (Dordrecht: Kluwer), 357

Devereux, N. A., & Hameed, S. 1997, AJ, 113, 599

Draine, B. T. 1990, in Evolution of the Interstellar Medium, ed. L. Blitz (San Francisco: ASP), 193

Draine, B. T., & Lee, H. M. 1984, ApJ, 285, 89

Draine, B. T., & Salpeter, E. E. 1979, ApJ, 231, 438

Dwek, E. 1998, ApJ, 501, 643

Dwek, E., & Scalo, J. M. 1980, ApJ, 239, 193

Efstathiou, A., Rowan-Robinson, M., Siebenmorgen, T. 2000, MNRAS, 313, 734

Eggen, O. J., Lynden-Bell, D., & Sandage, A. R. 1962, ApJ, 136, 748

Emerson, D. 1996, Interpreting Astronomical Spectra (New York: Wiley)

Ferrara, A., & Tolstoy, E. 2000, MNRAS, 313, 291

Fixsen, D. J., Dwek, E., Mather, J. C., Bennett, C. L., & Shafer, R. A. 1998, ApJ, 508, 123

Franceschini, A., Mazzei, P., De Zotti, G., Danese, L. 1994, ApJ, 427, 140

Gallagher, J. S., Bushouse, H., & Hunter, D. A. 1989, AJ, 97, 700

Gehrz, R. D. 1989, in IAU Symp. 135, Interstellar Dust, ed. L. J. Allamandora & A. G. G. M. Tielens (Dordrecht: Kluwer), 445

Gispert, R., Lagache, G.,& Puget, J. L. 2000, A&A, 360, 1

Glass, I. S. 1999, Handbook of Infrared Astronomy (Cambridge: Cambridge University Press)

Guiderdoni, B., Hivon, E., Bouchet, F. R., & Maffei, B. 1998, MNRAS, 295, 877

Guiderdoni, B., & Rocca-Volmerange, B. 1987, A&A, 186, 1

Habe, A., Ikeuchi, S., & Tanaka, Y. D. 1981, PASJ, 33, 23

Habing, H. 1968, Bull. Astr. Inst. Netherlands, 19, 421

Hacking, P., Condon, J. J., & Houck, J. R. 1987, ApJ, 316, L15

Hacking, P., & Houck, J. R. 1987, ApJS, 63, 311

Hameed, S., & Devereux, N. 1999, AJ, 118, 730

Harper, D. A., & Low, F. J. 1971, ApJ, 165, L9

Hartmann, D., & Burton, W. B. 1997, Atlas of Galactic Neutral Hydrogen (Cambridge: Cambridge University Press)

Hauser, M. G., et al. 1998, ApJ 508, 25

Hildebrand, R. H. 1983, QJRAS, 24, 167

Hirashita, H. 1999a, ApJ, 510, L99

Hirashita, H. 1999b, ApJ, 522, 220

Hirashita, H. 2000a, PASJ, 52, 107

Hirashita, H. 2000b, ApJ, 531, 693

Hirashita, H., Burkert, A., & Takeuchi, T. T. 2001, ApJ, submitted

Hirashita, H., Inoue, A. K., Kamaya, H., & Shibai, H. 2001, A&A, in press

Hirashita, H., & Kamaya, H. 2000, AJ, 120, 728

Hirashita, H., Takeuchi, T. T., Ohta, K., & Shibai, H. 1999, PASJ, 51, 81

Hughes, D. H, et al. 1998, Nature, 394, 241

Ikeuchi, S. 1988, Fundam. Cosmic Phys., 12, 255

Ikeuchi, S., Habe, A., & Tanaka, Y. D. 1984, MNRAS, 207, 909

Ikeuchi, S., & Tomita, H. 1983, PASJ, 35, 77 (IT83)

Inoue, A. K., Hirashita, H., & Kamaya, H. 2000a, PASJ, 52, 539 (IHK00)

Inoue, A. K., Hirashita, H., & Kamaya, H. 2000b, AJ, 120, 2415

Issa, M. R., MacLaren, I., & Wolfendale, A. W. 1990, A&A, 236, 237

Joint IRAS Science Working Group 1985, IRAS Point Source Catalog (Washington DC: GPO)

Jones, A. P., Tielens, A. G. G. M., & Hollenbach, D. J. 1996, ApJ, 469, 740

Jura, M., Kim, D. W., Knapp, G. R., & Guhathakurta, P. 1987, ApJ, 312, L11

Kamaya, H., & Hirashita, H. 2001, PASJ, submitted

Kamaya, H., & Takeuchi, T. T. 1997, PASJ, 49, 471 (KT97)

Kawada M. 1998, in Infrared Astronomical Instrumentation, Proc. SPIE, 3354, 905

Kawara, K., et al. 1998, A&A, 336, L9

Keel, W. C. 1983, ApJ, 268, 632

Kennicutt, R. C. Jr. 1998a, ARA&A, 36, 189

Kennicutt, R. C. Jr. 1998b, ApJ, 498, 541

Kennicutt, R. C. Jr., Tamblyn, P., Congdon, C. W. 1994, ApJ, 435, 22 (KTC94)

Kessler, M. F., et al. 1996, A&A, 315, L27

Kinney, A. L., Bohlin, R. C., Calzetti, D., Panagia, N., Wyse, R. F. G. 1993, ApJS, 86, 5

Kinney, A. L., Calzetti, D., Bohlin, R. C., McQuade, K., Storchi Bergmann, T., & Schmitt, H. R. 1996, ApJ, 467, 38

Knapp, G. R., Guhathakurta, Puragra, Kim, D.-W., Jura, M. A. 1989, ApJS, 70, 329

Korchagin, V. I., Ryabtsev, A. D., & Vorobyov, E. I. 1994, Ap&SS, 220, 115

Kodama, T., & Arimoto, N. 1997, A&A, 320, 41

Kozasa T., Hasegawa H., & Nomoto K. 1989, ApJ, 344, 325

Lacey, C. G., & Cole, S. 1993, MNRAS, 262, 627

Léger, A., & Puget, J. L. 1984, A&A, 137, L5

Leitherer, C., & Heckman, T. M. 1995, ApJS, 98, 9

Lilly, S. J., Tresse, L., Hammer, F., Crampton, D., & Le Fèvre, O. 1995, ApJ, 455, 108

Lilly, S. J., Le Fèvre, O., Hammer, F., & Crampton, D. 1996, ApJ, 460, L1

Lisenfeld, U., & Ferrara, A. 1998, ApJ, 496, 145

Lonsdale Persson, C. J., & Helou, G. 1987, ApJ, 314, 531

Lucy, L. B., Danziger, I. J., Gouiffes, C., & Bouchet, P. 1991, in Supernovae, The Tenth Santa Cruz Workshop in Astronomy and Astrophysics (New York: Springer), 82

Lynden-Bell, D. 1975, Vistas in Astronomy, 19, 299

Madau, P., Ferguson, H. C., Dickinson, M. E., Giavalisco, M., Steidel, C. C., & Fruchter, A. 1996, MNRAS, 283, 1388

Madau, P., Pozzetti, L., & Dickinson, M. 1998, ApJ, 498, 106

Maihara, T., Oda, N., Shibai, H., & Okuda, H. 1981, A&A, 97, 139

Maihara, T., et al. 2000, in Optical and IR Telescope Instrumentation and Detectors, Proc. SPIE, 4008, 1111

Malhotra, S., et al. 1996, A&A, 315, L161

Marlowe, A. T., Heckman, T. M., Wyse, R. F. G., & Schommer, R. 1995, ApJ, 438, 563

Marlowe, A. T., Meurer, G. R., & Heckman, T. M. 1999, ApJ, 522, 183

Mathis, J. S., Rumpl, W., & Nordsieck, K. H. 1977, ApJ, 217, 425 (MRN)

Matsuhara, H., et al. 2000, A&A, 361, 401

Matteucci, F., & François, P. 1989, MNRAS, 239, 885

Matsumoto, T. 2000, in Proc. SPIE, UV, Optical and IR Space Telescopes and Instruments, ed. J. B. Breckinridge & J. Jakobsen, 4013

Mazzei, P., Xu, C., & De Zotti, G. 1992, A&A, 256, 45

McKee, C. F. 1989, in IAU Symp. 135, Interstellar Dust, ed. L. J. Allamandola & A. G. G. M. Tielens, (Dordrecht: Kluwer), 431

McKee, C. F., & Ostriker, J. P. 1977, ApJ, 218, 148

Mebold, U., Winnberg, A., Kalberla, P. M. W., & Goss, W. M. 1982, A&A, 115, 223

Meurer, G. R., Heckman, T. M., & Calzetti, D. 1999, ApJ, 521, 64

Mezger, P. G., 1978, A&A, 70, 565

Mie, G. 1908, Ann. Phys., NY 25, 377

Misselt, K. A., Clayton, G. C., & Gordon, K. D. 1999, ApJ, 515, 128

Moorwood, A. F. M., 1996, Space Science Reviews, 77, 303

Mouri, H., Taniguchi, Y., Sato, Y., & Kawara, K. 1998, A&A, 334, 482

Moseley S. H., Dwek E., Glaccum W., Graham J. R., Loewenstein R. F., & Silverberg R. F. 1989, Nature, 340, 697

Murakami, H., et al. 1996, PASJ, 48, L41

Murakami, H. 1998, in Proc. SPIE, Space Telescope and Instruments V, ed. P. Y. Bely & J. B. Breckinridge, 3356

Myers, P. C. 1978, ApJ, 225, 380

Neugebauer, G., Miley, G. K., Soifer, B. T., & Clegg, P. E. 1986, ApJ, 308, 815

Nicolis, G., & Prigogine, I. 1977, Self-Organization in Nonequilibrium Systems (New York: Wiley and Sons)

Nishi, R., & Tashiro, M. 2000, ApJ, 537, 50

Nozakura, T., & Ikeuchi, S. 1984, ApJ, 279, 40

Nozakura, T., & Ikeuchi, S. 1988, ApJ, 333, 68

Oke, J. B., & Gunn, J. E. 1983, ApJ, 266, 713

Onaka, T., Yamamura, I., Tanabe, T., Roellig, T., Yuen, L. 1996, PASJ, 48, L59

Oliver, S., et al. 2000, MNRAS, 316, 749

Osterbrock, D. E. 1989, Astrophysics of Gaseous Nebulae and Active Galactic Nuclei, (California: University Science Books)

Oyabu, S., et al. 2001, A&A, in press

Papoular, R., Conard, J., Giuliano, M., Kister, J., & Mille, G. 1989, A&A, 217, 204

Partridge, R. B., & Peebles, P. J. E. 1967, ApJ, 148, 377

Pearson C. 1996, PhD Thesis, Imperial College of Science Technology

Pei, Y. C., & Fall, S. M. 1995, ApJ, 454, 69

Pei, Y. C., Fall, S. M., & Hauser M. G. 1999, ApJ, 522, 604

Peterson, R. C. & Caldwell, N., 1993, AJ, 105, 1411

Petrosian, V., Silk, J., & Field, G. B. 1972, ApJ, 177, L6

Piatek, S. & Pryor, C., 1995, AJ, 109, 1071

Pipher, J. L. 1973, in IAU Symp. 52, Interstellar Dust and Related Topics, ed. J. M. Greenberg & H. C. van de Hulst (Dordrecht: Reidel), 559

Popescu, C. C., Misiriotis, A., Kylafis, N. D., Tuffs, R. J., & Fischera, J. 2000, A&A, 362, 138

Purcell, E. M. 1969, ApJ, 158, 433

Puget, J.-L., Abergel, A., Bernard, J.-P., Boulanger, F., Burton, W. B., Désert, F.-X., & Hartmann, D. 1996, A&A 308, L5

Puget, J.-L., et al. 1999, A&A, 345, 29

Roberts, M. S. 1963, ARA&A, 1, 149

Rocha-Pinto, H. J., Scalo, J., Machiel, W., & Flynn, C. 2000, ApJ, 531, L115

Routly, P. M., & Spitzer, L., Jr. 1952, ApJ, 115, 227

Rowan-Robinson, M. 1980, ApJS, 44, 403

Rowan-Robinson, M., & Crawford, J. 1989, MNRAS, 238, 523

Rownd, B. K., & Young, J. S. 1999, AJ, 118, 670

Sakata, A., Wada, S., Onaka, T., Tokunaga, A. T. 1987, ApJ, 320, L63

Salpeter, E. E. 1955, ApJ, 121, 161

Sandage, A. 1986, A&A, 161, 89

Sanders, D. B., & Mirabel, I. F. 1996, ARA&A, 34, 749

Sanders, D. B., Phinney, E. S., Neugebauer, G., Soifer, B. T., & Matthews, K. 1989, ApJ, 347, 29

Sanders, D. B., Soifer, B. T., Elias, J. H., Madore, B. F., Matthews, K., Neugebauer, G., & Scoville, N. Z. 1988, ApJ, 325, 74

Saunders, W., Rowan-Robinson, M., Lawrence, A., Efstathiou, G., Kaiser, N., Ellis, R. S., & Frenk, C. S. 1990, MNRAS, 242, 318

Sauvage, M., & Thuan, T. X. 1992, ApJ, 396, L69

Sauvage, M., et al. 1996, A&A, 315, L89

Savage, B. D., Mathis, J. S. 1979, ARA&A, 17, 73

Scalo, J. M. 1986, Fundam. Cosmic Phys., 11, 1

Scalo, J. M., & Struck-Marcell, C. 1986, ApJ, 301, 77

Schmidt, M. 1959, 129, 243

Schmitt, H. R., Kinney, A. L., Calzetti, D., Storchi Bergmann, T. 1997, AJ, 114, 592

Seab, C. G. 1987, in Interstellar Processes: Proceedings of the Symposium on Interstellar Processes, ed. D. J. Hollenbach & H. A. Thronson (Dordrecht: Reidel), 491

Searle, L., & Zinn, R. 1978, ApJ, 225, 357

Shibai, H., Okumura, K., & Onaka, T. 1999, in Star Formation 1999, ed. T. Nakamoto (Nobeyama: Nobeyama Radio Observatory), 67

Silva, L., Granato, G. L., Bressan, A., & Danese, L. 1998, ApJ, 509, 103

Slavin, J. D., & Cox, D. P. 1992, ApJ, 392, 131

Smail, I, Ivison, R. J., & Blain, A. W., 1997, ApJ, 507, L21

Smail, I, Ivison, R. J., Blain, A. W., & Kneib, J.-P. 1998, ApJ, 507, L21

Small, T. A., Sargent, W. L. W., Hamilton, D. 1997, ApJ, 487, 512

Soifer, B. T., Houck, J. R., & Neugebauer, G. 1987a, ARA&A 25, 187

Soifer, B. T., Sanders, D. B., Madore, B. F., Neugebauer, G., Danielson, G. E., Elias, J. H., Lonsdale, C. J., & Rice, W. L. 1987b, ApJ, 320, 238

Sommer-Larsen, J. 1996, ApJ, 457, 118

Solomon, P. M., Downes, D., & Raddord, S. J. E. 1992, ApJ, 387, L55

Spinoglio, L., Malkan, M. A., Rush, B., Carrasco, L., Recillas-Cruz, E. 1995, ApJ, 453, 616

Spitzer, L. Jr., 1978, Physical Processes in the Interstellar Medium (New York: Wiley) (S78)

Stecker, F. W., Puget, J. L., & Fazio, G. G. 1977, ApJ, 214, L51

Steidel, C. C., Adelberger, K. L., Giavalisco, M., Dickinson, M., & Pettini, M. 1996, ApJ, 462, 17

Steidel, C. C., Adelberger, K. L., Giavalisco, M., Dickinson, M., & Pettini, M. 1999, ApJ, 519, 1

Tainaka, K., Fukazawa, S., & Mineshige, S. 1993, PASJ, 45, 57

Tajiri, Y. Y., & Kamaya, H. 2001, ApJ, submitted

Takagi, T., Arimoto, N., & Vansevičius, V. 1999, ApJ, 523, 107

Takahashi, H., et al. 2000, in UV, Optical, and IR Space Telescopes and Instruments, ed. J. B. Breckinridge & J. Jacobsen, Proc. SPIE, 4013, 47

Takeuchi, T. T., & Hirashita, H. 2000, ApJ, 540, 217

Takeuchi, T. T., Hirashita, H., Ohta, K., Hattori, T. G., Ishii, T. T., & Shibai, H. 1999, PASP, 111, 288 (T99)

Takeuchi, T. T, Kawabe, R., Kohno, K., Nakanishi, K., Ishii, T. T., Hirashita, H., & Yoshikawa, K. 2001a, PASP, submitted

Takeuchi, T. T., Ishii, T. T., Hirashita, H., Yoshikawa, K., Matsuhara, H., Kawara, K., & Okuda, H. 2001b, PASJ, 53, in press

Tamura, N., Hirashita, H., & Takeuchi, T. T. 2001, ApJ, submitted

Tielens, A. G. G. M., & Allamandola, L. J. 1987, in Interstellar Processes, ed. D. J. Hollenbach & H. A. Thronson (Dordrecht: Reidel), 333

Tinsley, B. M. 1972, A&A, 20, 383

Tinsley, B. M. 1980, Fundam. Cosmic Phys., 5, 287

Todini, P., & Ferrara, A. 2001, MNRAS, submitted (astro-ph/0009176)

Tomita, A., Takeuchi, T. T., & Hirashita, H. 1999, in Star Formation 1999, ed. T. Nakamoto (Nobeyama: Nobeyama Radio Observatory), 50

Tomita, A., Tomita, Y., & Saitō, M. 1996, PASJ, 48, 285

Trumpler, R. J. 1930a, PASP, 42, 214

Trumpler, R. J. 1930b, PASP, 42, 267

Usui, T., Saitō, M., & Tomita, A. 1998, AJ, 116, 2166

van de Hulst, H. C. 1946, Rech. Astron. Obs. Utrecht, 11, 1

Veilleux, S., Kim, D.-C., Sanders, D. B., Mazzarella, J. M., & Soifer, B. T. 1995, ApJS, 98, 171

Wang, B. 1991, ApJ, 374, 456

Wang, B., & Heckman, T. M. 1996, ApJ, 457, 645

White, S. D. M., & Frenk, C. S. 1991, ApJ, 379, 25

Whittet, D. C. B. 1988, in Dust in the Universe, ed. M. E. Bailey & D. A. Williams (Cambridge: Cambridge University Press), 25

Whittet, D. C. B. 1992, Dust in the Galactic Environment (New York: Inst. Phys.)

Xu, C., & Buat, V. 1995, A&A, 293, L65

Young, J. S., Allen, L., Kenney, J. D. P., Lesser, A., & Rownd, B. 1996, AJ, 112, 1903

Part IV

Research Activity

Paper List

[1] Hiroyuki Hirashita, Hideyuki Kamaya, Shin Mineshige (1997)
"The influence of Galactic wind upon the star formation histories of Local Group galaxies"
Monthly Notices of Royal Astronomical Society **290**, L33–L35

[2] Hiroyuki Hirashita, Tsutomu T. Takeuchi, Naoyuki Tamura (1998)
"Physical Interpretation of the Mass-Luminosity Relation of Dwarf Spheroidal Galaxies"
The Astrophysical Journal Letters **504**, L83–L86

[3] Hiroyuki Hirashita (1999)
"Global Law for Dust-to-Gas Ratio of Spiral Galaxies"
The Astrophysical Journal Letters **510**, L99–L102

[4] Hiroyuki Hirashita, Tsutomu T. Takeuchi, Kouji Ohta, Hiroshi Shibai (1999)
"Optical Number Count Estimation of IRIS Far-Infrared Survey of Galaxies"
Publications of the Astronomical Society of Japan **51**, 81–90

[5] Tsutomu T. Takeuchi, Hiroyuki Hirashita, Kouji Ohta, Takashi G. Hattori, Takako T. Ishii, Hiroshi Shibai (1999)
"The *IRIS* Far-Infrared Galaxy Survey: Expected Number Count, Redshift, and Perspective"
Publications of the Astronomical Society of the Pacific **111**, 288–305

[6] Hiroyuki Hirashita (1999)
"Dust-to-Gas Ratio and Phase Transition of Interstellar Medium"
Astronomy & Astrophysics **344**, L87–L89

[7] Hiroyuki Hirashita, Tsutomu T. Takeuchi, Hideyuki Kamaya (1999)
"Implication of Dark Matter in Dwarf Spheroidal Galaxies"
Publications of the Astronomical Society of Japan **51**, 375–381

[8] Hiroyuki Hirashita (1999)
"Evolution of Interstellar Clouds in Local Group Dwarf Spheroidal Galaxies in the Context of their Star Formation Histories"
The Astrophysical Journal **520**, 607–612

[9] Hiroyuki Hirashita (1999)
"Dust-to-Gas Ratio and Metallicity in Dwarf Galaxies"
The Astrophysical Journal **522**, 220–224

[10] Naoyuki Tamura, Hiroyuki Hirashita (1999)
"Observational Test of Environmental Effects on the Local Group Dwarf Spheroidal Galaxies"
The Astrophysical Journal Letters **525**, L17–L20

[11] Hiroyuki Hirashita (2000)
"Intermittent Star-Formation Activities of Dwarf Irregular Galaxies"
Publications of the Astronomical Society of Japan **52**, 107–112

[12] Hiroyuki Hirashita (2000)
"Cyclic Changes in Dust-to-Gas Ratio"
The Astrophysical Journal **531**, 693–700

[13] Akio K. Inoue, Hiroyuki Hirashita, Hideyuki Kamaya (2000)
"Conversion Law of Infrared Luminosity to Star Formation Rate for Galaxies"
Publications of the Astronomical Society of Japan, **52**, 539–543

[14] Hiroyuki Hirashita, Hideyuki Kamaya (2000)
"Application of the Limit-Cycle Model to Star Formation Histories in Spiral Galaxies: Variation among Morphological Types"
The Astronomical Journal, **120**, 728–732

[15] Hiroyuki Hirashita (2000)
"Dust Growth Timescale and Mass Function of Molecular Clouds in the Galaxy"
Publications of the Astronomical Society of Japan, **52**, 585–588

[16] Tsutomu T. Takeuchi, Hiroyuki Hirashita (2000)
"Testing Intermittency of the Galactic Star Formation History along with the Infall Model"
The Astrophysical Journal, **540**, 217–223

[17] Akio K. Inoue, Hiroyuki Hirashita, Hideyuki Kamaya (2000)
"Star Formation Efficiency in the Central 1 kpc Region of Early Spiral Galaxies"
The Astronomical Journal, **120**, 2415–2422

[18] Hiroyuki Hirashita, Akio K. Inoue, Hideyuki Kamaya, Shibai, H. (2001)
"Emission from Dust in Galaxies: Metallicity Dependence"
Astronomy & Astrophysics, in press

[19] Tsutomu T. Takeuchi, Takako T. Ishii, Hiroyuki Hirashita, Kohji Yoshikawa, Hideo Matsuhara, Kimiaki Kawara, Haruyuki Okuda (2001)
"Exploring Galaxy Evolution from Infrared Number Counts and Cosmic Infrared Background"
Publications of the Astronomical Society of Japan, in press